Version 7.0
June 1996

Faint Object Camera Instrument Handbook

SPACE
TELESCOPE
SCIENCE
INSTITUTE

For all questions, please contact the "Hotseat" at *help@stsci.edu*.

FOC Instrument Team

Name	Title	Phone	e-mail
Antonella Nota	FOC Group Lead	410-338-4943	*nota@stsci.edu*
Robert Jedrzejewski	FOC Instrument Scientist	410-338-4817	*rij@stsci.edu*
Mark Voit	FOC Instrument Scientist	410-338-4714	*voit@stsci.edu*
Warren Hack	Data Analyst	410-338-4943	*hack@stsci.edu*

FOC Instrument Handbook Revision History

Version	Date Of Issue	Editors
1.0	May 1985	F. Paresce
2.0	April 1990	F. Paresce
3.0	April 1992	F. Paresce
4.0	February 1993	A. Nota, R. Jedrzejewski, W. Hack
5.0	May 1994	A. Nota, R. Jedrzejewski, P. Greenfield, W. Hack
6.0	June 1995	A. Nota, R. Jedrzejewski, W. Hack
7.0	May 1996	A. Nota, R. Jedrzejewski, M. Voit, W. Hack

List of Figures

List of Tables

1.0 HANDBOOK REFERENCE GUIDE

The basic aim of this handbook is to make relevant information about the performance of the FOC+COSTAR system available to a wide group of astronomers. This handbook must be used when applying for HST time, and later on to calculate and plan FOC exposures.The information here provided has been obtained from in-flight characterization of the FOC, combined with COS-TAR ground and flight calibrations and represents our best present knowledge of the performance of the FOC+COSTAR system. This handbook covers not only the description of the camera (hardware and performance), but also describes how to calculate exposure times in the preparation of a proposal, what features of the FOC have been calibrated, and also how to retrieve the latest FOC calibration files. The following sections, organized through questions and answers, will help the reader to locate where the individual items are discussed throughout the handbook. In addition, at the end (Section 1.10), we provide a summary checklist that will prove useful to those observers who are considering writing a FOC proposal, to ensure they have considered all the features and limitations which must be taken into account when planning a FOC observation.

1.1 What is the FOC?

The Faint Object Camera (FOC) is one of the imaging cameras on board the Hubble Space Telescope (HST). It is a long-focal-ratio, photon-counting imager capable of taking high-resolution two-dimensional images of the sky up to 14×14 arcseconds^2 in size with pixel dimensions as small as 0.014×0.014 arcseconds^2 in the 1150 to 6500Å wavelength range. Its performance approaches that of an ideal imaging system at low light levels. The FOC is the only instrument on board the Hubble Space Telescope (HST) to fully use the spatial resolution capabilities of the Optical Telescope Assembly (OTA) and is one of the European Space Agency's contributions to the HST program. *Chapter 3* provides a complete overview of the camera itself, with COSTAR and its functions described in *Chapter 2*. More technical details about the specifics of the detectors, such as the apertures, filters, and electronics are given in *Chapter 4*.

1.2 Why Use the FOC?

Primarily the FOC serves as an imaging camera, but the possibility of using objective prisms and the F/48 long slit facility also provide some spectrographic capabilities.The following are just some of the presently unique properties of the FOC:

> **a. Spatial Resolution**: The FOC offers imaging capabilities with a pixel size of 0.014" and a FWHM of less than 2 pixels (less than 0.6 Planetary Camera pixel). The dependence of the FWHM on wavelength is described more fully in *Section 6.1*. Compared to STIS, the FOC has better sampling (being the pixel size 0.05" for the STIS CCD and 0.025" for the STIS MAMA, against 0.014" for the FOC).

> **a. UV Sensitivity**: The FOC provides peak sensitivity at 3400Å and better sensitivity than the WFPC2 for all observations with $\lambda < 4000$Å, down to 1150Å. *Section 6.3* discusses the overall throughput of the FOC, while the large selection of UV filters are described in *Section 4.4*. The FOC UV response in the range 2000-3000 is comparable to the STIS

NUV-MAMA.

b. Polarizers: The FOC provides three polarizer filters with pass directions of 0°, 60° and 120°. These filters provide a straight-through, low reflection-angle system. The specifics of these filters and their calibrations can be found in *Section 4.4.3*.

c. Objective Prisms: There are two objective prism filters for use with the FOC, operating in the near-UV and far-UV regions. Objective prism images allow spectra to be obtained for different regions of a spatially resolved object at the same time with high throughput, and low- to medium- resolution from 1700Å - 6000Å for the near-UV prism and 1150Å-6000Å for the far-UV prism. *Section 4.4.2* discusses the resolution and throughput of the prisms in more detail, while *Section 6.14* discusses the accuracy of the spectrophotometry.

d. Deep Photometry of Point Sources: The low detector background and its insensitivity to cosmic rays allows for long exposures providing very deep photometry of point sources in the field of view, reaching a S/N of 10 for a V=26 B5V star in a 45 minute exposure through the U filter (F342W). The limiting magnitudes are discussed in more detail in *Section 8.6*.

e. F/48 Long Slit Spectroscopy: The F/48 relay contains a long-slit spectroscopy facility for obtaining spectra with a resolving power of ~1150 in 4 orders spanning from 3600-5400Å, 1800-2700Å, 1200-1800Å, and 1150-1350Å. Problems with the F/48 relay have hampered its use in the previous cycles, but long slit spectroscopy will be again offered as the sole use of the F/48 relay in Cycle 7. *Section 4.5* discusses this facility in more detail, while *Section 6.13* describes the current performance of the F/48 detector itself. In *Chapter 11* we describe the existing calibration program for the F/48 long slit facility. After the refurbishment mission, STIS will replicate, more efficiently, the FOC long slit spectroscopic capabilities.

1.3 What other imaging capabilities does HST offer?

In addition to the FOC, HST offers the WFPC2 camera for wide field imaging, and NICMOS for near-IR imaging where the FOC has no sensitivity. These cameras complement each other by covering the complete spectral range from the far-UV to the near-IR. In addition to its extensive spectroscopic capabilities, STIS also offers imaging in the UV and in the optical, mainly limited by the available filter complement (see STIS Handbook, *Chapter 5*, for additional details).

In comparison to the FOC, WFPC2 and STIS can offer the following advantages:

a. Area Coverage: The WF CCDs have an imaging plate scale of ~0.1" per pixel over each of the three 800×800 chips, while the PC offers a plate scale of ~0.045" per pixel. This results in a combined field of view of nearly 160×160", compared with the 14"×14" (maximum) for the FOC. Due to the large size of some objects, it may be necessary to forego the increased resolution of the FOC in order to image the entire object with the WFPC2. Compared to STIS, the FOC has a smaller field of view (14" x 14" compared to 28" x 51" for the STIS CCD and 25"x 25" for the STIS MAMA) but better sampling (being the pixel size 0.05" for the STIS CCD and 0.025" for the STIS MAMA, against

0.014" for the FOC).

a. Far-UV Sensitivity: Compared to the STIS FUV-MAMA, the FOC is less sensitive in the 1150 Å- 2000 Å range.

b. Red Sensitivity: Both the STIS and the WFPC2 CCDs have a peak sensitivity in the red portion of the spectrum with filters all the way out to 1μ. In contrast, the FOC cuts off at about 6000Å resulting in the WFPC2 and STIS having better sensitivity than the FOC for $\lambda > 4000$Å.

c. High Precision Photometry: Photometry with the FOC suffers from other effects which limit the errors to about 5-10%. However, the WFPC2 CCDs provide a better understood background that can result in photometry with lower errors.

1.4 What is the actual performance of the FOC?

Table 1 summarizes the basic performance characteristics of the FOC, while *Chapter 6* breaks down each aspect in more detail. Specific information regarding the PSF, the sensitivity, the background and flat-fields, plus many other characteristics, is given in the individual sections in that chapter. This information can then be used to estimate the exposures necessary to carry out an observing program.

1.5 How do I calculate the FOC exposure times?

Chapter 7 is devoted entirely to calculating the exposure time by hand for any given FOC exposure using information given in the Handbook. In contrast, *Section 8.1* describes how FOC-SIM has been designed to use that same information automatically to calculate exposure times and to simulate FOC images. For point source exposure time calculations, FOCSIM can actually be run by anyone under the FOC WWW pages *(Section 8.2)* using a very simple graphical form. Objective prism observations can now be simulated using the STSDAS package FOCPRISM as described in *Section 8.5*. This combination of options should allow every user to easily model their FOC exposure.

1.6 What features of the FOC have been calibrated?

Chapters 6 and 11 are both devoted to describing what aspects of the FOC have been calibrated and to what accuracy. In general, the most effort has been spent on determining the absolute sensitivity of the FOC, the aperture location (for target acquisitions), the geometric distortions, the objective prism dispersion curves, and, to a lesser degree, the flat-field behavior of the F/96 relay. At the moment of writing, very little is known on the post-COSTAR performances of the F/48. *Chapter 11* details current knowledge and status of the F/48 calibration.

1.7 Where can I get updated information on the FOC?

This handbook can only report on calibrations which were analyzed prior to its publication,

whereas new calibration data continues to be taken throughout each cycle. As a result, there may be updated information, or maybe new calibration files, coming out after the publication of this handbook. This up to date information will be made available via the FOC team's WWW pages (see *Chapter 9* for more details) at:

> **http://www.stsci.edu/ftp/instruments.html**

These WWW pages provide access to electronic copies of calibration reports, calibration files, answers on data reductions, and even this handbook. In addition to the WWW pages, the same information can also be accessed via ftp at:

> **ftp.stsci.edu/instrument_news/FOC**

Through these two channels and the usual documentation, the FOC team will insure that the latest calibration data will always be readily available.

1.8 Where is information about pre-COSTAR FOC data?

This handbook applies only to post-COSTAR observations. Therefore, for observers analyzing pre-COSTAR FOC data, Version 3.0 of the handbook should be referenced. If there are any difficulties in obtaining a copy of Version 3.0 of the FOC Instrument Handbook, please contact the hotseat (*help@stsci.edu*).

1.9 What's New with the FOC Handbook?

A great deal of effort has been put into making this version of the handbook a more complete reference for FOC. This chapter itself represents a new addition, not only providing some guidance in using the handbook, but also summarizing the latest information about the FOC. Throughout the handbook, references have been included to documentation produced by the FOC team, most of which is available on-line. New information is provided on:

> **a. F/48 performance and availability:** Problems with the F/48 kept it from being used in the previous cycles, however, recent tests have shown that the situation is improving so that the detector can be reliably used for science. As a result, **the F/48 relay will be available AGAIN ONLY for long-slit spectroscopy** in Cycle 7. The latest information describing the recent performance of the F/48 can be found in the new *Section 6.13*.

> **b. Calibration accuracies:** The results of the calibration activities have always been implicitly incorporated into each previous version of the handbook, however, a separate chapter (*Chapter 11*) describes in more detail the present calibration program (*Section 11.1*), along with the accuracies of the current calibrations (*Section 11.2*). *Chapter 11* also contains details on the current F/48 long slit calibration plan and expected accuracies.

> **c. Updated calibrations of the objective prisms:** The dispersion curves for the F/96 objective prisms have been re-calibrated and the results are given in Table 5. In addition, analysis techniques and spectrophotometry accuracies are now provided in a new section (Section 6.13).

> **d. Updated information on the performances of the Neutral Density filters:** The in-flight transmission properties of the five neutral density filters available in the F/96 camera

have been calibrated for the first time in Cycle 5, at optical and UV wavelengths. Details are contained in Section 4.4.3.

e. New calibration of filter shifts: Most F/96 filters produce image shifts which can be as large as several pixels. These shifts have now been calibrated and the details are provided in Section 4.4.3.

f. Updated information on FOC simulators: The FOC Handbook has always contained a chapter describing the software package FOCSIM, which was primarily accessible only through an account at the Institute. This chapter has been enhanced to describe the new software that has been added to determine the orientation of a FOC image on the sky. This software can be used either when planning an observation requiring a special orientation, or to determine the orientation of an image already obtained.

There are many other less significant changes throughout the handbook as well, but primarily they only served to update what was already present in earlier versions, rather than adding anything new. These updates, along with the new material listed above, combine to make this handbook the most up-to-date and complete version possible.

1.10 What considerations should be made in preparing an FOC observing proposal?

The proposal instructions provide the details of the syntax for preparing an HST observing proposal, but it is this handbook which provides the details necessary for putting together a feasible program. Unfortunately, it is a difficult task to keep all the details of the FOC in mind when preparing a proposal. The following summary describes the most common problems in using the FOC and indicates where these problems are discussed in the handbook.

a. Bright Targets: Great care must be taken to not expose the FOC to an excessive amount of light. The specific bright limits are described in *Section 6.6*. Bright targets, defined as any target of magnitude 9 or brighter, must be observed using the Special Requirement CHECK-FILTER=YES (described in *Section 6.6*). This procedure checks to make sure that proper filters are in place to assure a safe count rate from the star. The filter combination, however, must be verified by an FOC Instrument Scientist prior to execution of the proposal, necessitating a careful simulation of the expected observation.

b. Photometric Linearity and Image formats: The FOC offers a wide range of formats for imaging, each with its own photometric characteristics. As a rule, the smaller the format, the higher the count rate can be, while maintaining photometric linearity in the image (see *Section 6.2*). The smaller formats are best suited for imaging brighter objects that are not very large, while the largest formats provide the best field of view for imaging faint sources. In general, though, point sources should not exceed 1 count $\sec^{-1}$ pixel^{-1} for the central pixel (*Section 6.2.2*) and extended sources should not exceed 0.15 counts $\sec^{-1}$ pixel^{-1} in the 512x512 format (*Section 6.2.1 and Table 10*) in order to obtain a photometrically linear image. We recommend that all observations be maintained in the linear regime. In special cases, scientifically justified, the Instrument Scientists can waive this requirement.

c. Small Image Format and INT ACQs: Sometimes it is necessary to use the small formats, such as the 256×256 format. In these cases, it becomes critical to have pinpoint target acquisition since the field of view is only 3.7"×3.7". An error of even 1" in the target coordinates could result in the target missing the field of view, since guide star errors are typically 0.6" and the FOC aperture positions are only known to about 0.2" (see *Section 11.2*). Therefore, whenever a format with a dimension less than 512 pixels is used, an INT ACQ must be taken to insure that the target is acquired within the small format.

d. Inaccurate Target Coordinates: The default acquisition mode is a blind pointing, described in *Section 5.2.2*. The small field of view for the FOC places strict constraints on the accuracies for the target coordinates. Even errors as large as 1" can seriously jeopardize the observation given the small field of view for the FOC. Therefore, all FOC target coordinates should be measured using GASP in order to provide the most consistent set of coordinates for this blind pointing.

e. Wrap-around in 8-bit formats: The largest format for the F/96 relay provides a field of view of 14.7"×14.7". Unfortunately, due to memory constraints (*Section 4.8*), the largest formats (512z×1024 and 512×1024) only have 8-bit deep pixels, i.e. they can only count up to 255 counts per pixel (*Table 7*). For a point source with a count rate of 0.25 counts sec^{-1} pixel^{-1}, the peak pixel of the star will count up to 255 in 1000 seconds then reset to 0 on the next count. The image has lost track of those counts, resulting in a loss of photometry. When using these formats, short exposures should be taken, then co-added, as long as the sources in the image maintain count rates that are linear (see *Table 10* for extended sources, *Section 6.2.2* for point-sources).

f. Format sensitivity: Each FOC format has a different photometric sensitivity (*Section 6.3.1*). This usually causes no problem, except in cases where images taken in different formats are compared. If different fields are to be compared, then taking the images in the same format will insure a consistent photometric response due to the image format, eliminating one more source of error in the photometry.

g. PSF Artifacts: A great advantage of the FOC is that it can discern detail on much smaller scales than any other instrument on HST. However, for the smallest details, differences in the shape of the PSF must be known in order to distinguish source structure from instrumental structure. A description of some of the most obvious features of FOC PSFs is given in *Section 6.1*, including a jet-like feature in the F372M PSF and some degradation in the F320W PSF. A couple of other filters (F501N and F502M) both show faint ghost images, as well. These might be important for programs trying to detect faint sources near brighter ones. A full library of observed PSFs can be retrieved using the FOC WWW pages (*Chapter 9*) to provide a better understanding of them prior to selecting the filter to be used for the observation.

h. Background noise, stray light and flat-field features: Although the FOC benefits from having very low background noise (*Section 6.4*), there are still limitations as to what can be detected in that faint background. Detection of very faint, background-limited sources relies on knowing the flat-field response of the FOC (*Section 6.9 and Section*

11.2.3) and the effect of the geometric correction on the background (*Section 6.11*). In addition, requirements can be specified in the proposal to minimize the effect of stray light (*Section 6.5*) in images of extremely faint sources.

i. Overhead times for images: The use of RPS2 in preparing observing proposals now allows observers to more efficiently schedule their observations in each orbit. This system automatically incorporates all the overhead times for taking FOC images (*Section 6.7*). One overhead which can be minimized is the selection of the filter for the image. By selecting the filters one after the other as they are situated on the filter wheels (see *Tables 3 and 4* for filter wheel positions), the time spent changing filters can be minimized, allowing for more net exposure time.

j. Visible Leaks for filters: Selecting the proper filter for the exposure usually focuses on obtaining a good count rate. However, each filter has its own transmission characteristics (*Section 4.4.1*) with their own visible leak concerns. For some observations, a small percentage of light from the visible (for a UV filter) does not make a difference. For other science, the amount of light from outside the desired passband can seriously affect the results. This problem is addressed in *Section 6.10*, with FOCSIM also providing a means of judging how serious this problem would be for a given observation (*Section 8.1*).

k. Geometric Stability: Long series of FOC images have been noticed to suffer from small, residual variations in the geometric stability, as described in *Sections 6.11 and 6.12*. This can present some problems from programs needing astrometric conditions for their science. The accuracies in the distortion which can be expected are discussed in *Section 11.2.2*, along with recommendations on how to best account for this in the proposal.

We advise all the users who finally decide to write a proposal using the FOC to examine all the items presented in this checklist. This will help them to optimize the scientific return from the instrument, and to obtain excellent images.

2.0 COSTAR OVERVIEW

The HST was placed in orbit on April 24, 1990. A few months later, it was realized that the 2.4m diameter primary mirror suffered serious optical degradation due to a manufacturing error at Perkin-Elmer. The primary mirror of the HST OTA was incorrectly figured with the wrong conic constant, which produced severe spherical aberration at the OTA image plane (Burrows et al. 1991, *Ap.J.Letters*, 369,L21.). This aberration, which caused the light from a star to be spread out into a circular Point Spread Function (PSF) of 2.5 arcseconds radius, could not be removed by changing the secondary mirror focus position or by moving the primary mirror actuators. In the fall of 1990, a Strategy Panel was convened to investigate possible methods for removing the spherical aberration, and made the following recommendations: 1) replace the Wide Field Planetary Camera (WF/PC) with the WFPC2 at the earliest possible opportunity, with the optics of the WFPC2 re-designed to counteract the OTA spherical aberration, and 2) replace the High-Speed Photometer with an instrument designed to deploy corrective optics in front of the remaining axial instruments (FOC, GHRS and FOS)—COSTAR. Both these recommendations were approved by NASA, and were implemented in the first Servicing Mission executed in December 1993.
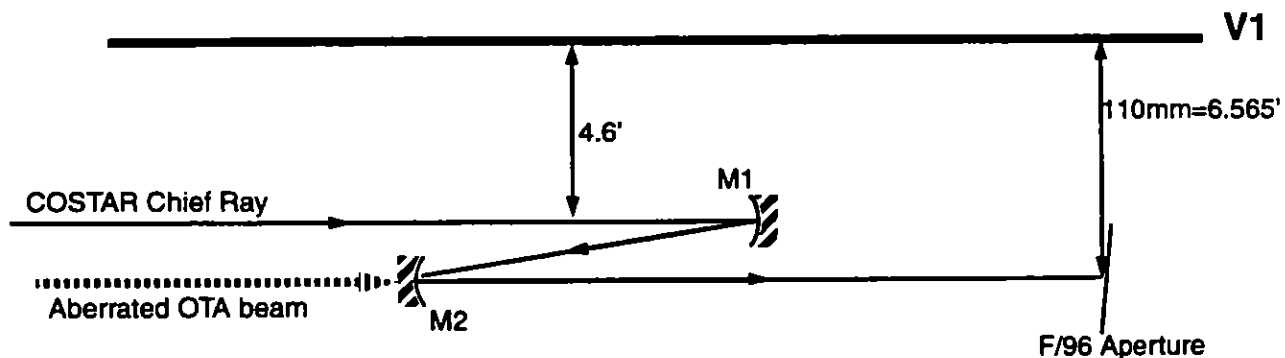
Figure 1. Diagram showing the COSTAR correction principle for the F/96 relay. The aberrated OTA beam (dashed line) is blocked from reaching the FOC aperture by the M2 mirror.

COSTAR (Corrective Optics Space Telescope Axial Replacement) has restored the two prime scientific objectives of the FOC: deep imagery and photometry of very faint celestial objects and imagery of bright objects at the highest possible resolution available from HST. The FOC is now capable of detecting a star of U magnitude 27.5 in a 5 hour exposure with a S/N of 5 and of resolving bright sources in the near UV up to an effective angular resolution of 0.03 arcseconds.

COSTAR replaced the High Speed Photometer in the Axial bay of HST, in the V2, +V3 quadrant (see Figure 7). It is a "passive" instrument, in that it has no detector of its own, its sole purpose being to deploy a set of mirrors in front of the other Axial Scientific Instruments (ASI). These mirrors, and their associated mounts and arms, serve only to block the aberrated OTA beam from entering the ASI entrance apertures and to correct the spherical aberration of a different part of the OTA field of view before re-directing the corrected beam into the ASIs. A schematic diagram of the COSTAR optics in front of the F/96 relay is shown in Figure 1. There is a separate set of mirrors that corrects the F/48 channel, mounted on the same arms as those for the F/96 channel.

Before COSTAR, the aberrated F/24 OTA beam at 6.565 arcminutes from the V1 axis formed an image at the FOC focal plane aperture 110 mm from the V1 axis. After the deployment of COSTAR, the M2 mirror and its mounting arm blocks this light from entering the aperture. The

beam that would have formed an image 4.658 arcminutes from the V1 axis is re-directed by the spherical M1 mirror to form an image of the OTA exit pupil on the M2 mirror. This mirror becomes the exit pupil of the OTA+COSTAR optical system, and the anamorphic aspheroidal figure fulfills three functions:

- it re-directs the corrected beam into the FOC, forming an image at the FOC focal plane aperture;

- it corrects for the OTA spherical aberration;

- it increases the astigmatism from that present at 4.658 arcminutes to that appropriate to 6.565 arcminutes because the FOC is designed to correct for exactly the new amount of astigmatism.

However, there is one major difference between the COSTAR-corrected beam and the unaberrated OTA: the F/ratio is increased from F/24 to F/37. **This results in a change in the F/number of the FOC relays from F/48 to F/75.5 and from F/96 to F/151. Because the names "F/48" and "F/96" are deeply-rooted in the HST ground system at all levels, from proposal entry to data archiving, we have been forced to retain these names despite the fact that they do not describe the true focal ratios of the cameras anymore. As a result, the user must take particular care in reading this handbook, for whenever we mention the F/48 and the F/96 relays, we are really referring to the relays with focal ratios of F/75.5 and F/151 respectively.**

A schematic diagram of COSTAR when deployed is shown in Figure 2. The FOC M1 mirrors are mounted on an arm which can be tilted in each of 2 orthogonal directions. This adjustment is necessary to accurately center the image of the OTA exit pupil on the M2 mirror, and was done on orbit. Any error in this centering results in the introduction of coma into the PSF. Since the M1 mirrors for both of the relays are on the same mount ("ganged"), only one channel (the F/96) can be optimized in this way. It is anticipated that the tilt of the F/48 M1 mirror relative to that of the F/96 mirror was set during ground alignment to sufficient accuracy that no appreciable residual coma is left in the F/48 PSF. Optimization of the M1 tilt was accomplished during the Servicing Mission Observatory Verification (SMOV) period shortly after the installation of COSTAR.

The M2 mirrors for both of the new channels are also on a single arm mounting, but there is no tip/tilt capability. Both arms are connected to the Deployable Optical Bench (DOB), which can be commanded to move over a 16mm range parallel to the V1 direction. This was used to focus the F/96 channel during SMOV. The focus position of the F/48 channel relative to that of the F/96 channel was set to an accuracy of 0.1mm or less during ground alignment.

The correction of the spherical aberration of the OTA by COSTAR does introduce a small number of side-effects that were not present in the original design of HST+FOC. Firstly, the focal plane tilt of the OTA at the FOC entrance apertures cannot be duplicated by the 2-mirror COSTAR system. The tangential and sagittal image planes produced by COSTAR are tilted with respect to those in the OTA, and tilted appreciably with respect to each other. This means that perfect astigmatism correction can only be achieved at one field point. Similarly, the mean focal surface produced by COSTAR is tilted with respect to the mean focal surface produced by the OTA, so that there is a field-dependent focus variation. These effects are described more fully in Section 6.1.

Secondly, the HST+COSTAR exit pupil is now only 530mm from the FOC entrance apertures (compared to 7m for the uncorrected OTA). This causes unavoidable vignetting in the F/48 camera for field positions more than about 12 arcseconds away from the optimally-corrected field point. The effects of this vignetting are discussed in Sections 4.2 and 6.9. The F/96 channel does not suffer from vignetting. For this reason, it was decided to make the F/96 channel the 'preferred' channel of the FOC and to attempt to optimize the image quality of this channel.
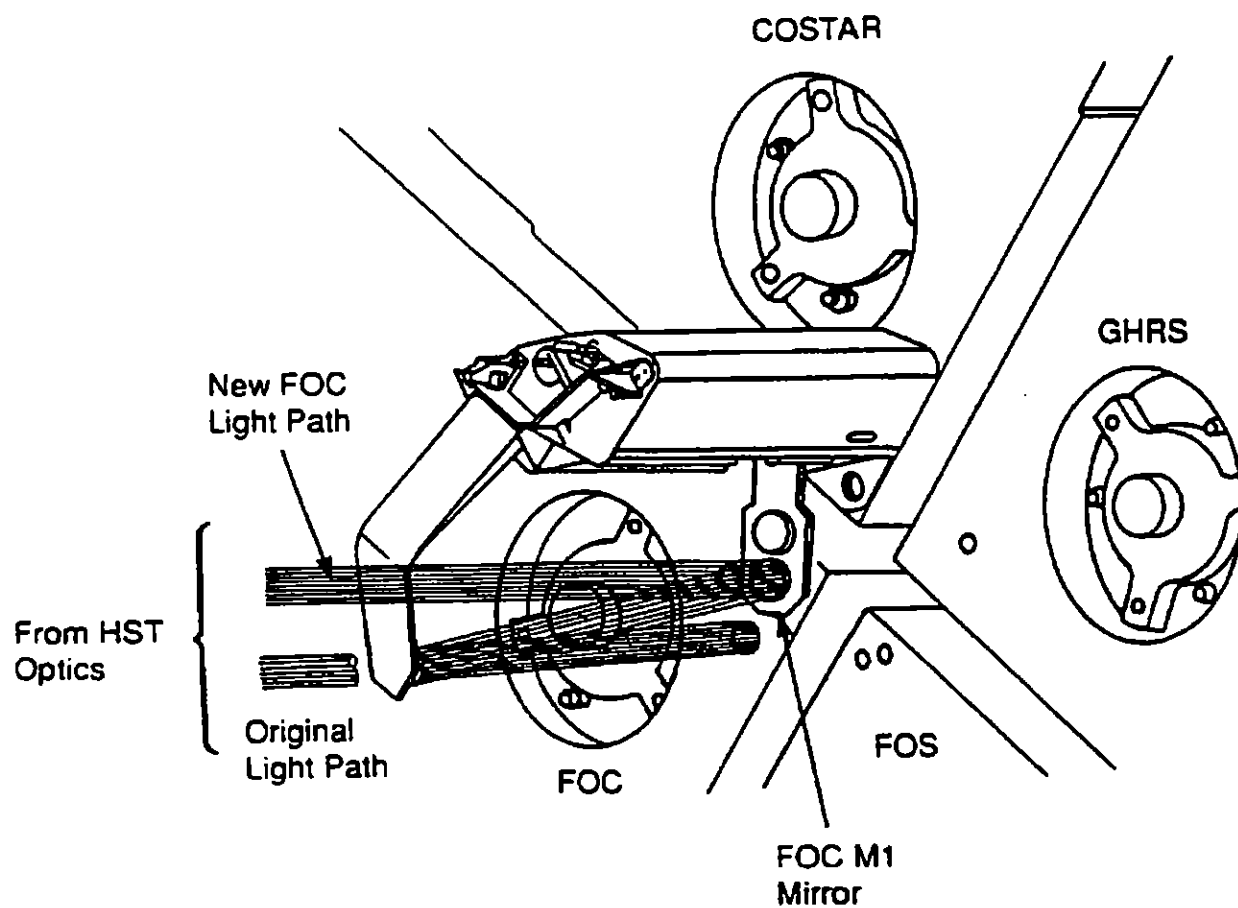
Figure 2. A Schematic View of COSTAR, after deployment, showing the FOC light paths. For clarity, the FOS and GHRS M2 arms are omitted.

3.0 INSTRUMENT OVERVIEW

The Faint Object Camera (FOC) is one of the four axial scientific instruments sharing the HST focal plane. It is located in the -V2, -V3 quadrant (see Figure 7), has overall dimensions of 0.9 × 0.9 × 2.2 meters, weighs 320 kg and consumes 130W of power on average in operation. An overall operational and data flow block diagram of the instrument is shown in Figure 3 with the FOC itself contained within the dashed line. Radiation from an astronomical source focused onto the OTA focal plane is reimaged by COSTAR and fed into either of two separate and independent cameras each with its own entrance aperture, imaging optics and detector system.

One camera magnifies the image on the OTA focal plane by a factor of two to an effective focal ratio of F/75.5 while the other magnifies the focal plane by a factor of four to an effective focal ratio of F/151. This transfer is accomplished mainly in order to match the OTA resolution performance with the available detector pixel size.

Each optical relay consists of segments of a full optical figure of revolution the axis of which is perpendicular to the OTA focal plane at the FOC entrance aperture location. Both cameras have the same overall length and operate at the same distance from the OTA optical axis. The re-imaging optics transfers the COSTAR corrected OTA image onto the photocathode of a photon counting detector with negligible spherical aberration or coma and corrects for the residual OTA off-axis astigmatism. The FOC optical system also provides means for dispersing, filtering, attenuating, polarizing and focusing the image formed by the OTA and for in-flight calibration of the relative and absolute response in the visible.

All the optical elements and both detectors are supported on an optical bench which is rigidly connected to the focal-plane structure of the OTA and is contained within the load-carrying structure which also provides a light-tight enclosure. To meet the image stability requirements, the internal surfaces of the load-carrying structure which enclose the optical bench are actively thermally controlled during all operational modes with a stability of better than $0.5°$ C. An exploded schematic view of the FOC is presented in Figure 4.

The two detectors are two dimensional photon counting devices of identical design. Each consists of a three-stage image intensifier which is optically coupled by a relay lens system to an Electron Bombarded Silicon Target (EBS) TV tube. The tube detects scintillations at the output of the intensifier corresponding to the arrival of individual photons at the first stage photocathode. The central x-y position of each burst of visible light is measured by a dedicated video processing unit (VPU), and the contents of a memory location in the scientific data store (SDS) unit associated with that position are incremented by one. At the end of the exposure, the accumulated image in the SDS is sent directly out of the FOC to a dedicated unit in the ST Scientific Instrument Control and Data Handling (SI C&DH) subsystem which consists of a computer with a reprogrammable non-volatile memory. The two detectors in orbit produce a dark noise typically of $\cong 7 \times 10^{-4}$ counts sec^{-1} pixel^{-1} for the F/96 relay and $\cong 10^{-2}$ counts sec^{-1} pixel^{-1} for the F/48 relay (see also Section 6.13 for the current performance).

The SDS storage capacity is adapted to an image area of 512 × 512 resolution elements and provides a 16 bit data word for each pixel. This results in a memory capacity of 256K words of 16 bits each or 0.5 Mbyte in total. The word length can also be commanded to 8 bits to store data in a 512 × 1024 pixel format with reduced dynamic range. Because of operational constraints, a time interval of at least 3.9 minutes must elapse between the end of an exposure and the start of the next (see Section 6.7 for more details).

The detectors are sensitive to radiation between 1150 and 6500Å, the lower limit being set by
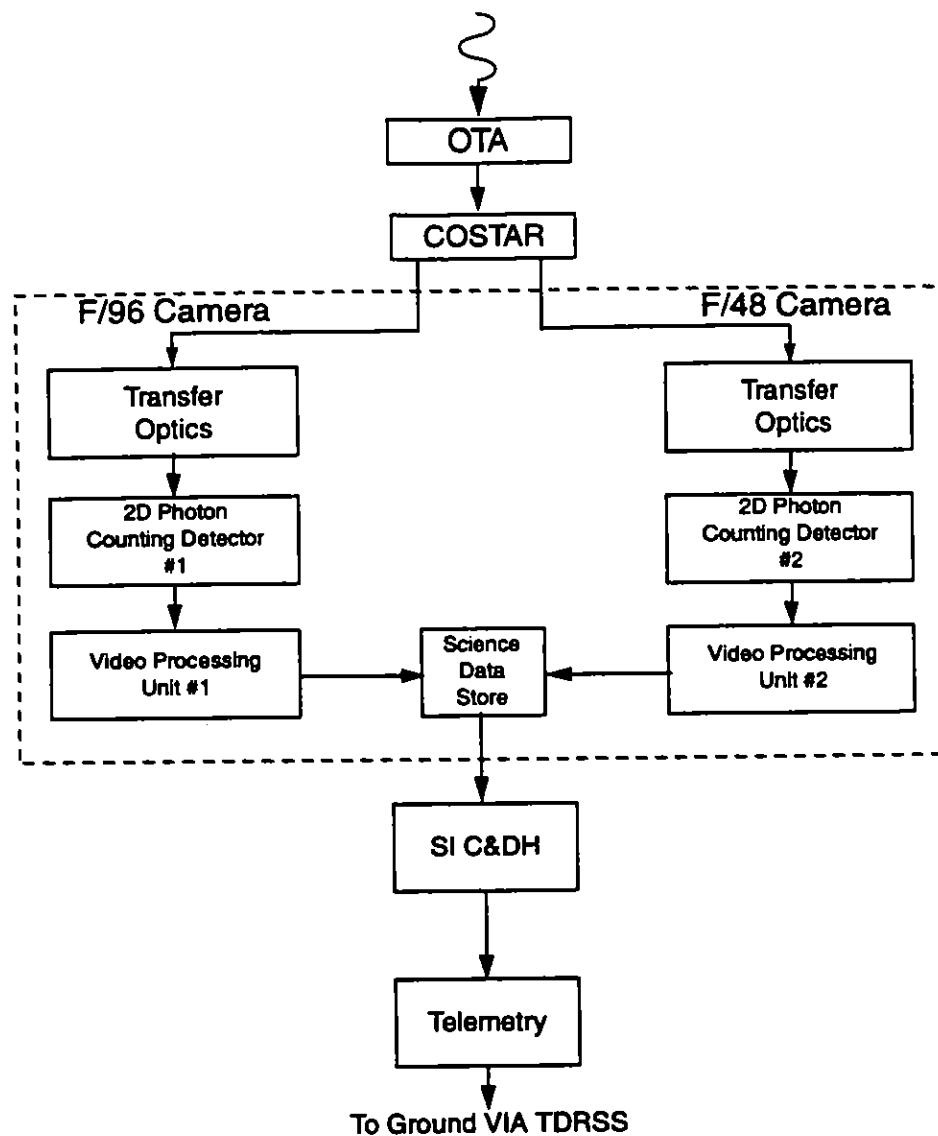
Figure 3. FOC Operational and Data Flow Block Diagram

the MgF_2 input window and the upper limit by the bialkali photocathode material. The useful photocathode area is 40 millimeters in diameter while the size of an independent resolution element (pixel) is on average normally $\cong$ 24 × 24 microns squared, but one dimension can be stretched (zoomed) to $\cong$ 48 microns. The longer pixel dimension is in the TV frame scan direction and perpendicular to the dispersion direction of all but one (the FOPCD) of the dispersing elements. The plate scales for the F/48 and the F/96 relays are 1.131 and 0.569 arcseconds mm^{-1} respectively.

These parameters, coupled to the quoted maximum SDS capacity, imply that the F/48 camera has a maximum achievable field of view of $\cong$ 28 × 28 arcseconds squared imaged at a pixel size of 0.056 × 0.028 arcseconds squared (512 zoomed × 1024, 48 × 24 micron squared pixels with 8-bit words). The corresponding values for the F/96 relay are $\cong$ 14 × 14 and 0.028 × 0.014 arcseconds squared. Smaller fields can be imaged at higher spatial resolution and extended dynamic range (see Table 7 for a partial list, and Section 5.1 for more details).
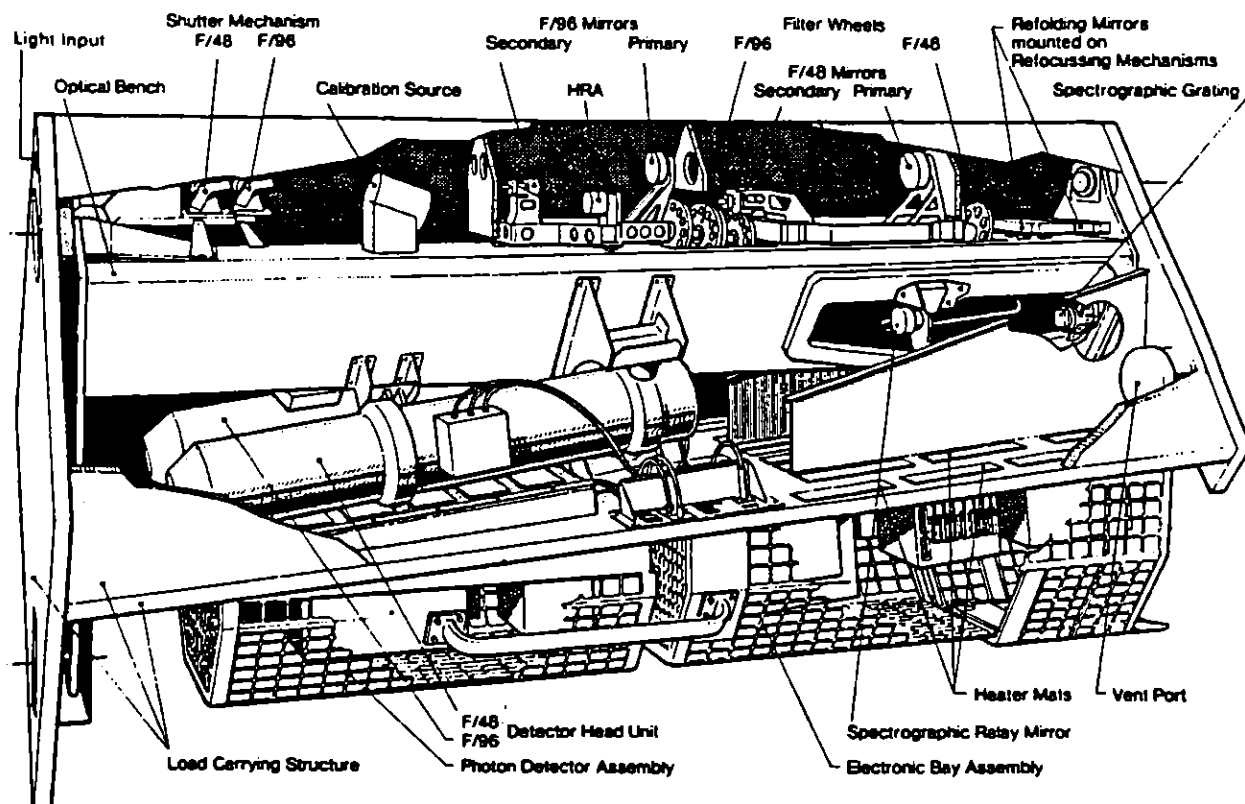
Figure 4. Schematic Drawing of the FOC

In summary, the key operating features of the FOC are its low noise, high angular resolution, high sensitivity in the UV range and extreme versatility due to its occultation, polarization, and objective prism capabilities. Its most significant limitations, on the other hand, are its relatively small field of view, further restricted by COSTAR, and the non-linearity of response at high count rates which limits its useful application to objects yielding less than $\cong 2$ counts sec^{-1} pixel^{-1}, corresponding to a U $\cong$ 18.5 A0V star observed through the F342W filter with the F/96 relay, for example. A summary of the most important performance characteristics of the FOC as presently known is given in Tables 1 and 2 for the imaging and spectrographic modes, respectively.

Table 1: Summary of FOC Performance Characteristics I. Imaging

Optical Modes	F/48[a]	F/96
Focal Ratio	75.5	151
Operating Range (Å):	1150-6500	1150-6500
Number of Bandpass Filters:	11	39
Bandpass FWHM (Å) Max:	2700	2300
Bandpass FWHM (Å) Min:	300	34
Maximum ND attenuation (mag.):	0	9
Field of View (arcsec) Max:	28x28	14x14
Field of View (arcsec) Min (128x128):	3.6x3.6	1.8x1.8
Unzoomed Pixel Size (arcsec):	0.028	0.014
Minimum Wavelength for Critical Sampling (Å):	6500	3250
Peak Efficiency (%):	6.6	7.9
Peak Wavelength (Å):	3400	3700
Limiting Magnitude, Point Source[b]:	27	27.5
Limiting Magnitude Arcsec^{-2}, Extended Source[c]:	23.5	23
Dynamic Range, Point Source[d] (mag):	20-27	19-27.5
Dynamic Range, Extended Source[e] (mag arcsec^{-2}):	18-25	17-25
Overload Magnitude:	9	9
Number of Polarizing Prisms[f]:	0	3

a. The F/48 mode is offered in Cycle 7, limited to long slit spectroscopy ONLY.
b. S/N = 5, 5 hour integration, U band.
c. Same as b. over 0.1" × 0.1" area.
d. 2 counts sec^{-1} pixel^{-1} upper limit
e. 0.5 counts sec^{-1} pixel^{-1} upper limit
f. 0°,60°, 120° direction of polarization

Table 2: Summary of FOC Performance Characteristics II. Spectroscopy

Spectral Modes[a]:	F/96-FUVOP	F/96-NUVOP	F/48-SP	F/48 SP-CD
Operating Range[b]:	1150-3000	1700-4000	3600-5400 (1) 1800-2700 (2) 1200-1800 (3) 1150-1350 (4)	3600-5400 (1) 1800-2700 (2) 1200-1800 (3) 1150-1350 (4)
Maximum Field of View (arcsec):	14×14	14×14	0.06×12.5	0.06×12.5
Number of Bandpass or Order Sorting Filters Available:	33	33	11	5
Number of ND Filters Available:	1	1	0	0
Spatial Resolution (arcsec):	0.04	0.04	0.063×0.1	0.063×0.1
Resolving Power:	100	250	1150	1150
Wavelength (Å):	1500	2500	(1) - (4)	(1) - (4)
Spectrum Length (pix):	200	750	1024	1024
Spectrum width (pix):	3	3	≤450	≤450
Maximum Spectral Resolution (Å):	3	1.5	4 2 1.3 1.0	4 2 1.3 1.0
Peak Efficiency (%):	6.4	6.4	1.1 (1) 0.55 (2) 0.15 (3) 0.13 (4)	1.1 (1) 0.53 (2) 0.13 (3) 0.08 (4)
Limiting Flux, Point Source[c] (ergs cm^{-2} s^{-1}):	6×10^{-16}	1×10^{-16}	3×10^{-16}(1) 7×10^{-16}(2) 6×10^{-15}(3) 2×10^{-14}(4)	3×10^{-16} (1) 7×10^{-16} (2) 7×10^{-15} (3) 3×10^{-14} (4)
Limiting Flux, Extended Source[d] (ergs cm^{-2} s^{-1} arcsec^{-2}):	2×10^{-14}	4×10^{-15}	3×10^{-14} (1) 7×10^{-14} (2) 6×10^{-13} (3) 2×10^{-12} (4)	3×10^{-14} (1) 7×10^{-14} (2) 7×10^{-13} (3) 3×10^{-12} (4)

a. SP = Spectrograph; SP-CD = Cross Dispersion Spectrograph; F/48 is Available in Cycle 7,ONLY for long slit spectroscopy (SP).

b. Spectrograph characteristics are given at the following wavelengths for each order: (1) 5000Å, (2) 2500Å, (3) 1500Å, (4) 1250Å

c. S/N = 5, 3 hour integration, flux in emission line at 1500Å(FUVOP) and 2500Å(NUVOP).

d. Same as c. over 0."063 × 0."063 area.

4.0 DETAILED INSTRUMENT DESCRIPTION

4.1 TRANSFER OPTICS

A component block diagram of the FOC transfer optics is shown in Figure 5. A conceptual schematic optical layout in a plane containing the V1 axis and the chief ray is shown in Figure 6. Radiation from the COSTAR corrected OTA enters the FOC through a baffled tube that leads to a field-defining entrance aperture located in a plane tangential to the OTA focal surface and centered on or near the best focus point at the position of each relay. Just beyond the entrance aperture, the radiation encounters a light tight shutter mechanism that, in its closed position, introduces a calibration mirror into the beam to intercept light emitted by an internal source of visible radiation and to uniformly illuminate the FOC object plane.

Once past the shutter, radiation impinges on a two element aplanatic optical system consisting of a spherical concave primary and an elliptical convex secondary mirror. This optical system magnifies the OTA focal plane by a factor of two for the F/48 relay and four for the F/96 relay with negligible spherical aberration or coma. The mirrors are all made of Zerodur and overcoated with $Al + MgF_2$ for a reflection efficiency exceeding 0.7 above 1200Å.

Near the exit pupil, in the F/96 relay are located four independently commandable rotating filter wheels. Two such wheels are located at or near the exit pupil in the F/48 relay. The filter wheels for the F/96 relay each have 12 equidistant working positions while for the F/48 relay each wheel has 8 equidistant positions. Each wheel has one clear position. These devices carry a full complement of wide, medium and narrow bandpass and neutral density filters, polarizing and objective prisms.

In order to fold the light beam back onto the detector and to focus the FOC, a cylindrical concave mirror is placed into the slowly converging beam past the filter wheels. This mirror also corrects for the residual off-axis OTA astigmatism and is made of the same materials as the primary and secondary mirrors. This mirror is mounted on a commandable focusing mechanism that allows it to internally compensate for variations in optical path length introduced by the OTA focus variations, FOC internal stability and by the differing optical thicknesses of the various optical elements on the filter wheels. The focusing mechanism changes the length of the optical path by ± 16 millimeters maintaining the position of the image on the detector typically within 0.05 millimeters whatever the location of the mirror along the stroke. The FOC focal plane is designed to coincide with the detector photocathode plane. The detector samples an area of 24.6 × 24.6 millimeter squared corresponding to 1024 × 1024 pixels, each ≅ 24 micron squared in size, averaged over the field of view.

Absolute image position on the FOC focal plane can be referred to a grid of 17 × 17 reseau marks, each 75 × 75 microns squared in size evaporated on the inner surface of the photocathode MgF_2 window. The overall wavefront distortion of the FOC+COSTAR optical system is less than $\lambda/10$ for the F/48 relay and the F/96 relay at $\lambda6328$Å.

In the F/48 relay, the beam from the folding mirror may be relayed by a removable toroidal convex mirror to a fixed spherical concave reflection grating which re-images a spectrum of a portion of the field of view onto the detector photocathode. This portion contains a fixed width rectangular slit that is located on the entrance aperture (see Figure 9). The grating works with a divergent beam in the Rowland condition at fixed wavelength ranges in the first (3600--5400Å), second (1800--2700Å), third (1200--1800Å) and fourth (900--1350Å) order at a resolution $\lambda/\Delta\lambda$ ≅ 1000. Only the 1150--1350Å portion of the fourth order spectrum can be measured in practice,
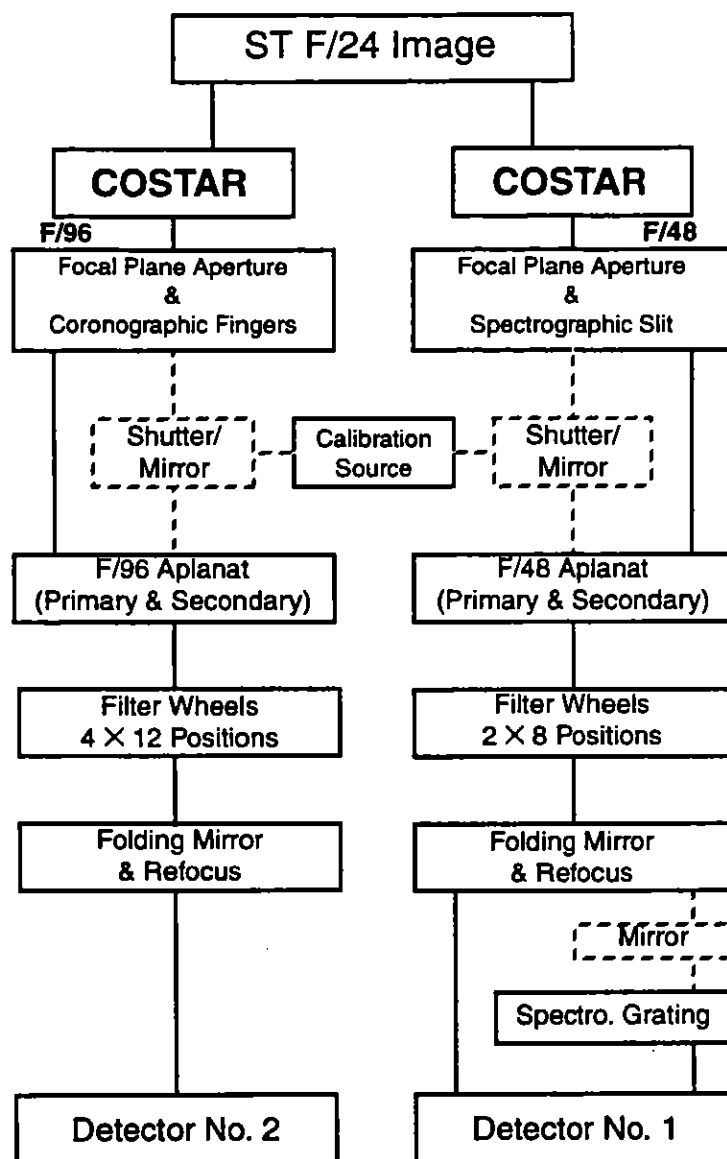
Figure 5. The Transfer Optics Block Diagram. The removable components are shown in the dashed frames.

of course, due to the MgF_2 cut-off of the detector. Wavelength range selection is accomplished by introducing suitable bandpass filters into the optical path of the F/48 relay or by using the objective prism (FOPCD) whose dispersion axis is oriented at $\cong 90°$ to the grating dispersion direction as a cross disperser.

4.2 FOCAL PLANE APERTURES

The two FOC field defining entrance apertures are each located in a plane tangent to an OTA focal surface at the center point of the aperture. The center of each aperture is located at a linear distance of 110 millimeters from the V1 axis. Each FOC channel of COSTAR redirects part of the OTA field of view into an FOC entrance aperture. For the F/96, the field is centered on a point
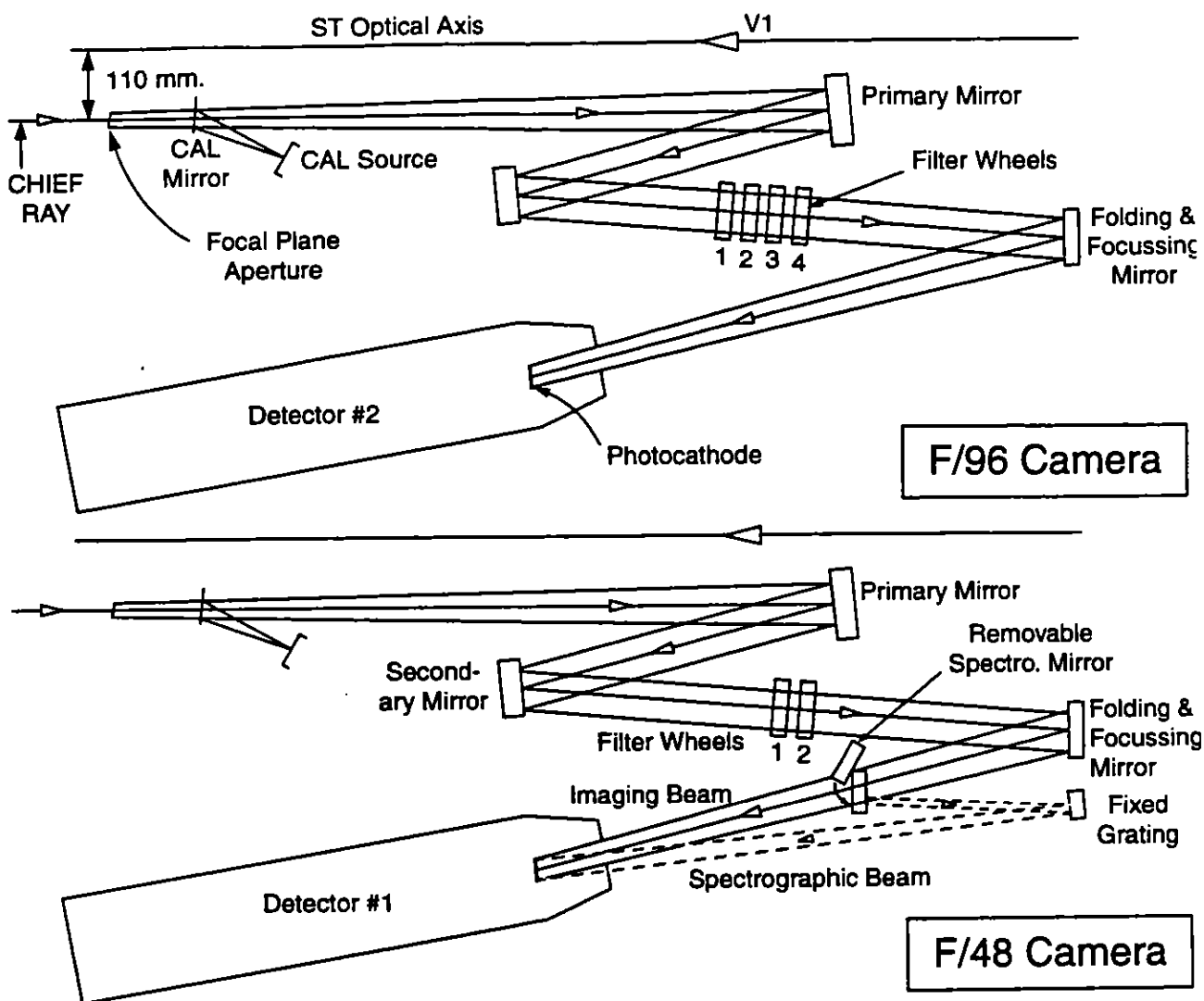
Figure 6. The schematic optical layout of the two cameras in the planes containing the V1 axis and the chief rays.

4.658 arcminutes from the V1 axis, while for the F/48 the field is centered on a point 4.312 arc-minutes from V1. The projections of these apertures onto the plane of the sky are shown in Figure 7; the dotted circles show the projection through the OTA only (i.e. the pre-COSTAR positions), while the solid circles are the positions through the COSTAR+OTA optics. In this figure, the V1 axis runs into the paper at the center of the WFPC2 field of view and V1, V2, V3, U2, and U3 are the HST axes defined in the Call for Proposals and Proposal Instructions. The observant reader will notice that in Figures 8 and 9 the V2-V3 directions are reversed with respect to pre-COSTAR versions of the FOC Handbook: this is because COSTAR forms an intermediate image between the M1 and M2 mirrors.

At the locations of the FOC entrance apertures, the OTA focal plane makes an angle of 10.05° with the normal to the ST axis. This plane is the object plane for the FOC optical relays. The COSTAR-corrected focal plane is inclined to this plane, which induces a field-dependent focus variation that is described more fully in Section 6.1.1. The axes of symmetry of the two FOC cam-

eras D96 and D48 that run through the center of the apertures, perpendicular to and intersecting on the V1 axis form an angle of 30°. The D96 axis forms an angle of 30° with the +V2 axis and D48 an angle of 30° with the +V3 axis.
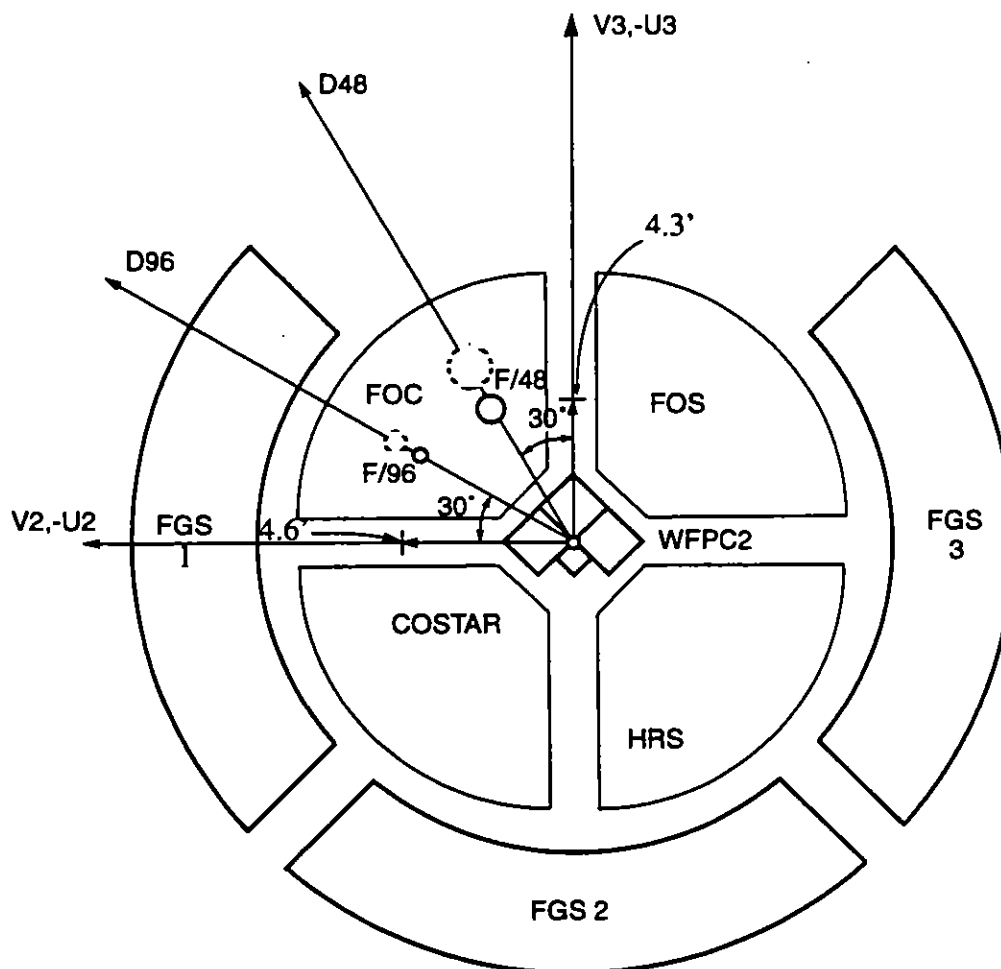
Figure 7. The location of the FOC entrance apertures on the HST focal plane projected onto the plane of the sky. In this perspective V1 is directed into the paper at the center of the WFPC2 pattern. V1, V2 and V3 form the HST right handed coordinate system defined in the Call for Proposals.

An expanded view of the two apertures in exactly the same perspective is shown in Figures 8 and 9. The camera aperture for the F/96 relay is a circular diaphragm of 10.5 millimeters in diameter corresponding to 24 arcseconds on the sky in the COSTAR-corrected field, centered at point O with two 2 millimeter-long protruding opaque metal fingers oriented $\cong 30°$ to the D96 line and parallel to the V2 axis. The finger on the right is 0.112 millimeters thick (0.25 arcsecond in the sky) while the other is 0.223 millimeters thick (0.5 arcsecond in the sky). The directions of increasing sample (S) and line (L) numbers for the extended SDS format define the image coordinate system with its center at point C_{96}. This system is aligned with the X, Y reference system

used to designate the orientation of the apertures on the sky in the Proposal Instructions. The corners ABCD of the 512 × 1024 zoomed format are marked on Figure 8. The large 14 × 14 arcsecond square marks the limit of the extended format. The opaque coronographic fingers are indicated by the hatched regions. The V1 axis is 4.658 arcminutes from O in the direction indicated to V1. The fully corrected field point for the F/96 relay coincides with C_{96}. Due to the presence of a reseau mark at C_{96}, the reference position for F/96 images has been moved off the center to R_{96}, located at (S,L) = (556,536) and shown in Figure 8.
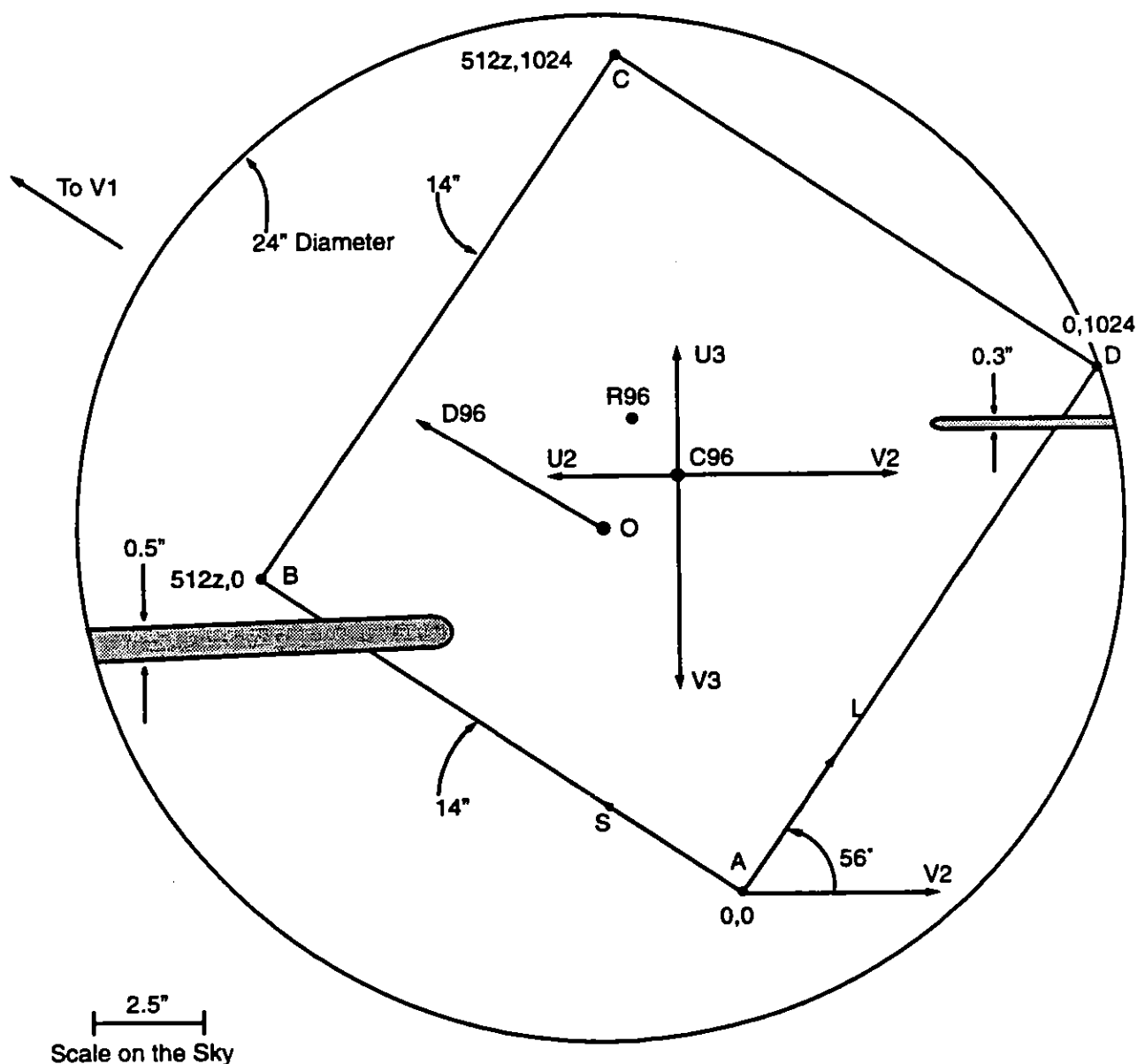
Figure 8. The camera entrance aperture for the F/96 relay projected onto the sky.
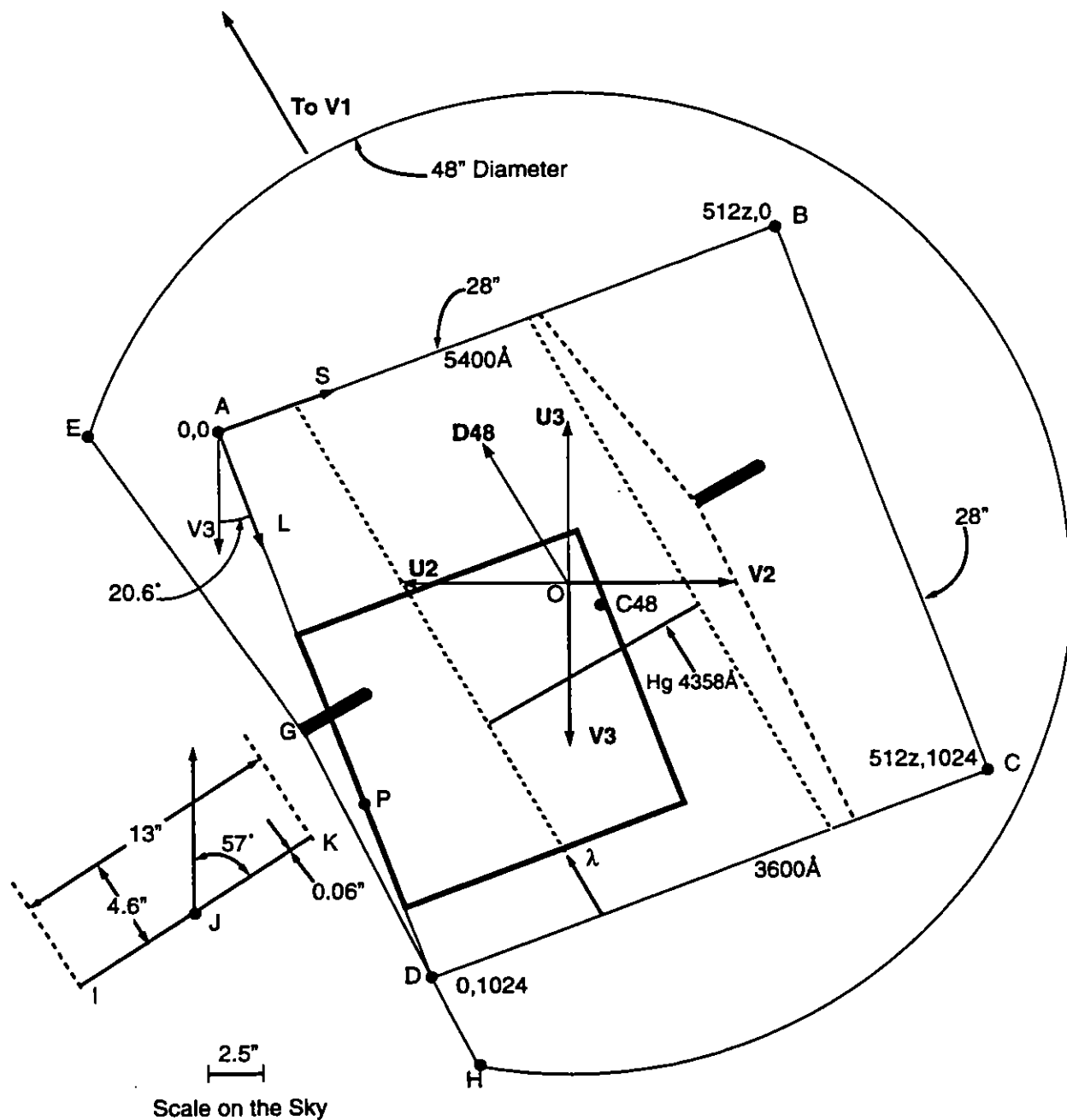
Figure 9. The camera entrance aperture for the F/48 relay projected onto the sky. KI along the spectrograph slit coincides with the reference axis x that is used to designate the orientation of the apertures on the sky in the Proposal Instructions. The point P is the optimally corrected field point for the F/48 relay and the new 512 × 512 imaging format is shown outlined with a **bold** line.

The F/48 entrance aperture is shown in Figure 9. The center O of the main aperture coincides with the center of the extended SDS format and lies on the sagittal focus while the center J of the slit lies on the tangential focus of the OTA.

Because of vignetting induced in the FOC by moving the OTA exit pupil from 7 meters to 530 millimeters from the F/48 entrance aperture, it is not possible to have the center of the extended field unvignetted as well as all of the slit. The best compromise, which maintains the utility of the long slit as well as providing an imaging field useful for spectrograph acquisitions, was to move the optimally corrected field point from the center of the extended format to the point P, which is where the hypothetical extension of the slit would meet the edge of the extended imaging format. The default 512 × 512 imaging format has therefore been moved to that corner of the extended format, and has been outlined in Figure 9. In this way, over half of the slit suffers less than 20% vignetting while the newly moved 512 × 512 imaging format is unvignetted over more than 80% of its area. Full vignetting contours are shown in Section 6.9.

The main aperture is essentially a circular diaphragm with a diameter of 21 millimeters corresponding to 48 arcseconds on the sky in the COSTAR-corrected field, except for an oblique truncation at points E and H. A thin, 0.15 arcsec wide opaque finger points to O from point G. A 5.689 millimeters (12.8 arcsecond) long, 0.028 millimeters (0.064 arcsecond) wide slit centered at J is located between points I and K. This slit forms the defining aperture of the spectrograph for the F/48 relay. The corners of the 512z × 1024, 28 × 28 arcsecond squared extended imaging format are given on Figure 9 as points A, B, C and D. When the spectrograph mirror is in place, the aperture is imaged onto the extended SDS format as shown in Figure 9 with the dashed lines representing the inner and outer edge of the spectrally dispersed image of the slit and the edge of the main aperture drawn for the specific case of the Hg line at 4358Å. The opaque finger (originally used for target acquisition) is indicated by the dark region. V1 is 4.312 arcminutes from P in the direction indicated to V1. A part of the dispersed main aperture falls in the right hand quarter of the extended format and may be eliminated by tailoring the observing format to the region inside the slit area. Wavelength increases in the direction indicated by λ from 3600Å to 5400Å in first order.

In order to predict with reasonable accuracy the location and orientation of an extended source in the FOC fields of view and to determine whether or when the required instrument orientations are compatible with the HST roll angle restrictions, it may be useful to locate with respect to the S, L axes on Figures 8 and 9 the celestial reference axes for that particular target and viewing configuration. To accomplish this, simply follow the procedures described in the Phase II Proposal Instructions.

To specify a particular orientation of the apertures with the ORIENT special requirement of the exposure logsheets (see Proposal Instructions for a more detailed description), place the object to be observed in the proper configuration on the entrance aperture shown in Figures 8 and 9. This will determine the desired positions of the N direction on the same apertures. The angle between this direction and the U3 axis drawn on these figures (measured E from N) is the angle to specify in this special requirement. See also Section 9.0 for the description of a user-friendly WWW tool to calculate the special requirement ORIENT.

The aperture configurations described in this section for the F/96 correspond to the position determined during the first in-flight tests of the FOC + COSTAR system and the Cycle 5 alignment calibrations. Additional calibrations will be performed in Cycle 6 to monitor the stability of these positions and to ensure that the FOC apertures alignment is maintained at better than 0.2". Alignment calibrations are planned in Cycle 5 for the F/48. Astronomical targets imaged so far

have been acquired with an accuracy of ~ 2". Also, targets have been acquired onto the 0.06" slit with an accuracy of 0.2", after a dedicated acquisition procedure. More robust calibrations are now in progress to make the slit acquisition less time consuming.

Actual images of the extended 512z × 1024 pixels pre-COSTAR F/48, pre-COSTAR F/96, and pre-COSTAR F/48 spectrograph fields obtained in orbit with external flat field illumination of the FOC entrance apertures are shown in Figures A1—A3 in the Appendix. The extended format 512z × 1024 pixel images have been dezoomed and displayed in a 1024 × 1024 pixel format. The occulting fingers, spectrograph slit, reseau marks appear clearly together with some blemishes and large scale response inhomogeneities. The latter are discussed in more detail in Section 6.9 and Chapter 11.

4.3 INTERNAL CALIBRATION SYSTEM

When the shutter is closed, an Al + MgF_2 mirror (see Figure 6) reflects the light beam from a light emitting diode (LED) calibration source into the optical path of the relay. The position of the source and the curvature of the mirror insure a quasi flat field illumination of the object plane. The unit consists of seven LEDs (two red, two yellow, two green and one blue) illuminating an integrating sphere. Their normalized emission spectra are shown in Figure 10. The unit is capable of illuminating both calibration mirrors simultaneously. Each LED output can be set to 256 separately commandable intensity levels. The calibration system will be used to determine the detector's intensity transfer function, the uniformity of response, the FOC response to visible light and the geometric distortion. A ground-based comparison between external and LED flat field illumination of the detectors at the same wavelengths shows that the spatial variations of LED illumination are less than ±3% peak to peak over most of the field of view. The only exception is due to one edge of the circular mirror on the back of the shutter for the F/48 relay preventing LED light from illuminating the upper left hand corner of the F/48 frame. The calibration unit does not experience the same vignetting of an external source. This must be taken into account when comparing internal and external flat fields. As mentioned previously, the F/96 detector is not expected to have any vignetting, nor is there any evidence of it. UV flat fields for the F/96 relay have been obtained using observations of the inner region of the Orion Nebula (see Section 6.9 for additional details).

4.4 FILTER WHEELS

The FOC has six commandable rotating filter wheels holding 58 optical elements and six clear apertures. Four wheels are on the F/96 relay and two on the F/48 relay. The filter wheels of the F/96 camera have 3 long pass, 9 wide band, 20 medium band, 2 narrow band and 5 neutral density filters. They also contain 3 polarizers and 2 objective prisms. The filter wheels of the F/48 relay contain 3 long pass, 8 wide band, and 3 objective prisms. A complete list of the optical elements ordered by increasing peak wavelengths λ_o is given in Table 3 for the filters of the F/96 relay and in Table 4 for the filters of the F/48 relay. In these tables, ID indicates the filter identification code, FW indicates the filter wheel number (1-4 for the F/96, 1-2 for the F/48), POS indicates the position of the filter on the wheel [information useful in accounting for exposure overhead times], λ_0 the wavelength at the peak of the curve representing the product of the filter transmission (T) with the OTA + FOC response function, (Q) described in Section 6.3, $\Delta\lambda$ the full width at half maximum of this curve, and $T(\lambda_0)$ is the filter transmission at λ_0, and $QT(\lambda_0)$ is $T(\lambda_0)$ multiplied by Q. Δm gives the magnitudes of attenuation of the neutral density filters at 3000Å. These filters are
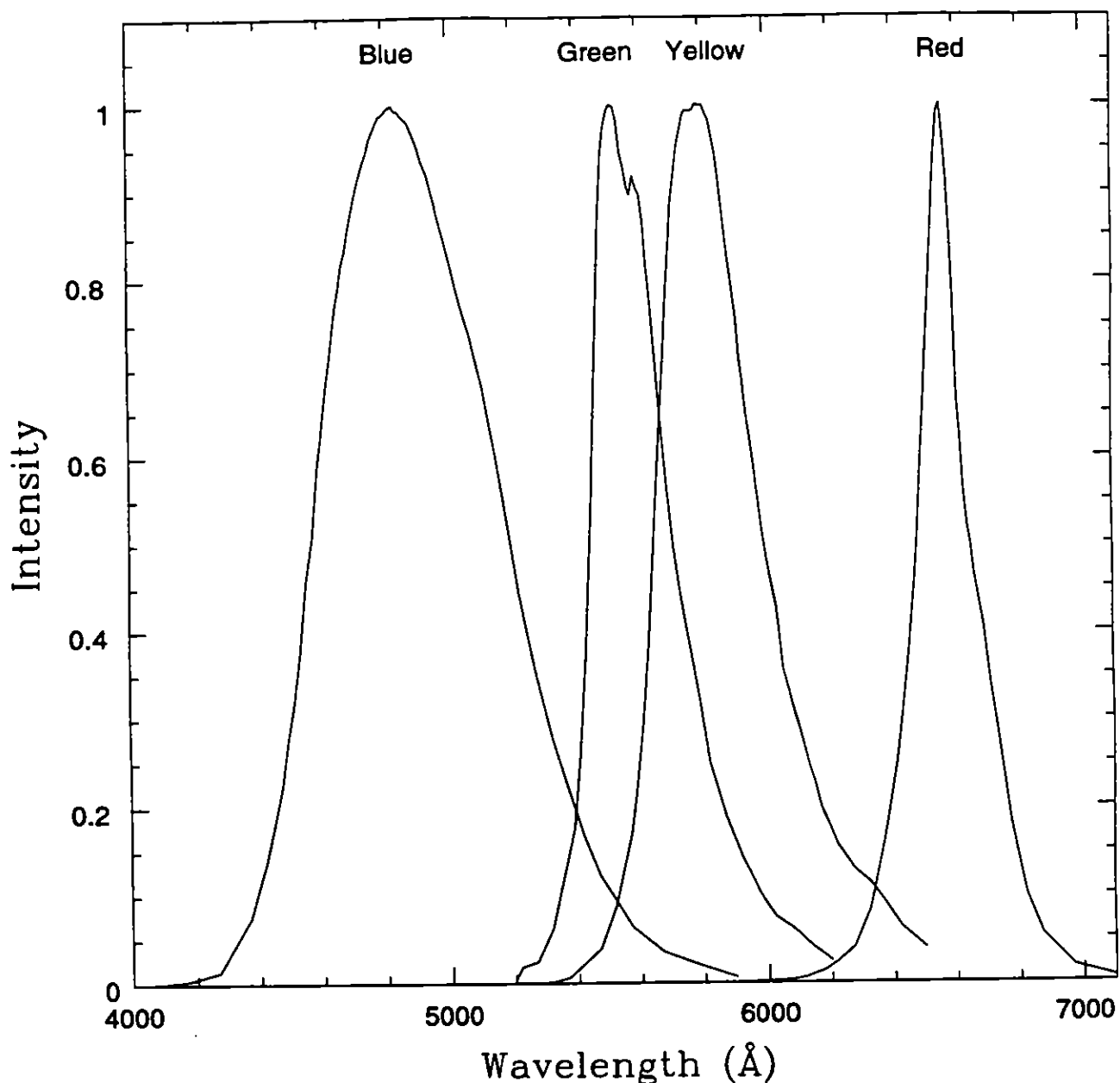
Figure 10. Normalized Emission Spectra of the Calibration LEDs.

placed on the wheels in such a way as to allow beam attenuation in increments of 1 magnitude from 1 to 9 magnitudes. A few filters have been found to exhibit faint ghost images and image shifts. These filters are flagged in the Comments column.

The filter wheel system of the F/96 camera allows, in principle, up to 12^4 or 20,736 and up to 8^2 or 64 different combinations of optical elements for the F/48 relay. Clearly, only a fraction of these will find a useful astronomical application. Observing configurations requiring more than one filter on the same wheel are not possible, of course. Filter positions on the wheels were carefully selected in order to minimize such needs. The time required to change some filter combinations may reach 3 minutes.

Table 3: F/96 Optical Element Characteristics Ordered by Peak Wavelength

ID	FW	Pos.	λ_0(Å)	$\Delta\lambda_0$(Å)	$T(\lambda_0)$	$QT(\lambda_0)$	Comments
F120M	3	3	1230	82	0.10	0.0008	Medium band
F130M	3	6	1280	88	0.10	0.0010	Medium band
F140W	2	6	1370	298	0.21	0.0028	Wide band
F140M	3	9	1400	178	0.08	0.0010	Medium band
F152M	3	4	1500	184	0.08	0.0010	Medium band
F165W	3	11	1700	910	0.28	0.0036	Wide band
F170M	3	8	1760	184	0.18	0.0021	Medium band
F175W	2	7	1730	716	0.24	0.0033	Wide band
F195W	3	10	2110	946	0.42	0.0079	Wide band
F190M	3	7	2000	276	0.15	0.0024	Medium band
F210M	3	2	2156	214	0.18	0.0042	Medium band
F220W	2	8	2280	480	0.39	0.0109	Wide band
F231M	3	12	2330	228	0.18	0.0058	Medium band
F253M	4	9	2550	236	0.18	0.0075	Medium band
F275W	2	9	2770	594	0.40	0.0196	Wide band
F278M	4	10	2800	316	0.26	0.0132	Medium band
F307M	4	11	3080	328	0.26	0.0161	Medium band
F130LP	4	7	3750	2202	0.92	0.0630	Long pass ($\lambda \geq 1300$Å)
F320W	2	10	3360	844	0.89	0.0599	Wide band, **Not Available** (see Fig 26)
F342W	2	3	3410	702	0.81	0.0546	Wide band, U filter
F346M	4	2	3480	434	0.58	0.0390	Medium band, u filter
F372M	4	6	3710	406	0.73	0.0494	Medium band, bar in PSF (see Fig 27c.)
F430W	2	4	3940	832	0.74	0.0469	Wide band, B filter
F370LP	2	2	4020	984	0.83	0.0500	Long pass ($\lambda \geq 3700$Å)
F410M	4	3	4100	194	0.58	0.0337	Medium band, b filter
F437M	4	12	4290	438	0.71	0.0350	Medium band, ghost
F470M	4	4	4710	212	0.79	0.0222	Medium band, v filter
F486N	2	11	4870	34	0.63	0.0155	Interference filter centered on H_β line
F502M	4	8	4940	530	0.82	0.0192	Medium band, ghost
F501N	2	12	5010	74	0.68	0.0151	Interference filter centered on [O III],ghost
F480LP	2	5	5100	744	0.82	0.0183	Long pass ($\lambda \geq 4800$Å), V filter
F550M	4	5	5460	188	0.77	0.0093	Medium band, y filter
F600M	1	5	5800	410	0.8	0.0059	Medium band

Table 3: F/96 Optical Element Characteristics Ordered by Peak Wavelength

ID	FW	Pos.	λ_0(Å)	$\Delta\lambda_0$(Å)	$T(\lambda_0)$	$QT(\lambda_0)$	Comments
F630M	1	6	6382	208	0.67	0.0009	Medium band
CLEAR	1,2,3,4	1	3700	2208	1.0	0.0680	Clear aperture
F8ND	1	2	3440	2100	9×10^{-4}	6×10^{-5}	Neutral density, $\Delta m = 8.0$, degraded PSF
POL120	1	3	3700	2180	0.91	0.0626	Polarizer, 120°
F2ND	1	4	3400	2176	0.19	0.0135	Neutral density, $\Delta m = 2.0$
POL0	1	7	3700	2180	0.92	0.0626	Polarizer, 0°
F4ND	1	8	3400	2176	0.03	0.0021	Neutral density, $\Delta m = 4.0$
F6ND	1	9	3200	2348	0.005	0.0003	Neutral density, $\Delta m = 6.0$
PRISM2	1	10	3700	2124	0.94	0.0640	Near UV objective prism (NUVOP)
POL60	1	11	3740	2076	0.92	0.0626	Polarizer, 60°
PRISM1	1	12	3700	2232	0.94	0.0638	Far UV objective prism (FUVOP)
F1ND	3	5	3400	2162	0.39	0.0259	Neutral density, $\Delta m = 1.0$

Table 4: F/48 Optical Element Characteristics Ordered by Peak Wavelength

ID	FW	Pos.	λ_0(Å)	$\Delta\lambda_0$(Å)	$T(\lambda_0)$	$QT(\lambda_0)$	Comments
F140W	1	5	1320	300	0.20	0.0047	Wide band
F150W	1	3	1400	628	0.23	0.0059	Wide band
F175W	1	6	1730	678	0.18	0.0035	Wide band
F195W	1	4	2110	1076	0.36	0.0112	Wide band
F220W	1	8	2250	480	0.36	0.0155	Wide band
F275W	2	6	2750	656	0.29	0.0163	Wide band
F130LP	2	7	3400	2722	0.94	0.0536	Long pass ($\lambda \geq 1300$Å)
F180LP	2	5	3400	2702	0.92	0.0528	Long pass ($\lambda \geq 1800$Å)
F342W	2	3	3400	706	0.83	0.0475	Wide band, U filter
F305LP	1	7	3450	1692	0.92	0.0509	Long pass ($\lambda \geq 3050$Å)
F430W	2	4	3950	938	0.75	0.0372	Wide band, B filter
CLEAR	1,2	1	3400	2732	1.0	0.0571	Clear aperture
PRISM3	1	2	3360	2722	0.96	0.0550	Far UV Cross Disperser Objective Prism (FOPCD)
PRISM2	2	2	3400	2704	0.88	0.0504	Near UV Objective Prism (NUVOP) Not Available
PRISM1	2	8	3400	2738	0.96	0.0548	Far UV Objective Prism (FUVOP) Not Available
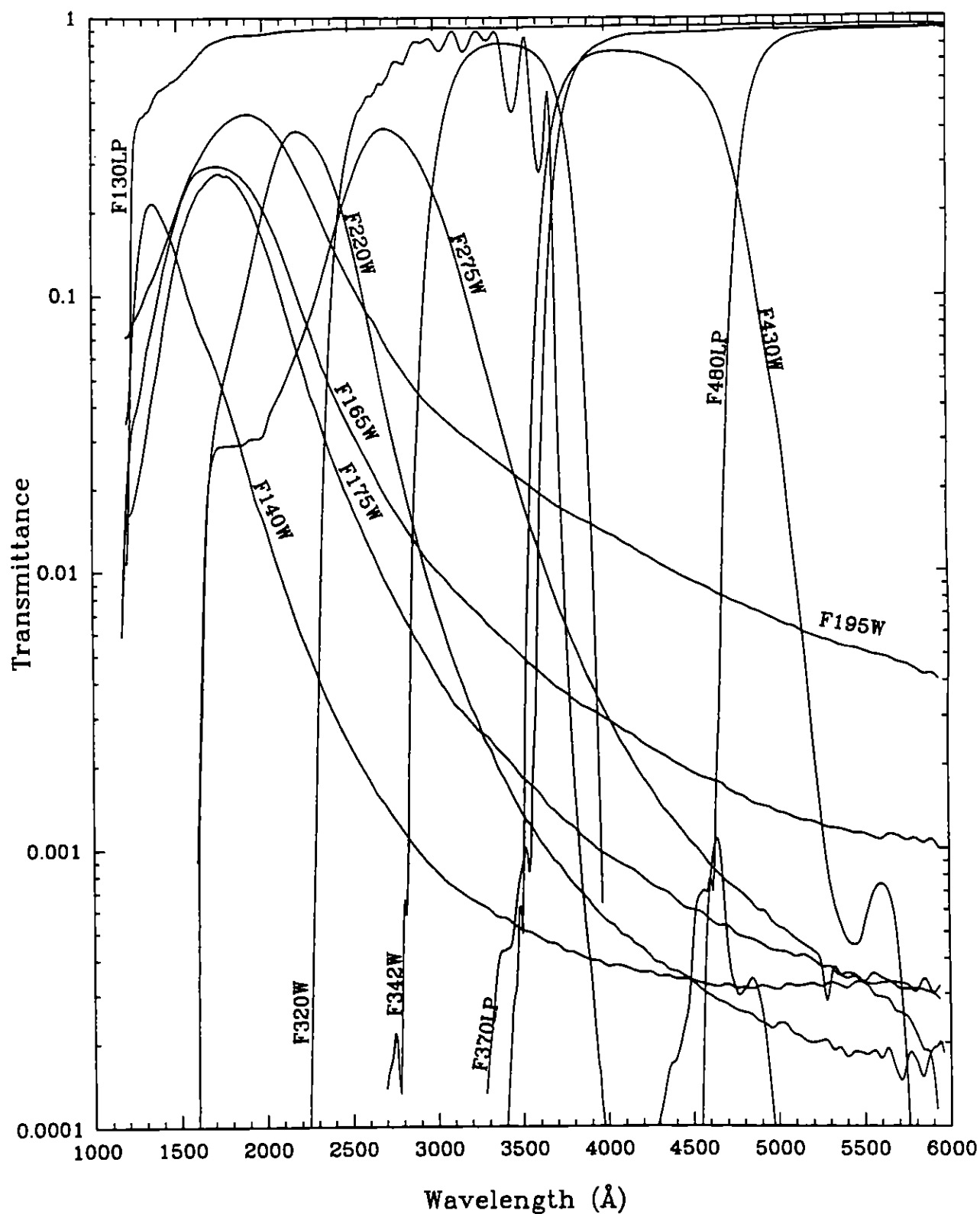
Figure 11. Transmittance of the long pass and wide band filters on the filter wheels of the F/96 relay as a function of wavelength.
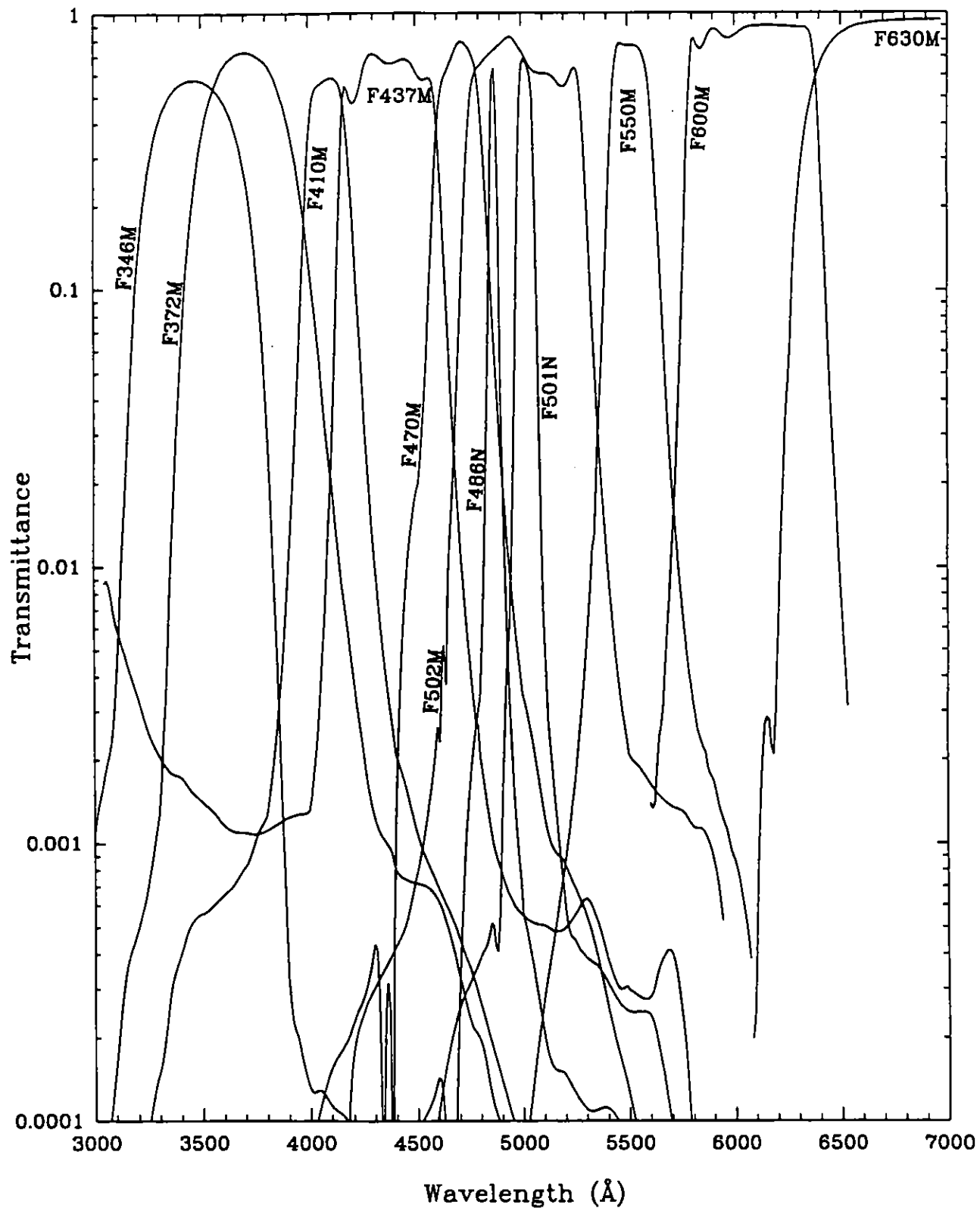
Figure 12. Transmittance of the visible medium and narrow band filters in the filter wheels of the F/96 relay as a function of wavelength.
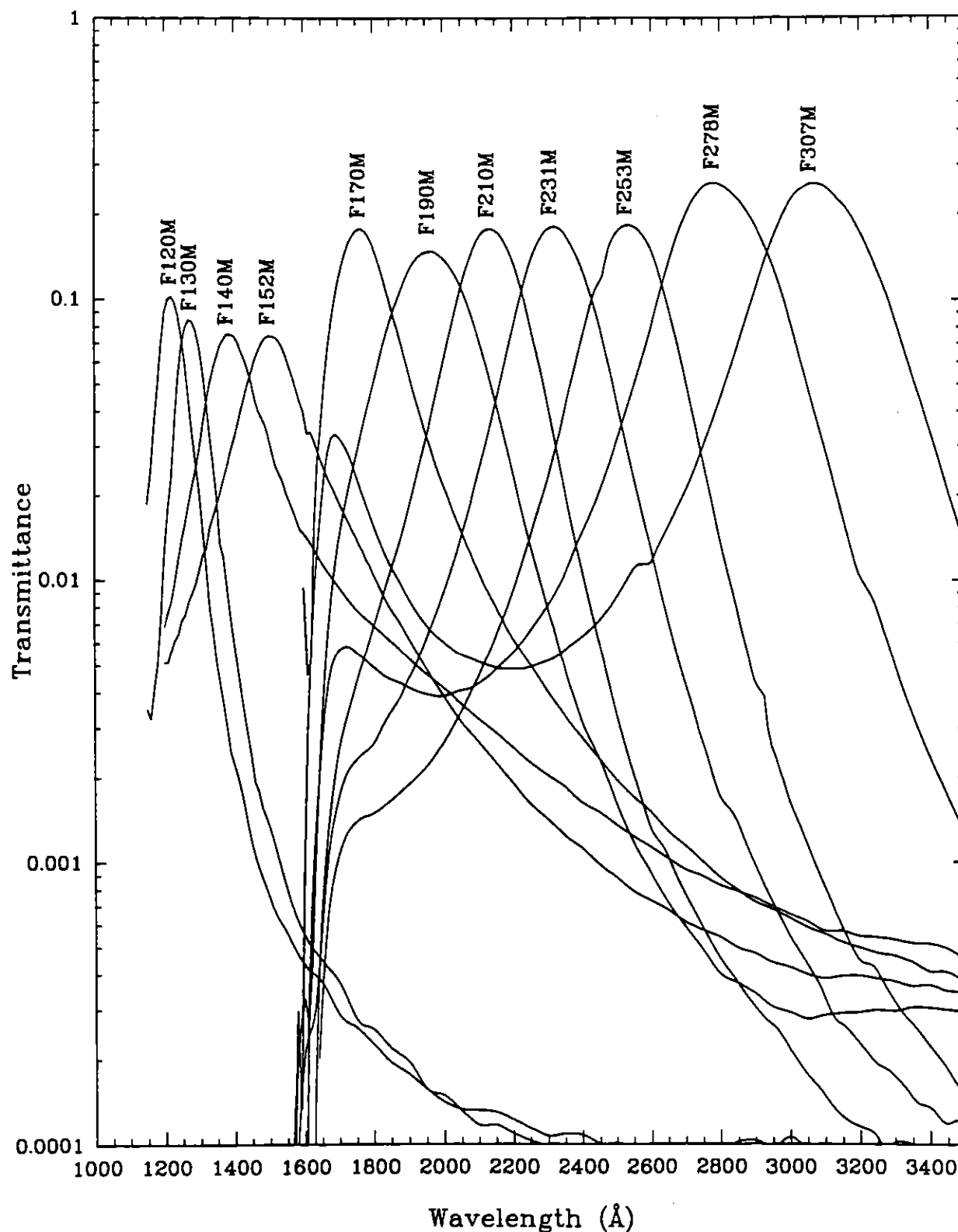
Figure 13. Transmittance of the UV medium band filters on the filter wheels of the F/96 relay as a function of wavelength. The F120M and F130M filter transmission curves remain essentially flat at 10^{-4} beyond $\cong 2500$Å.
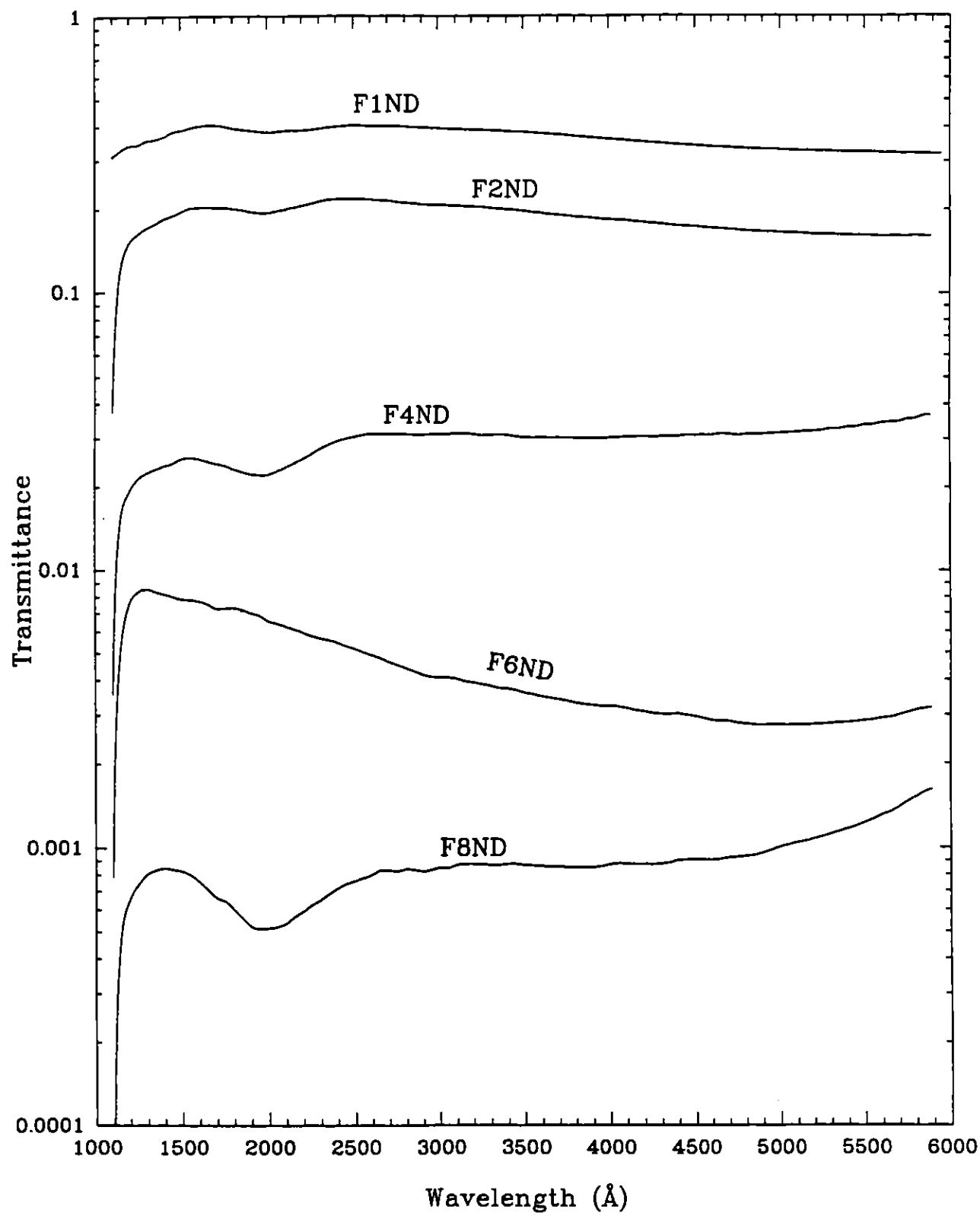
Figure 14. Transmittance of the neutral density filters on the filter wheels of the F/96 relay as a function of wavelength.
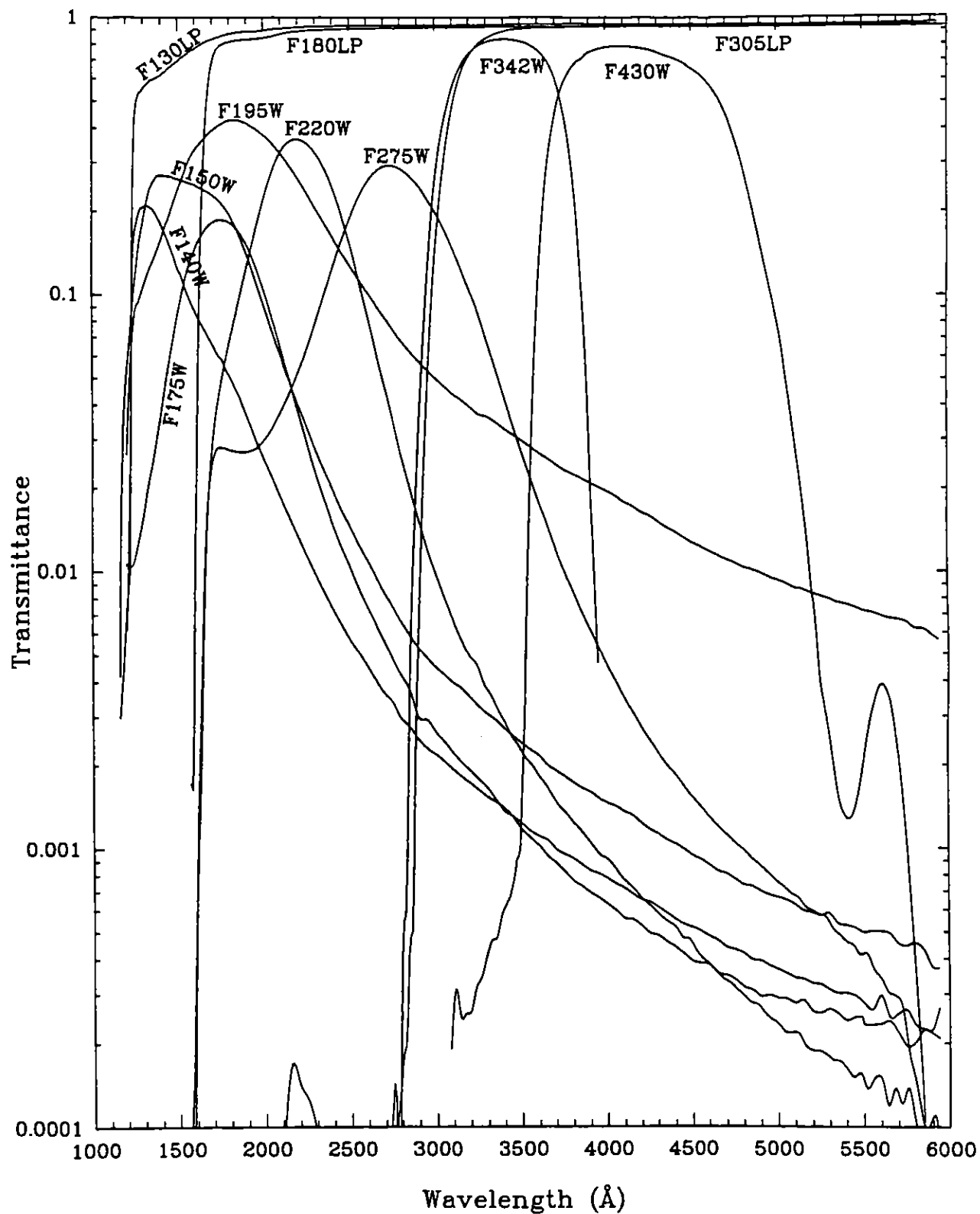
Figure 15. Transmittance of all the filters on the filter wheels of the f/48 relay as a function of wavelength.

4.4.1 Bandpass and Neutral Density Filters

In general, the long pass filters are Schott colored glass combined with a low pass filter, the wide band filters are metallic UV filters, the medium band filters are multi-dielectric multi-element with ZnS-Th F_4 layers, and the interference filters are multi-dielectric multi-element with ZnS chiolithe layers. The measured transmission versus wavelength curves for all filters and attenuators for the F/96 relay and the F/48 relay are shown in Figures 11—15. In order to suppress ghost images, the external faces of all mono-element filters are parallel to within 5 arcseconds or better. For multi-element filters the tolerance is 1 arcminute. The cemented elements have a wedge angle of 1° or less. In order to minimize losses in the modulation transfer function, the external faces are flat to $\lambda/5$ peak to peak at 6300Å and the internal faces in the multi-element filters are flat to $\lambda/2$ peak to peak. The refractive index is homogeneous to a level of $\Delta n < 2 \times 10^{-5}$ to be consistent with the $\lambda/5$ flatness constraint. These conditions have been complemented by the introduction of appropriate tilt angles of the different filter wheels themselves. Transmission non-uniformities are held to within ±5% over the whole surface.

The transmission curves described in Figures 11—15 are the result of ground calibrations performed before the HST launch. For the neutral density filters only (five available in the F/96 camera), a calibration program has been recently carried out to verify that the transmission factors match their ground-based measurements. Preliminary results indicate that the F1ND (1 magnitude) and F2ND (2 magnitude) filters behave roughly as expected. Figures 16a and 16b show post-COSTAR photometric measurements of stars in the globular cluster ω Cen taken through the F430W filter and varying numbers of ND filters. Above the photometric cutoff, where the flux measurements are minimally affected by noise, the ratios of count rates measured with and without the F1ND and F2ND filters in the beam are close to nominal. The F4ND filter appears to be within 20% of nominal, and measurements of the F6ND and F8ND filters, based on data of poorer quality, suggest that their throughputs may be low by 20-40%. These numbers should be taken with caution since they have been measured at only a couple of wavelengths, and are extremely difficult to determine accurately, particularly for the larger neutral density values.
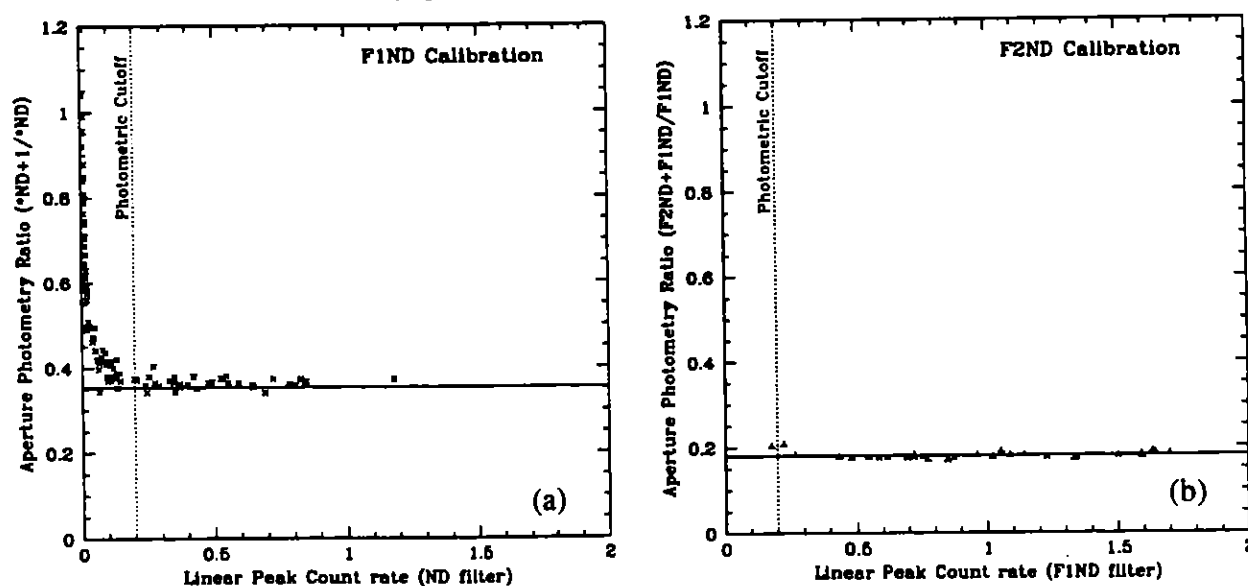
Figure 16. Ratios of point-source count rates through different ND filter combinations. (a) combinations isolating F1ND, (b) combination isolating F2ND

Table 5: Filter Image Shifts

Filter	ΔX	ΔY
F120M	=0	=0
F130M	0	0
F140W	-1	2
F140M	0	0
F152M	0	0
F165W	1	1
F170M	0	0
F175W	-1	1
F190M	1	0
F210M	1	0
F220W	-1	2
F231M	1	-3
F253M	-1	3
F275W	-1	2
F278M	-2	4
F307M	-2	5
F320W	-73	46
F342W	-1	-2
F346M	-5	6
F372M	-4	6
F430W	1	8
F370LP	0	2
F410M	-12	17
F486N	-6	16
F502M	-1	-7
F501N	11	0
F480LP	-1	1
F550M	-1	-5
F600M	24	11
F2ND	1	0
F4ND	0	-1
F6ND	0	0
F1ND	0	0

In addition, it is known that some filters shift the apparent position of the target in the field of view. In some instances, the shifts can be greater than 0.1". In Table 5, we list the shifts measured for most filters in Table 3, in pixels. The shifts were determined relatively to the position of the same target in an F120M image, and they are affected by measurement errors of ±1 pixel. The use of filters that produce large shifts may have an impact on calculating positional offsets (POS TARG), in observations taken with small formats (such as the 256x256 format), on the final position of the target after an INT ACQ, and on the analysis of objective prism spectra if compared to a direct image. In these circumstances, the filter shifts should be taken into consideration to ensure that the target is actually placed at desired position in the image.

4.4.2 Objective Prisms

The objective prisms consist of either a single 30 millimeter diameter, 3 millimeter thick wedged crystal of MgF_2 (the FUVOP and FOPCD, called PRISM 1 and PRISM 3 in the Instructions) or a combination of two wedged crystals of MgF_2 and SiO_2 glued together (the NUVOP called PRISM 2 in the Instructions). The former operates down to 1150Å with a wavelength resolution $\lambda/\Delta\lambda \cong 100$ at 1500Å while the latter has a dispersion $\lambda/\Delta\lambda \cong 250$ at 2500Å but transmits only above $\cong$ 1600Å. All of the prisms disperse in a direction oriented roughly anti-parallel to the increasing line number (L) direction except FOPCD on FW # 1 of the F/48 camera that, instead, disperses in a direction roughly perpendicular to L or about 90° to the others. This last one is meant as a cross disperser (CD) for the long slit spectrograph (see Section 4.5). The MgF_2 prisms (FUVOP and FOPCD) on the F/48 relay (Prisms 1 and 3) are both preceded by a 3 mm. thick CaF_2 window in order to reduce geocoronal Lyman alpha contamination. These prisms, therefore, have negligible transmissions below $\cong$ 1250 Å. The essential features of the FOC objective prism facility are listed in Table 6 and illustrated schematically in Figure 17 for the FUVOP of the F/96 relay. The left hand side of this diagram corresponds to a view of the extended format for the F/96 relay in the same orientation as the one shown in Figure 8 and approximately to scale. The direction of dispersion of the prism is represented by the vector I emanating from the center C_{96} of the format and making

Table 6: FOC Objective Prism Characteristics

F/96 FUVOP θ = 8° x(pix); R(Å/pix) T	F/96 NUVOP θ = 11° x(pix); R(Å/pix) T	F/48 FUVOP θ = 12° x(pix); R(Å/pix) T	F/48 NUVOP θ = 12° x(pix); R(Å/pix) T	F/48 FOPCD θ = 100° x(pix); R(Å/pix) T	λ(Å)
-416;1.7 0.44					1200
-369;2.7 0.58		-183;5.1 0.61		-208;5.1 0.62	1300
-339;4.1 0.64		-168;8.8 0.69		-191;8.8 0.70	1400
-320;6.4 0.73		-159;13.7 0.76		-181;13.7 0.76	1500
-306;9.5 0.85	-570;0.6 0.06	-153;19.5 0.82		-174;19.5 0.82	1600
-297;13.0 0.88	-425;0.78 0.63	-149;25.9 0.86		-169;25.9 0.86	1700
-289;16.8 0.91	-315;1.0 0.77	-145;33.0 0.9	-50; 0.78	-165;33.0 0.9	1800
-284;21.0 0.92	-232;1.4 0.79	-142;40.7 0.92	-46; 0.79	-161;40.7 0.91	1900
-280;25.0 0.93	-173;1.7 0.80	-140;49.2 0.92	-32;15.7 0.8	-159;49.2 0.92	2000
-276;29.6 0.95	-122;2.2 0.82	-138;58.6 0.94	-19;10.5 0.82	-157;58.6 0.93	2100
-272;38.8 0.95	-83;3.0 0.83	-137;69.0 0.95	-11;11.6 0.84	-156;69.0 0.94	2200
-265;50.4 0.96	-6.3;5.1 0.86	-133;107.6 0.96	5;20.9 0.86	-151;107.6 0.96	2500
-258;92.3 0.96	62;10.9 0.88	-130;203 0.96	23;41.8 0.88	-148;203 0.96	3000
-254;161 0.94	99;17.4 0.94	-128;348 0.97	33;67.9 0.89	-145;348 0.96	3500
-252;279 0.94	121;33.1 0.94	-127;55 0.98	40;99 0.89	-144;554 0.97	4000
-249;526 0.94	145;58.6 0.94	-125;1192 0.98	47;168 0.89	-142;1192 0.97	5000
-248;1562 0.92	-158;81.0 0.9	-125;2192 0.98	52;247.5 0.85	-142;2197 0.85	6000

an angle θ with -L with θ increasing clockwise from -L. The spectrum of an object located at C96 will lie along the line defined by I . The position of any specific wavelength is defined then by giving the linear coordinate x in pixels from C96 on this line with negative values for positions above C96 (towards +L), positive below it (towards -L) consistent with the I directions shown in Figure 17.

A blow-up of this spectrum extending from 1200 to 6000 Å as dispersed by the FUVOP is shown on the right hand side of this figure where the solid curve gives the position x along I of any wavelength for this case. The reciprocal of the slope of this curve yields the resolution R in Å/pixel given in the figure for several representative wavelengths. Values of the linear coordinate $x(\lambda)$, $R(\lambda)$, $T(\lambda)$ the transmission of the prism and the value of θ for each prism is listed in Table 6 as a function of wavelength. Please note that the angle θ for the prisms of the F/96 relay increases clockwise from -L while it increases counterclockwise from -L for the prisms of the F/48 relay due to the different orientation of the F/48 format shown in Figure 9. The position of the entire dispersed FOV with respect to the undispersed FOV is also shown in Figure 17. The former is displaced upwards by 5.88 millimeters at the red limit at 6000Å at the upper edge and 9.96 millimeters at the far UV limit at 1200Å at the lower edge of the field.
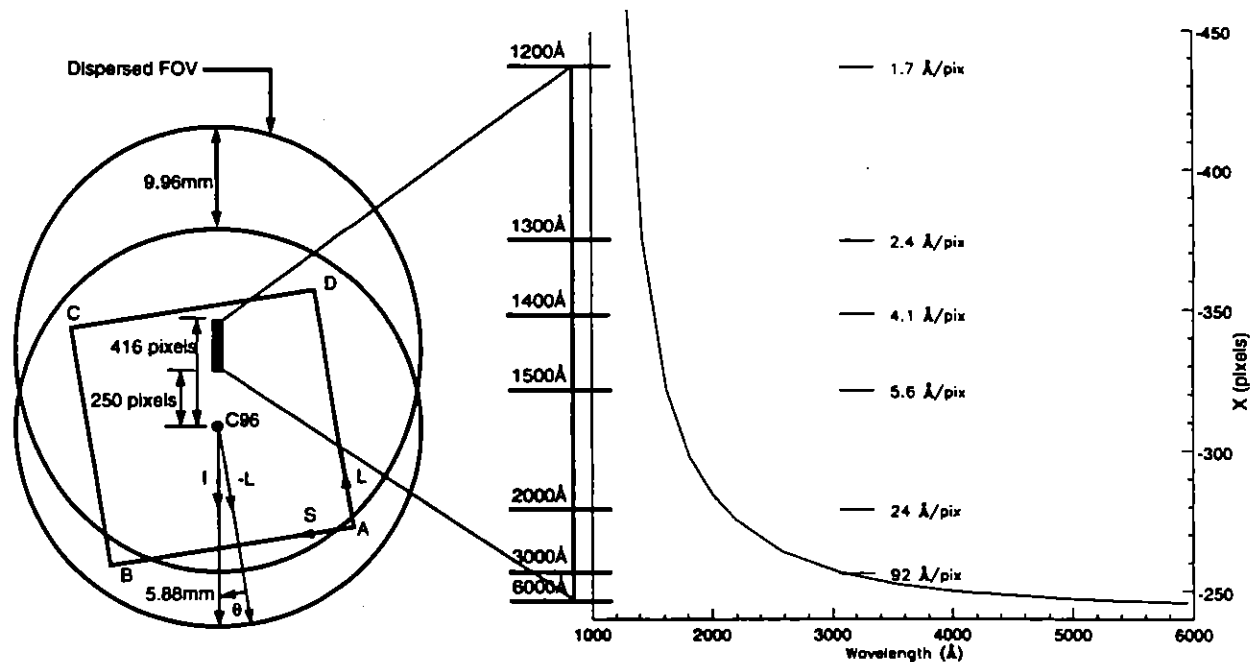
Figure 17. Optical layout of the focal plane of the F/96 relay with the FUVOP inserted in the beam. The star is assumed located at C96 in the entrance aperture of Figure 7.

A composite image showing the central 256 × 512 pixels of the undispersed image of a star in the post-COSTAR F/96 256 × 1024 image and its associated Far-UV objective prism spectrum is shown in Figure A4 in the Appendix. In this 256 × 1024 centered format, the star was placed well below the center of the format so that in the next image, the dispersed FUVOP spectrum is roughly centered. The two images were then co-added to produce Figure A4. It should also be apparent from an inspection of Figure 17 and Table 6 that careful consideration must be given to the positioning of the format and/or the target object in the format in order to ensure that the ensu-

ing spectrum falls on the correct part of the frame. This is especially critical for the FUVOP's that have a large offset and a spectrum length which is a sizable fraction of a typical field of view. The simplest way to handle this problem is through judicious use of the POS TARG special requirement described in the Proposal Instructions. Suppose, for example, that one desires to place a particularly interesting feature in the spectrum of an object located at $\cong$ 1500 Å close to the center of the image for the F/96 relay listed in Table 7 using the FUVOP. According to the data given in Table 6 and the situation illustrated in Figure 17, one would specify a POS TARG 0, -4.6 because 1500Å falls 320 pixels or 4.57 arcseconds from the undispersed position of the object in the positive Y(or L) direction specified in the Proposal Instructions.

4.4.3 Polarizers

The FOC polarimeter consists of three MgF$_2$ double Rochon prisms located on FW1 in the F/96 relay. Each prism consists of an optically contacted double Rochon prism combination acting as a three element birefringent beam splitter. The pass directions for the electric vector of the prisms are at 0°, 60°, and 120°, counterclockwise from the image X axis (-S direction) as projected onto the sky. A schematic drawing of the device is shown in Figure 18. These values are known to an accuracy of approximately 3° (see Section 11.2.6 for more details).

The optical axes of the outer components A and C are oriented perpendicular to the optical beam axis while the central component B has its optical axis parallel to the beam axis. The entrance face is at the base of the central prism. In this configuration, the ordinary ray is transmitted without deviation while the extraordinary rays are deviated by the interface between the outer and central prisms. Thus, three exit beams emerge from the polarizer. The orientation of polarization is parallel to the face of the octagon to within ±5 arcminutes and the external faces are parallel to within ±5 arcseconds. This ensures that the wavefront distortion is less than $\lambda/10$ at λ 6328Å. The beam deviation δ depends on the ordinary and extraordinary indices of refraction and the prism wedge angle. These parameters were chosen such that the angular separation of the beams yield a central undeviated 7 arcseconds squared image without overlap of the two orthogonally polarized beams. Thus, δ= 1.155° for λ=1300Å and 1.165° for λ=6328Å. In practice, overlap of the beams has not been seen even when the full (512x1024(z)) format is used. The pass directions for the electric vectors on the focal plane of the F/96 relay are located as shown in Figure 19 for the three prisms.

The major principal transmittance (T$_{MAJ}$) of the undeviated beam through the three prisms and the minor principal transmittance (T$_{MIN}$) of the normal nonpolarized light are given in Figure 20. Notice that one of the polarizers (POL60) does not transmit below $\cong$ 1800Å. There are limitations on the accuracy which is attainable with this facility, but current calibrations have attained accuracies for relative photometry of approximately 5% (1σ), with more details available in Section 11.2.6. A major factor is that the three different polarizers have somewhat different throughputs, even longward of 3000 Angstroms. While the filter transmissions have been measured, filters do change with time, and color variations in the source will result in small differences in the actual throughput. In addition, the light reaches the polarizers only after reflection off the OTA, COSTAR and the FOC primary and secondary mirrors (but before the fold mirror). Each of these six reflections is at a non-zero angle of incidence, ranging from a few minutes of arc for the OTA primary to about 11.5° for the FOC secondary. Such reflections introduce a phase shift in incident polarized light and a slight instrumental polarization which is predicted to be less than 1%. The reflections off the COSTAR optics are at angles of incidence that are smaller than the angles for
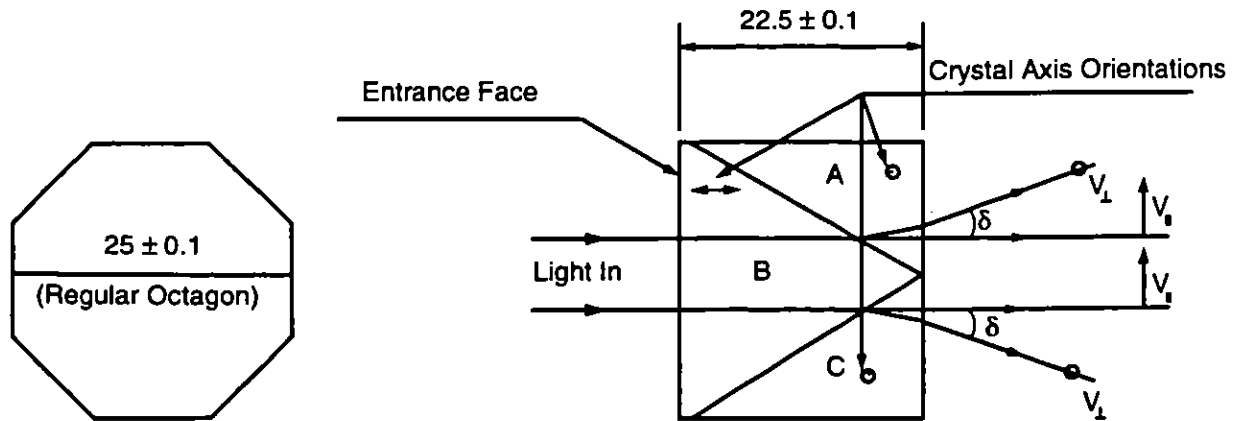
Figure 18. The Physical Layout of the FOC Polarizers. Dimensions are in millimeters.
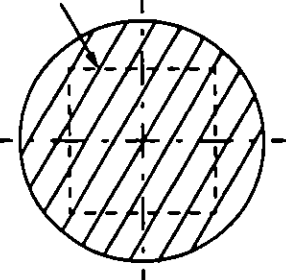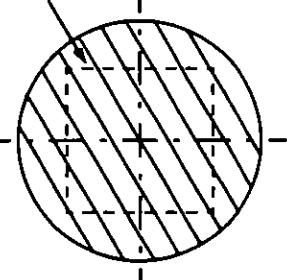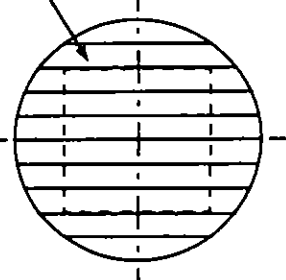
Figure 19. Image configurations on the focal plane of the F/96 relay for the three polarizers.

the FOC optics, resulting in performance comparable to the pre-COSTAR case.

Several factors complicate analysis of polarization data and limit the accuracy achievable. Firstly, the PSFs through the polarizers are all rather different from the PSF obtained without the polarizers, and also different from each other. This means that the encircled energy as a function of radius is different for each polarizer, so the apparent "polarization" of a compact source will appear to change with the size of the photometry aperture. While the aperture corrections are in principle calibratable, the dependence on wavelength and on small focus differences that are a factor for all observations adds an unpredictable element to the calibration. These differences are only at the level of a few percent, but they mean that high precision (1%) polarimetry of compact isolated sources is difficult if not impossible. Extended sources generally fare better in this respect; since it is often necessary to spatially bin the data to achieve the desired signal/noise ratio these differences in the PSF, as well as small-scale flatfield irregularities, are reduced in impor-
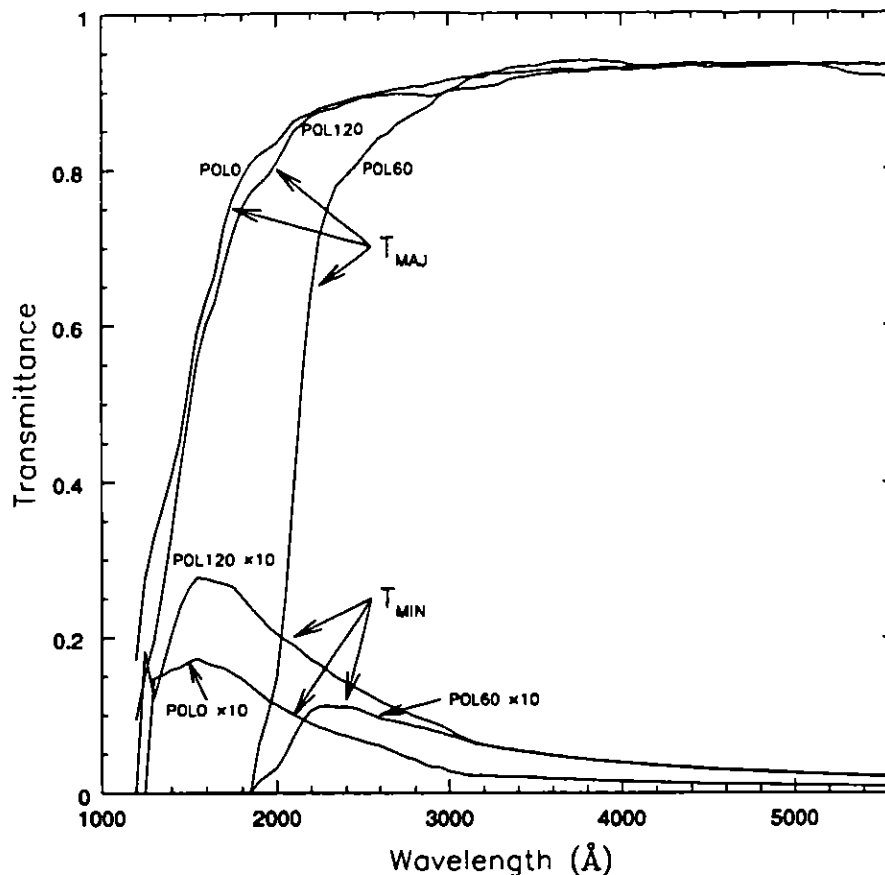
Figure 20. The major principal transmittance T_{MAJ} and the minor principal transmittance T_{MIN} of the three FOC polarizers as a function of wavelength.

tance.

Overall, the 1σ accuracy achievable for isolated point sources through the polarizers is approximately 4-5% in the degree of polarization. For extended sources (size $\geq$ 10x10 pixels), one can in general do better, achieving 1σ accuracies of 2% or so. These calculations assume of course that sufficient photons are detected that photon statistical errors are not the dominant source of error.

In principle, one could imagine a very careful observational program that might be able to beat down some of the error sources. One could split the observations into a large number of exposures to try to average out the orbital focus variations, and perhaps execute small positional offsets between exposures to try to smooth out the small-scale flatfield structure. But there would still remain the uncertainties in the calibration of the polarizers' transmissions, polarization efficiencies and angles that would require a prohibitive amount of telescope time to calibrate to the same level.

4.5 LONG SLIT SPECTROGRAPHIC FACILITY

The F/48 camera will be made available again in Cycle 7, FOR LONG SLIT SPEC-TROSCOPY ONLY.

This facility consists of the following four elements:

1.a rectangular (0.063 × 12.5 arcsecond) slit placed on the F/48 camera entrance aperture at the OTA tangential focus as shown in Figure 9,

2.order sorting bandpass filters and/or a cross dispersing objective prism on the filter wheels of the F/48 relay,

3.a removable toroidal convex mirror which picks off the F/48 beam between the folding mirror and the DHU and reflects it towards

4.a fixed spherical concave reflection grating which reimages the slit spectrum onto the detector photocathode as shown in Figure 6.

The last two optical elements are slightly tilted and decentered with respect to the optical relay axis of the F/48 in order to center the spectrum of the slit onto the photocathode. Since, as shown in Figure 9, the slit is considerably offset from the extended 28 × 28 arcseconds squared normal imaging field, its image falls outside the scanned area of the photocathode in the normal imaging mode. Only when the convex mirror is placed into the F/48 beam does the dispersed image of the slit become visible on the scanned area in the position indicated in Figure 9. The effective wavelength range of the device in first order is 3600--5400Å, in second 1800--2700Å, in third 1200--1800Å and in fourth 900--1350Å. The MgF_2 window of the detector limits this last range to 1150-1325Å.

The spectrograph mirror and the grating are both made of Zerodur overcoated with Al + MgF_2 with a reflection efficiency exceeding 0.7 beyond 1200Å. The grating is ruled with 150 grooves mm^{-1} and a blaze angle of 1.94° for maximum efficiency at 4500Å in first order. Its radius of curvature is 94cm and the angle of diffraction is 2.6°. This implies a linear dispersion at the photocathode of 71, 36, 24, and 18 Å mm^{-1} and, with a beam diameter of $\cong$ 20 mm., a theoretical resolving power of $\cong$ 3000, 6000, 9000 and 12000 for the four orders, respectively. The FOC spectrograph resolution, however, is limited, in practice, by the slit size and the OTA Point Spread Function (PSF) that correspond to $\cong$ two to three 24 micron pixels. Using the Rayleigh resolution criterion, the actual resolving power of the instrument is $\cong$ 1150 in all orders with a spectral resolution of 4, 2, 1.3, and 1Å for first, second, third, and fourth orders respectively. These values have been confirmed by ground-based calibration using line source stimulation.

Both the spectrograph mirror and the grating work with unit magnification. The convex mirror corrects the astigmatism introduced by the spectrograph's optical elements. The resulting image is nearly free of astigmatism and image tilt with respect to the photocathode plane. The fixed grating configuration of the long slit spectrograph implies that light from all orders falls simultaneously on the same area of the detector. Because of the limitations of the UV bandpass filters, any order may be contaminated with light from another, resulting in possible ambiguities in line identification and degradation of achievable signal to noise ratio (S/N) due to line or continuum overlap. This can be a serious problem in some applications, especially those involving objects with a bright visible spectrum where the spectrograph's overall quantum efficiency peaks.

Even in the most complicated situations, however, it is still possible, at least in principle, to separate the different orders by executing a number of exposures with judiciously chosen bandpass filters. Light from the first order, for example, can be unambiguously identified by means of the F305LP filter that completely blocks radiation below 3000Å. Since the filter transmissions are well known, shorter wavelength information can be recovered from a confused spectrum by appropriately subtracting the calibrated data. The F220W for the second order, F150W for the third and F140W for the fourth may be considered as the standard FOC spectrograph order sorting filters but others may be selected, at the discretion of the observer, instead of or in addition to

these for more specialized applications. This procedure can always be used at the expense of increased observation time required by the multiple exposures and of degraded S/N due to the effectively increased background uncertainty. For extended sources larger than 1.6 arcsecond in size this is the only viable alternative.

For objects of limited spatial extent (including point sources), the four overlapping orders can be spatially separated by using the FOPCD objective prism as a cross disperser. The position of the four orders on the detector field of the F/48 relay in this case is shown in Figure 21. The prism dispersion direction PD is orthogonal to the grating dispersion direction GD and close to antiparallel to the increasing sample number direction S. The reader is referred to Figure 9 for a broader perspective of this viewing configuration. The largest achievable physical separation between orders is 7 pixels (0.20 arcseconds) between the first (I) and second (II), 15 pixels (0.42 arcseconds) between the second and third (III) and 36 pixels (1.01 arcseconds) between the third and fourth (IV) order. The background is significant only for wavelengths which are harmonics of bright geocoronal lines like OI, 1304Å. This option is very attractive because of its high efficiency due to the spectral multiplex gain of a factor of 4 and to the gain of a factor of 3 -- 5 resulting from the elimination of the bandpass filters. The CaF_2 blocking filter on the FOPCD effectively removes the contaminating effect of the bright geocoronal line at Lyman α at 1216Å.

The open area to the right of the dotted line in the extended format of the F/48 relay in the spectrograph mode shown in Figure 9 and Figure A3 of the Appendix is normally blanked out by selecting the 256z × 1024 format. It should be kept in mind, however, that dispersed light from this part of the aperture is still falling on the photocathode and, if the field here is very bright (a bright galactic nucleus, or the central part of a nebula, for example), some contamination of the right edge of the slit spectrum due to scattering should be expected.

4.6 DETECTORS

The transfer optics described in Section 4.1 relay the image produced on the OTA focal plane to the photocathode of a two dimensional photon counter drawn schematically in Figure 22. The detector consists of three basic parts: a three stage image intensifier tube, a coupling lens, and a TV camera tube.

4.6.1 Image Intensifier and Coupling Lens

The intensifier is an EMI 9614 three stage tube magnetically focused by means of a permanent magnet. The first-stage photocathode (like the following two) is a hot bialkali for the highest quantum efficiency in the UV-blue region and the lowest dark-count rate at 17°C. It has a useful diameter of 40mm and is deposited on a MgF_2 input window.

The photoelectrons generated at the first stage are accelerated by a 12 kilovolt potential and impinge on a P11 phosphor layer coupled by a 4 micron thick mica membrane to the second photocathode. This amplification process is repeated in the second and third stages to achieve an overall photon gain of 1.3×10^5. Focusing of the intensifier electrons is accomplished with a carefully shaped permanent magnet assembly and a trimcoil is added around the third stage for fine adjustments.

The limiting spatial resolution of the intensifier is 35 line-pairs per millimeter. The dark current at an ambient temperature of 17° C is less than 10 counts $cm^{-2} s^{-1}$ (10^{-4} counts $pixel^{-1} s^{-1}$ in the normal mode). Both of these characteristics are essentially limited by the first stage of the
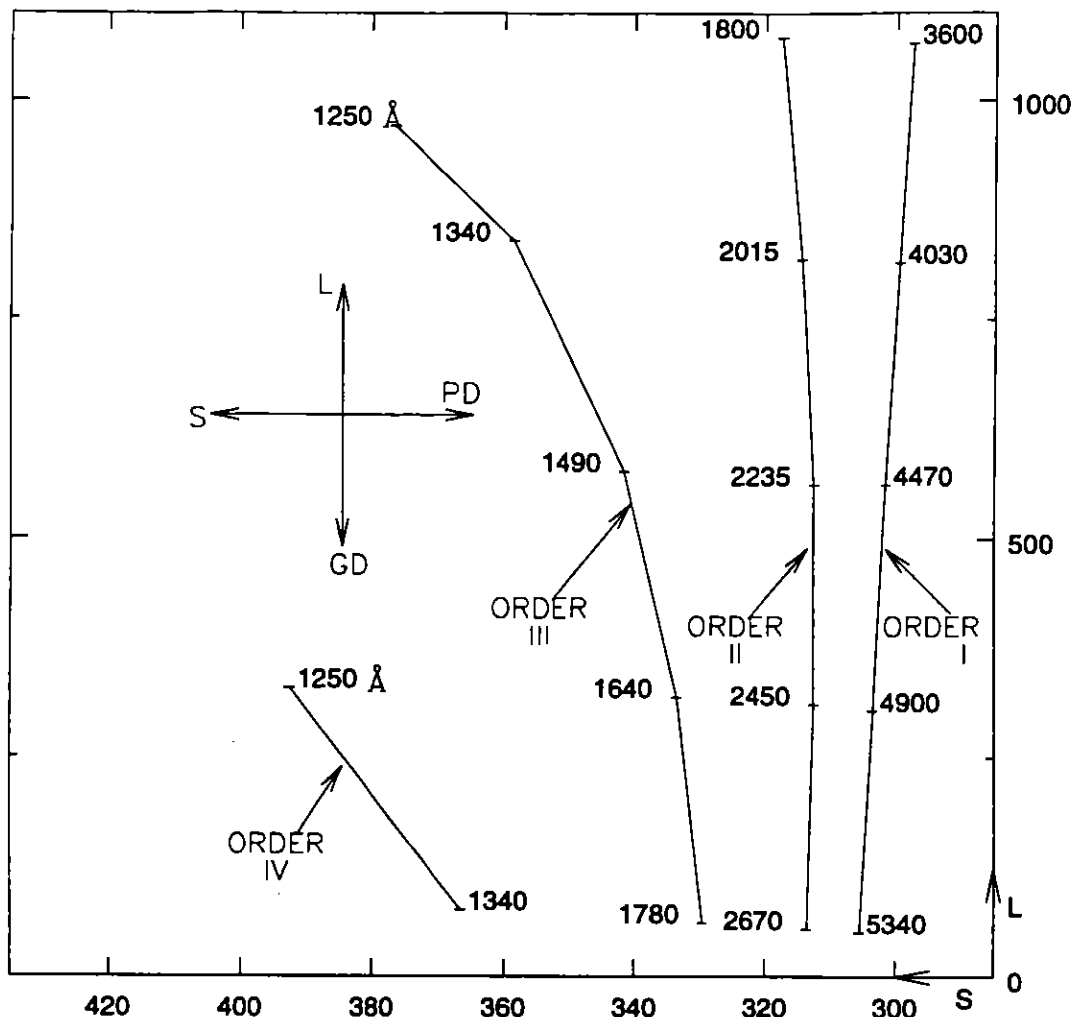
Figure 21. Optical layout of the F/48 focal plane in the spectrograph mode and the FOPCD in the beam. The coordinates are line numbers (L) as ordinates and sample numbers (S) as abscissas. Notice the different scales for S and L.

intensifier tube.

A lens assembly consisting of 9 components in a double Gaussian design is used to transfer the image from the output phosphor of the intensifier to the fiber-optic faceplate of the TV camera. It is designed to operate at f/2.7 with a slight magnification (1.15) to compensate for the demagnification of the image intensifier. The 80% energy width for point object images varies between 22 and 35 microns over the whole of the useful area and the light transmission is more than 60%.

4.6.2 TV Tube

The camera tube is a Westinghouse WX32719 low-light TV tube. This is a high-sensitivity, high resolution EBS tube (Santilli and Conger in *Photo-Electronic Devices*, AEEP, ed. L. Marton, 33A, 1972) with a 25 millimeters square diode array target, magnetic focus and deflection coils and an electrostatically focused image section with a 40 millimeter diameter useful photocathode
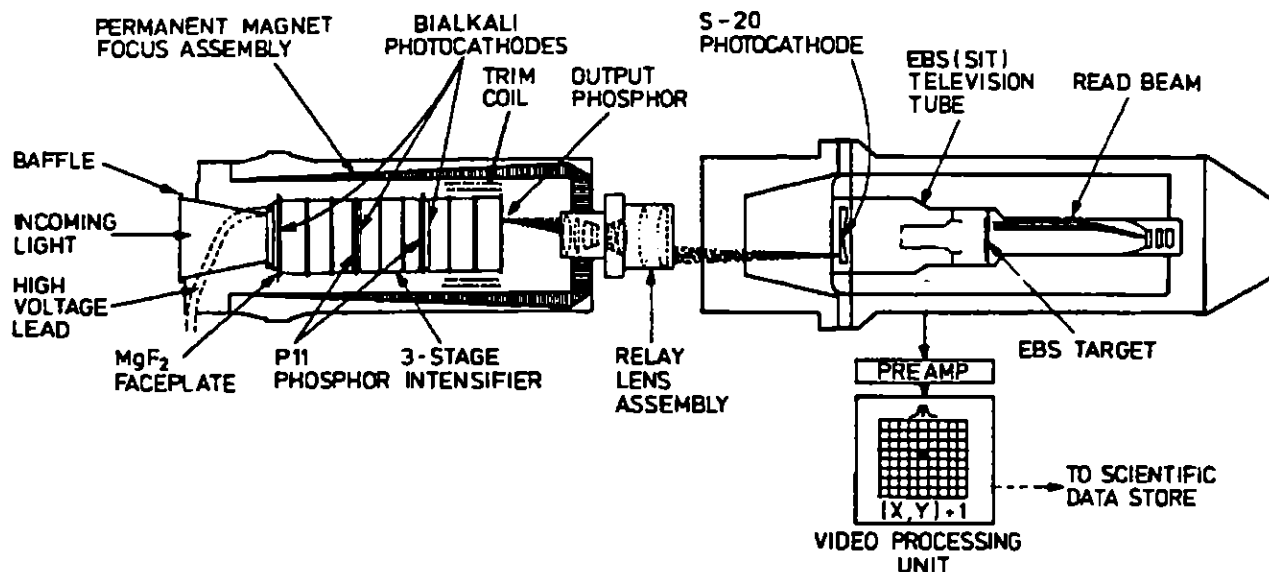
Figure 22. Physical Layout of the Imaging Photon Counting Detectors

area. The S-20 photocathode is evaporated onto the concave inner surface of the input fiber-optic faceplate. The emitted photoelectrons are accelerated by a potential of up to 12 kilovolts and focused onto the target which is an N-type silicon wafer with diffused P-type regions arranged in an hexagonally-packed diode array.

During operation each diode is reverse biased. Incoming photoelectrons generate electron-hole pairs which discharge the diodes. An amplified charge pattern corresponding to the image is then stored in the diodes. The charge flowing in the target lead, when the scanning beam recharges the diodes, is the signal current. The target gain is about 2500 and the modulation transfer function is 50% at 8 line-pairs per millimeter. The video signal coming from the TV tube is amplified by the preamplifier and then transmitted to the Video Processing Unit (VPU).

4.7 VIDEO PROCESSING UNIT

Each camera has its dedicated VPU which accepts the amplified signals from the camera preamplifier. The purpose of the VPU is to determine the x-y centroid of each event, determine if a true photon event has occurred and to increment the SDS memory address corresponding to the location where the photon event was detected. During any one scan of a frame of duration of 30 milliseconds for the 512 × 512 format down to 520 microseconds for the smallest 64 × 64 format there will only be a few scattered photon events. A photon event is typically a spot with a diameter of 3 or 4 pixels. It is read by the scanning beam on successive lines of the raster scan. Figure 23 illustrates how such a signal would look using the z axis to represent the magnitude of the charge.

As a line is scanned, a gaussian shaped pulse is produced. As successive lines are scanned, additional pulses, corresponding to slices of the event, increase in peak amplitude until a maximum is reached. The pulse amplitude then decreases. This video signal is amplified and presented to the VPU which takes the incoming video lines and produces two signals needed to analyze the waveform, Peak Signal and Extent Signal. The Peak Signal corresponds to the point of maximum amplitude of an event on a single scan line or slice. The Extent Signal is used to determine the time or extent of the event during a single line.

A true photon event is present on several successive lines. Analysis of these events character-ized by the peak and extent signals on successive lines is the task of the VPU. By using delay lines and shift registers, each event is examined in a 4×9 pixel area by real time analysis so that the same event on successive lines can be analyzed. The z-dimension event center is tagged in the x and y direction. The Pattern Recognition Logic analyzes the event's shape to determine true pho-ton events and reject other noise and ion events.
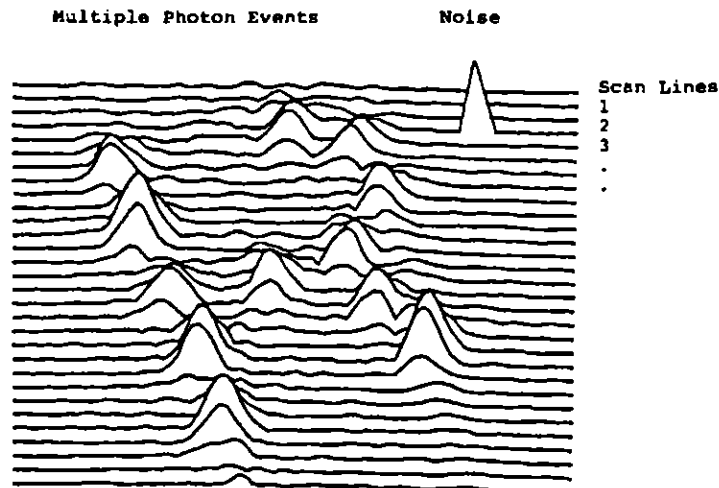
Figure 23. Schematic Drawing of a Typical Raster Scan Output of the Detectors

4.8 SCIENCE DATA STORE

As an event is detected and classified as valid, the video processing unit causes the science data store (SDS) to increment by one the memory location corresponding to the event centroid. The image is gradually built up over the exposure time. After stopping the exposure, the SDS can be read out without disturbing the stored image. The SDS can accept a 512×512 line image in the 16 bit word mode or a 512×1024 line image in the 8 bit word mode. The cycle time for the SDS is compatible with the camera scan rate of $\geq 10^6$ pixels per second. This rate is maintained for all formats and zoom. In this latter mode, the camera read beam scans the target twice as fast in the line direction as it does in the normal imaging mode but the pixels are twice as long. The detector generates an increment command for every pixel in which a photon event has been detected. A scan of 256K pixels occurs in less than 30 milliseconds while a scan of 4K pixels (i.e. a 64×64 pixel squared format) takes place in approximately 512 microseconds.

There are two different interface circuits in the SDS (SDS-1 and SDS-2), with unit 1 dedicated to the camera of the F/48 relay and unit 2 to the camera of the F/96 relay. The SDS memory is physically divided into 22 modules of 16K 16-bit data words each holding 32 words from each of 512 lines, but only 16 modules are active at any given time. These 16 modules are accessed in sequence to reduce the required memory cycle time. Each SDS word has 22 bits, with the extra 6 bits being used for "single-bit" error correction and "two-bit" error detection. Included in the engineering telemetry are error detection and correction bits set for each logical module. If more than 6 SDS memory modules fail, the memory can still be operated in a reduced data mode. In this case, zeros will appear in the downlink for those modules that are not available. Data loss occurs from the "right-hand" side, so if only 15 modules are up, words 0-479 for each of the PDA lines of 512 pixels would be obtained.

The SDS can be operated in either the normal imaging mode or the SDS dump mode so it is necessary to interrupt the pixel increment commands from the detector to read out the SDS memory to the downlink. Each readout is a dump of the 256K 16-bit words of SDS memory, and hence contains 4M data bits regardless of the image format. Readout of science data is normally done under control of the NSSC-1, which controls the gating of signals to the Remote Interface Unit (RIU) of the SI C&DH including the Science Data Formatter (SDF). From the SDF, the data is fed to the downlink or the tape recorder.

5.0 OBSERVING ARRANGEMENTS

5.1 IMAGING, OCCULTATION AND SPECTROGRAPHIC MODES

Operationally, the observation of an astronomical source with the FOC is defined once the following physical parameters are specified in terms of RPS2 Exposure parameters:

1. The optical relay or configuration (*Config*): FOC/96 or FOC/48
2. The choice of filters or spectral elements(*Sp_Element*) chosen from the 4 filter wheels of the F/96 or 2 filter wheels of the F/48 camera: See Tables 3 and 4.
3. The optical mode (*Opmode*) of the camera: ACQ, IMAGE, OCC, or SPEC [spectrograph mirror in the F/48 beam]
4. The S$\times$L imaging format (*Aperture*): S$\leq$512, L$\leq$1024 pixels with S the number of SDS pixels in the line scan direction and L the number of SDS pixels in the increasing line direction
5. The pixel size (*Optional Parameter: Pixel Size*): 25 $\times$ 25 microns squared (default) or 50 $\times$ 25 microns squared (for zoomed formats)
6. The position of the target in the chosen format (*Special_Requirement: POS TARG*).
7. The exposure time for the observation (*Time_per_Exposure*).

The F/48 camera will be made available again in Cycle 7, FOR LONG SLIT SPECTROSCOPY ONLY.

Selections 4 and 5 are subject to the 4 Mb SDS memory size limitation. This means that the word length is completely defined, once the format is selected, such that all formats larger than 512 $\times$ 512 pixels squared will automatically require an 8-bit word length while any format of that size or less will be imaged with 16-bit words.

Only a small fraction of all the possible observational modes allowed in principle by the FOC will find practical astronomical application and, therefore, be accurately and extensively understood and calibrated prior to use. Table 7 lists the main characteristics of the standard imaging and spectrographic observing modes are available for the F/96 and the F/48 relays. The first column in this table gives the format size (S$\times$L), the second the pixel size in microns and arcseconds squared in the sky, the third the starting pixel (S$_0$, L$_0$), the fourth the word length, the fifth the zoom configuration, the sixth the overall field of view in arcseconds squared for that format, the seventh the maximum count rate per pixel N$_{MAX}$ for that format (see Section 6.2.1), and the last column lists the main scientific justification for the selection, the mode names used in the Proposal Instructions for HST, if appropriate, and the proposal entry required for that format. S$_0$ is given in the 1$-$1024 range on a dezoomed extended format.

For the spectrographic modes of the F/48 relay, the pixel size and the FOV are given in units of arcseconds $\times$ Angstroms in first order. The pixel size (selection 5 in the list above) is considered an optional parameter in the Phase II Exposure Logsheet of the ST Proposal Forms. The default value, if none is specified, is 25 $\times$ 25 microns squared for imaging and 50 $\times$ 25 microns squared for spectroscopy. The position and orientation of the target in the aperture (selection 8) should be specified in the Special Requirements column of the Phase II Exposure Logsheets using the *POS TARG* and *ORIENT* commands.

Table 7a: F/96 IMAGE or OCC Modes

Format (S × L)	Pixel Size (μm^2) ($arcsec^2$)	Offset (S_0,L_0)	Word Length	Zoom	FOV ($arcsec^2$)	N_{MAX}[a] (cs^{-1})	Comments/ Proposal Entry
512 × 1024	50 × 25 (0.028 × 0.014)	0,0	8 bit	on	14 × 14	0.04	Largest FOV. Opmode: IMAGE or OCC. Aperture: 512 × 1024, PIXEL = 50 ×25
512 × 1024	25 × 25 (0.014 × 0.014)	256,0	" "	off	7 × 14	0.08	Largest FOV with highest resolution. Opmode: IMAGE, Aperture: 512 × 1024
512 × 512	50 × 25 (0.028 × 0.014)	0,256	16 bit	on	14 ×7	0.08	Largest FOV with highest photometric accuracy. Opmode: IMAGE. Aperture: 512 × 512, PIXEL = 50 × 25
512 × 512	25 × 25 (0.014 × 0.014)	256,256	" "	off	7 ×7	0.15	Highest photometric accuracy. Opmode: IMAGE, Aperture: 512 × 512
512 × 512	" "	0,512	" "	" "	" "	" "	Covers 0.4 coronographic finger. Opmode: OCC, Aperture: 512 × 512-F0.4
512 × 512	" "	421,0	" "	" "	" "	" "	Covers 0.8 coronographic finger. Opmode: OCC, Aperture: 512 × 512-F0.8
256 × 1024	" "	384,0	" "	" "	3.6 × 14	" "	Allows imaging of entire NUVOP spectrum. Opmode: IMAGE, Aperture: 256 × 1024
256 × 256	" "	384,384	" "	" "	3.6 × 3.6	0.6	Wider dynamic range, highest photometric accuracy. Opmode:IMAGE, Aperture: 256 × 256
128 × 128	" "	448,448	" "	" "	1.8 × 1.8	2.4	Widest dynamic range. Opmode:IMAGE, Aperture: 128 × 128

a. Maximum count rate to maintain <10% non-linearity for uniform illumination. Point sources may be observed at count rates in the peak of the core at about 12 times this level and still maintain <10% non-linearity (see Section 6.2.2).

Table 7b: F/48 Image Modes

Format (S × L)	Pixel Size (μm^2) (arcsec²)	Offset (S_0, L_0)	Word Length	Zoom	FOV (arcsec²)	N_{MAX} (cs⁻¹)	Comments/ Proposal Entry
512 × 1024	50 × 25 (0.056 × 0.028)	0,0	8 bit	On	28 × 28	0.03	Largest FOV. Available for ACQ only. Aperture: 512 × 1024, PIXEL = 50 × 25
512 × 512	25 × 25 (0.028 × 0.028)	0,384	16 bit	" "	14 × 14	0.10	Highest photometric accuracy. Available for ACQ ONLY. Aperture: 512 × 512

Table 7c: F/48 SPEC Modes

Format (S × L)	Pixel Size (μm^2) (arcsec × Å)	Offset (S_0, L_0)	Word Length	Zoom	FOV (arcsec × Å)	N_{MAX} (cs⁻¹)	Comments/ Proposal Entry
512 × 1024	50 × 25 (0.056 × 1.8)	0,0	8 bit	On	28 × 1800	0.04	Highest spectral resolution with widest spectral range. Aperture: 512 × 1024, PIXEL = 50 × 25
512 × 1024	25 × 25 (0.028 × 1.8)	192,0	8 bit	Off	14 × 1800	0.08	Highest spatial and spectral resolution with widest spectral range. Aperture: 512 × 1024, PIXEL = 25 × 25
256 × 1024	50 × 25 (0.056 × 1.8)	192,0	16 bit	On	14 × 1800	0.03	Widest dynamic and spectral range. Aperture: 256 × 1024-SLIT
256 × 1024	25 × 25 (0.028 × 1.8)	320,0	" "	Off	7 × 1800	0.10	Widest dynamic range,highest spatial resolution. Aperture: 256 × 1024-SLIT, PIXEL = 25 × 25

5.2 TARGET ACQUISITION MODES

Two acquisition modes are available for use with the FOC as described in the Proposal Instructions: INTeractive ACQuisition (Mode I) and blind pointing (Mode III). On-Board Acquisition (Mode II) is not available due to technical limitations. In addition, an EARLY ACQuisition can be specified where an examination of the field is necessary prior to science exposures to help measure a target in a crowded field or to determine a slit alignment angle, for example.

5.2.1 Mode I Target Acquisition - INTeractive ACQuisition

Designed to be the most accurate acquisition procedure for use with the small image formats or the slit, this procedure requires the involvement of the observer, in real-time, to identify the field and measure the center of the target on an FOC image. First, using a blind pointing acquisition, the target is placed in a standard field of view and an image is taken, with instrument parameters such as filters and exposure time selected by the user. The resulting image of the field is then read down for immediate display at STScI. Once the observer identifies the target using an interactive image display system and measures the target position from the display screen, a slew request is generated and up-linked, and the telescope is maneuvered to place the target in the selected destination. There is no verification of the subsequent field unless specifically requested by the observer in their Phase II proposal.

INTeractive ACQuisition is expected to be the standard acquisition procedure to acquire targets into formats smaller than the standard 512 x 512. The procedure also may be useful in IMAGE mode when an object needs to be placed in a particular place in one of the imaging apertures. For the long slit spectrograph, which has a slit width of only 0.06 arcseconds, INTeractive ACQuisition is the only allowed way to ensure proper centering of a point source.

In terms of overheads, an INTeractive ACQuisition adds 16m for Decision Time (time to receive the image and calculate the slew), and 8.5m to uplink the slew prior to obtaining the next science exposure (in RPS2 the overheads will be shown immediately following the exposure with the INTeractive ACQuisition, but during execution the precise scheduling of these activities will depend on availability of the TDRS communications with the HST).

In IMAGE mode, objects of 9th magnitude or brighter require an INTeractive ACQuisition and an additional filter check to ensure the safety of the detector. Whenever an acquisition is required of a target brighter than the 9th magnitude, the user has to specify the Special Requirement: CHECK-FILTER = YES. This will allow an automatic procedure to be activated, which checks whether the proper filter configuration is in place. If, and only if, the proper filter configuration is in place, the FOC will take the ACQuisition exposure. Otherwise, the automatic procedure will safe the instrument. This procedure must be repeated whenever a different filter configuration is selected. No overhead is required by this special requirement CHECK-FILTER.

5.2.2 Mode III Target Acquisition - Blind Pointing

Mode III is the default acquisition procedure for the FOC. When no target acquisition is specified in the Special Requirements section on the proposal exposure logsheets, the telescope performs a straightforward blind pointing on the coordinates provided by the user. After the acquisition, no explicit verification of the target position in the fields-of view-aperture-is-performed. No overhead time in addition to the guide stars lock time is charged to the user for this

acquisition.

Mode III is expected to be the standard acquisition procedure for IMAGE mode in all instrument configurations, except for those formats smaller than the F/96 512 x 512. The user must ensure that the target's coordinates have been measured within the Guide Star Selection System (GSSS) ensuring best accuracy with respect to the guide star catalogue. The procedure will not be useful for point sources in SPEC mode, because blind pointing is unlikely to provide the precision needed to accurately place a target on the slit of the F/48 relay (width = 0.06 arcseconds). However, for extended objects where accurate pointing is not important, blind pointing can be used. Targets of magnitude 9 and brighter can be acquired with blind pointing by using the Special Requirement Check-filter = yes (see Section 5.2.1) and a filter combination which will bring the expected count rate down to allowed levels.

5.2.3 EARLY ACQuisition

When necessary, it is possible to take an acquisition image some time before the scientific observation. The acquisition image can be used for a better identification of the field, or a better evaluation of the source flux, etc. In order to update the observation parameters, a minimum turnaround time of two months is necessary between the acquisition and the science exposure.

Presently, the system does not have the capability to select for the science observation the same pair of guide stars successfully used for the acquisition exposure, thus eliminating the possibility of using the acquisition image to measure the target coordinates at the accuracy level required to perform, for example, a blind pointing on the F/48 0.06 arcseconds slit.

Table 8: Target Acquisition Formats

Relay	Format Name	Size	USE
F/48	512z × 1024	1024 × 1024	spectrograph slit
F/48	512 × 512	512 × 512	spectrograph slit
F/96	512z × 1024	1024 × 1024	
F/96	512 × 512	512 × 512	

5.3 THE FOC TARGET ACQUISITION APERTURES

For convenience, a number of special formats to be used in the Mode I acquisition exposures have been defined. These formats (listed in Table 8) are calibrated and maintained in order to ensure good pointing accuracy (better than 0.2"). This applies currently to the F/96, however, the F/48 pointing accuracy has not been established yet.

Different sizes are available, but it is strongly recommended to use the larger images for acquisition purposes, due to the initial position error of the target's coordinates with respect to the guide stars ($\cong$ 0.33 arcseconds).

6.0 INSTRUMENT PERFORMANCE

6.1 THE POINT SPREAD FUNCTION (PSF)

Before the installation of COSTAR, the HST+FOC PSF suffered from severe spherical aberration, which meant that a circular aperture of 0.1 arcsecond radius contained only 15-18% of the light from a star instead of the expected 70%. The principal effect of the spherical aberration was a loss in sensitivity, because most of the light in the halo of a faint star is effectively lost in the background noise. COSTAR has restored much of the OTA capability, in that the COSTAR-corrected PSF contains more than 75% of the light within a radius of 0.1 arcsecond at visible wavelengths while losing less than 20% of the light to the two reflections at the two extra mirror surfaces. The net increase in sensitivity is a factor of approximately 3-4 at visible wavelengths. The correction COSTAR made to the PSF is illustrated in Figure 24, which shows the radial profile of an aberrated PSF image and a COSTAR-corrected image.

Image Profile — Before & After
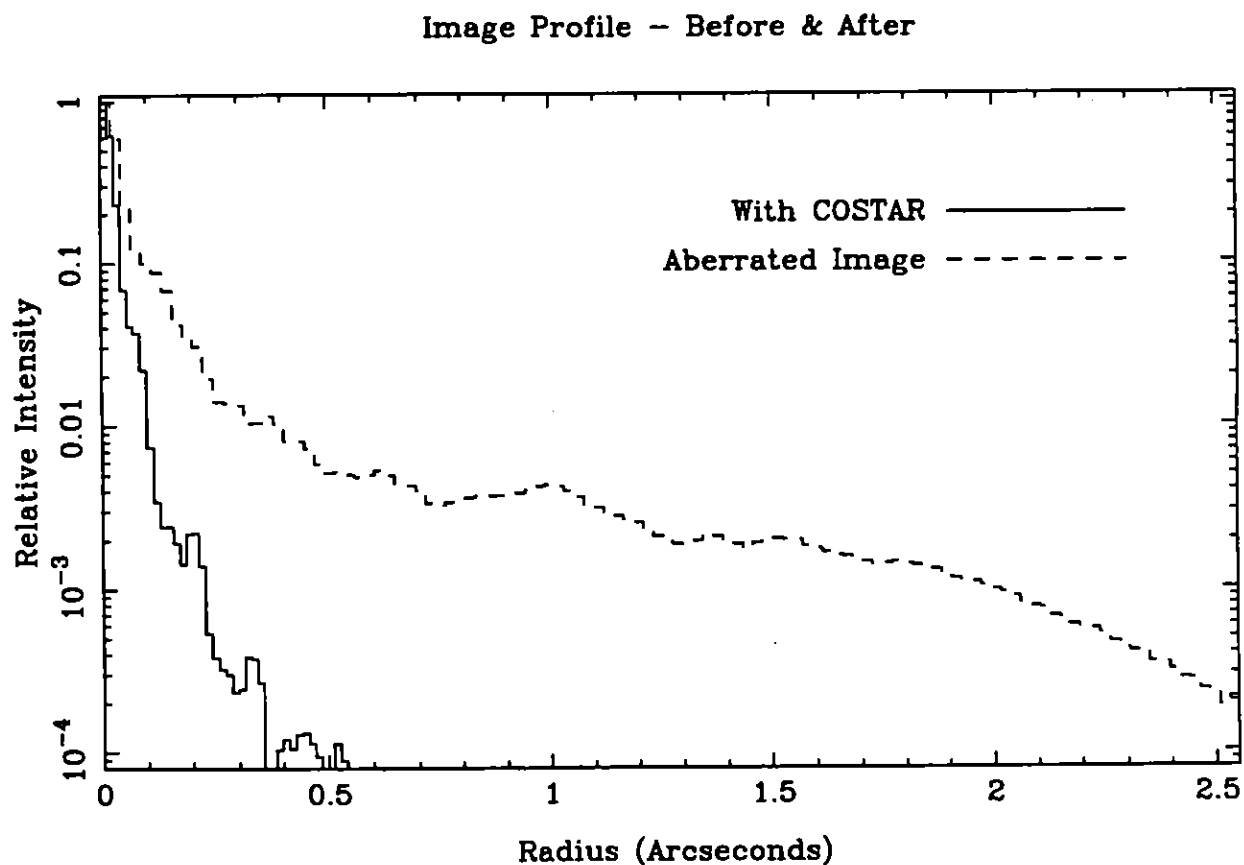
Figure 24. Radial profiles of pre-COSTAR aberrated PSF (**dotted**) and COSTAR-corrected PSF (**solid**) at 4860Å.

In Table 9, the encircled energy fraction $\varepsilon(\lambda)$ is tabulated for various circular apertures against the number of pixels in the aperture and the effective radius (defined as $\sqrt{\#pixels/\pi}$, with the definition that the encircled energy is 1.0 at a radius of 1 arcsecond (70 pixels)). A more thorough discussion of the definition of the encircled energy calculation and the rationale behind it is given in the Detective Quantum Efficiency section, 6.3. These energy fractions are to be used to predict

Table 9: Measured Energy Fraction ε(λ) for the F/96 Relay

n	r (arcseconds)	F120M	F140M	F170M	F210M	F278M	F346M	F410M	F486N	F550M
1	0.007	0.039	0.061	0.055	0.094	0.093	0.087	0.071	0.064	0.054
9	0.024	0.214	0.294	0.319	0.415	0.452	0.409	0.385	0.380	0.345
21	0.037	0.315	0.421	0.463	0.555	0.621	0.528	0.543	0.548	0.532
37	· 0.049	0.393	0.499	0.558	0.626	0.712	0.601	0.627	0.613	0.611
69	0.067	0.491	0.577	0.652	0.688	0.774	0.722	0.744	0.697	0.670
97	0.080	0.536	0.619	0.696	0.722	0.802	0.773	0.799	0.769	0.727
137	0.095	0.578	0.657	0.739	0.768	0.832	0.809	0.830	0.831	0.807
177	0.108	0.599	0.682	0.763	0.798	0.858	0.833	0.844	0.855	0.851
225	0.121	0.626	0.703	0.781	0.821	0.886	0.856	0.858	0.870	0.870
293	0.139	0.653	0.724	0.798	0.841	0.909	0.877	0.877	0.886	0.881
349	0.151	0.664	0.736	0.808	0.851	0.919	0.896	0.888	0.897	0.888
421	0.166	0.682	0.749	0.819	0.859	0.928	0.916	0.905	0.909	0.898
489	0.179	0.696	0.762	0.829	0.867	0.934	0.927	0.922	0.917	0.906
577	0.194	0.712	0.777	0.841	0.873	0.942	0.938	0.934	0.928	0.915
665	0.209	0.723	0.790	0.850	0.877	0.948	0.944	0.941	0.941	0.921
749	0.222	0.734	0.799	0.855	0.883	0.951	0.948	0.945	0.950	0.929
861	0.238	0.747	0.810	0.863	0.889	0.954	0.952	0.950	0.955	0.942
973	0.253	0.750	0.821	0.871	0.896	0.958	0.956	0.953	0.958	0.949
1085	0.260	0.765	0.830	0.879	0.902	0.961	0.958	0.957	0.961	0.952
1201	0.281	0.774	0.839	0.886	0.909	0.964	0.959	0.961	0.964	0.955
1313	0.293	0.790	0.847	0.892	0.913	0.967	0.961	0.964	0.966	0.958
1457	0.309	0.803	0.856	0.900	0.917	0.970	0.964	0.967	0.969	0.961
1597	0.324	0.813	0.865	0.907	0.923	0.972	0.966	0.970	0.972	0.963
1741	0.338	0.822	0.875	0.914	0.929	0.974	0.968	0.973	0.975	0.964

how many counts one can expect to measure given the total count rate from FOCSIM or SYN-PHOT, or from using the formulation in Chapter 7. For the most part, these numbers are believed to be good to approximately 10% or so, but they are subject to variation due to the changes in the effective focus of the OTA ('breathing'). This typically causes the fraction of the energy in small apertures (with radius 3 pixels or so) to vary by ~10%, but with worst case variations of up to 50%, and is most severe in the 2000-4000 Å range. Taking PSF observations just before or after one's science data will not help to improve the measurement of encircled energy, since the variation is orbital in nature.

The improvement in performance over the aberrated PSF is shown in Figure 25, where the encircled energy curve is compared to that of the aberrated OTA and with a perfect diffraction-limited image from a 2.4m circular aperture with a 0.33 central obstruction. It can be seen that the COSTAR-corrected FOC PSF approaches that of an ideal imaging system in both encircled energy performance and in the FWHM of the PSF core.

The profile of the PSF itself is not characterized to very high accuracy, since this would require long integrations at many different wavelengths. The signal-to-noise ratio of PSF images

COSTAR/FOC – Comparison with Perfect Image
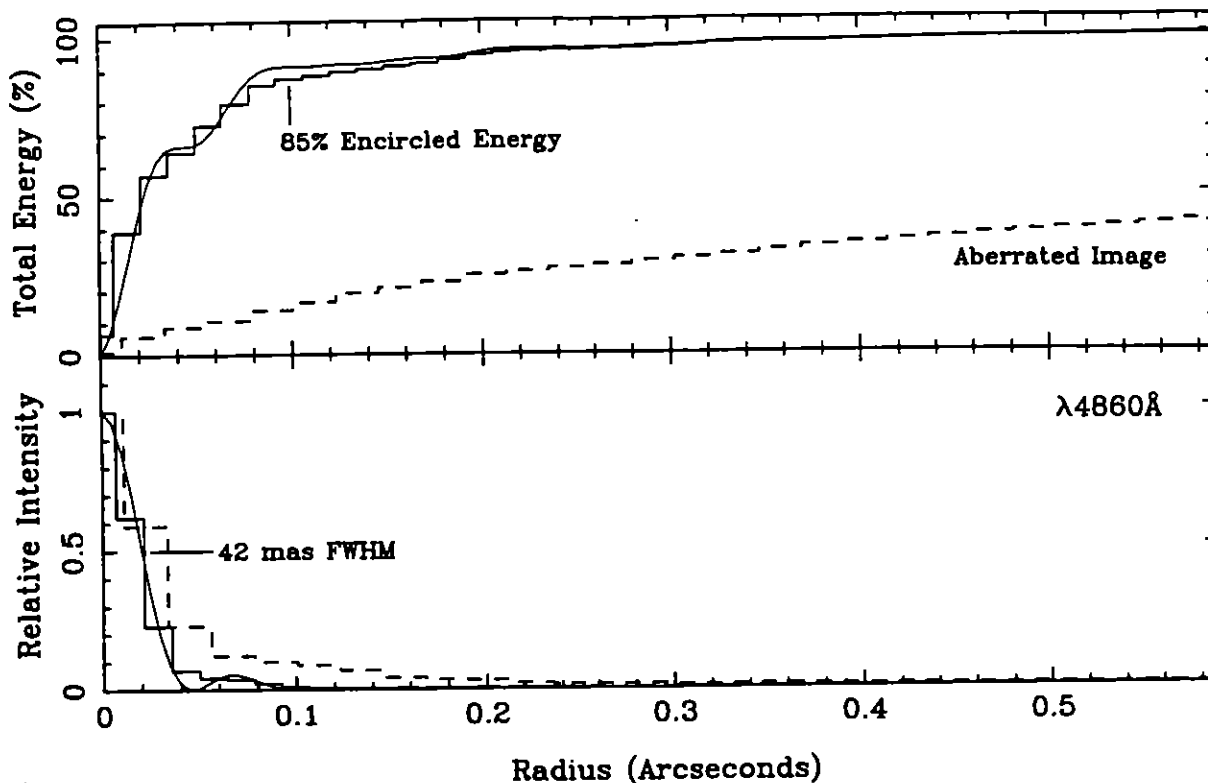
Figure 25. The encircled energy fraction and PSF profile for the COSTAR-corrected F/96 and pre-COSTAR F/96 relays compared to those expected from a perfect diffraction limited OTA.

taken for the DQE measurement program typically allows measurement of the PSF profile to 25-50% accuracy when azimuthally averaged over a 1-pixel wide annulus. Variations of the profile will occur in the core as a result of OTA orbital variations, but outside 0.15 arcsec radius the PSF profile is dominated by scattering from small-scale irregularities in the OTA & COSTAR mirrors and FOC optics. It is recommended that if observers need accurate characterization of the PSF for their data (for example, if they are trying to detect low-surface brightness features in the vicinity of bright point-like sources), then they should explicitly ask for such calibration time in their proposal. Again, it is stressed that characterization of the PSF interior to 0.1 arcsec is not possible, because of its dependence on orbital variations in the focus.

The resolution provided by the HST+FOC combination is characterized in a simplistic way by specification of the FWHM of the PSF as a function of wavelength. This was measured for a sample of PSF observations using the raw (.d0h) images, so that there would be no degradation by the geometrical correction resampling process. The FWHM was measured in both the X and Y directions by simply interpolating where in the 1-dimensional profiles the intensity dropped to half of the peak value; no attempt was made to account for undersampling. The mean of X and Y FWHM is plotted as a function of wavelength in Figure 26. It can be seen that the FWHM is less than 0.05 arcsec at all wavelengths, dropping to only 0.03 arcsec (2 pixels) below 3000Å. Users should note for comparison that one PC pixel is 0.045 arcsec, and that the PC PSF typically mea-
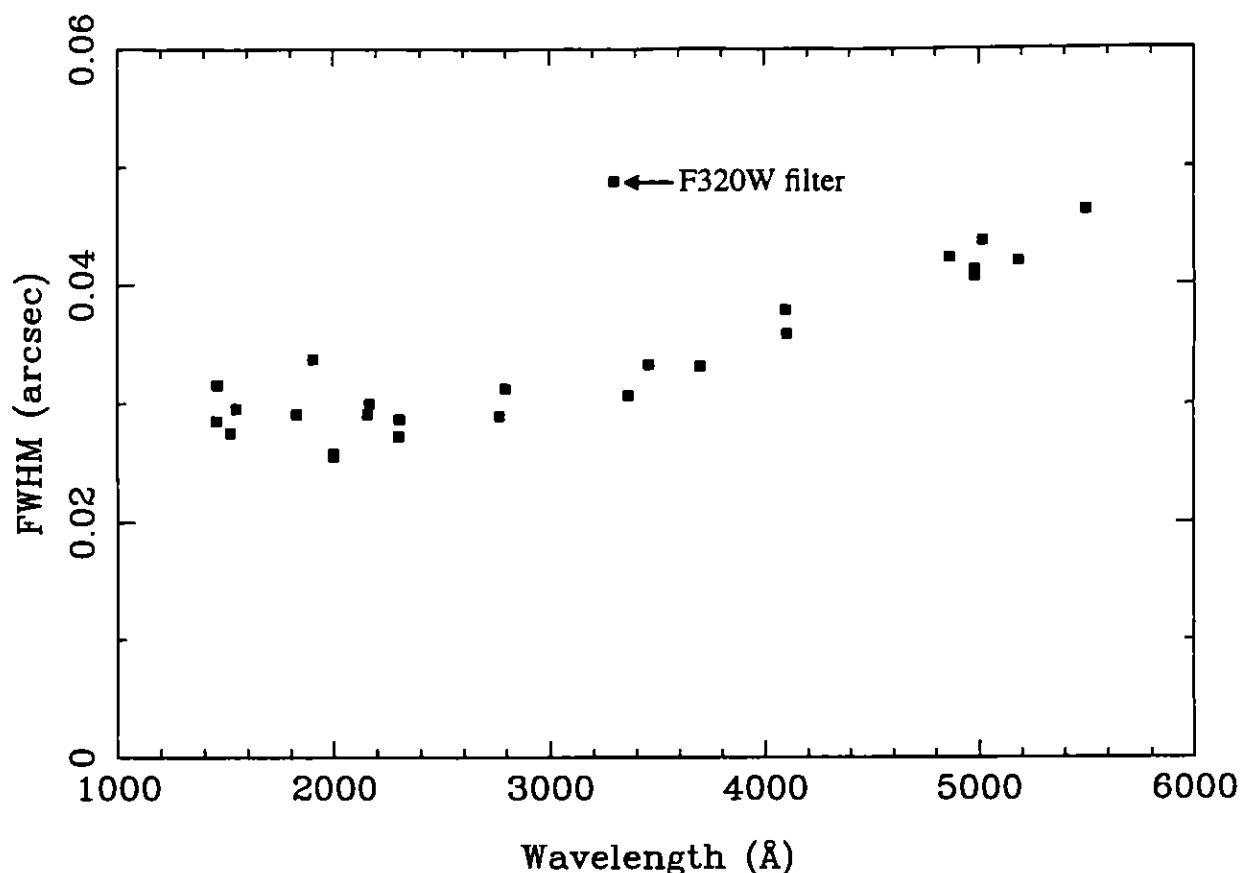
Figure 26. Variation of FWHM with wavelength for the F/96 relay of the FOC

sures **1.6-1.8 pixels (~0.08 arcsec)**. Compared to STIS, the FOC has better sampling, given the pixel size of 0.05" for the STIS CCDs and of 0.025" for the STIS MAMAs.

The discrepant point in Figure 26 comes from the PSF using the F320W filter, which is significantly degraded in resolution to a FWHM of 0.09 by 0.035 arcsec.

Despite the outstanding performance of the OTA+COSTAR+FOC imaging system in terms of encircled energy within small radii, the PSF appearance does not quite match a true diffraction-limited simulation perfectly at all wavelengths. The PSF obtained using the F486N filter shows a non-uniform azimuthal intensity distribution in the first diffraction ring (Figure 27a). There is also a small amount of residual coma that possibly varies with time, possibly due to some slack in the M1 tilt mechanism. This was removed for the most part by a small tilt of the COSTAR M1 mirror in early August 1995.

In the ultraviolet, the PSF shows a fairly strong jet-like feature pointing approximately in the -V3 direction (Figure 27b). The strength decreases with increasing wavelength but is still quite noticeable at 4000Å. The cause of this feature and the asymmetry in the first diffraction ring is unknown.

Several filters have been found to have artifacts. The F372M filter shows a strong linear feature in the PSF wings, at approximately 45° to the OTA spider (Figure 27c). The F501N and F502M filters both show a faint ghost image 60 and 24 pixels respectively from the PSF center, approximately 5 magnitudes fainter than the core. The PSF taken through the F320W filter is significantly degraded, having a FWHM of approximately 6x2.5 pixels (compared to 2.5x2.5 pixels

for the F342W PSF, see also Figure 26). This causes the central pixel to contain only 3.5% of the total light in the PSF, compared to 10% for the F342W filter.

A selection of PSF images is available through the FOC WWW pages. The PSF images, and other FOC information is accessible via anonymous FTP, gopher, or WWW's Mosaic interface at *stsci.edu* (see Chapter 9 for more details).

a.   **b.**   **c.**
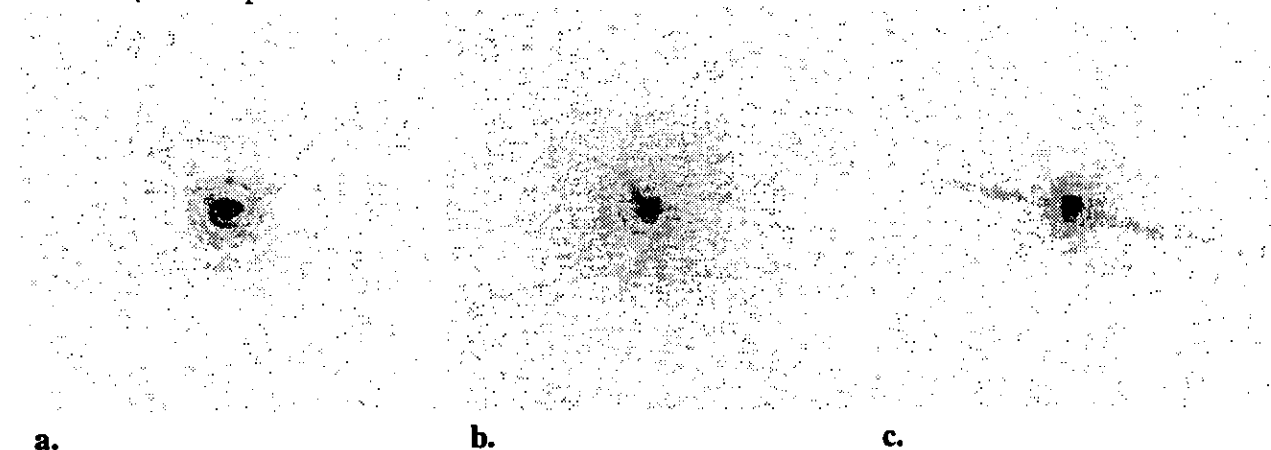
Figure 27. Images of PSFs taken with the COSTAR-corrected F/96 camera. **a.** F486N filter **b.** F120M filter **c.** F372M filter.

6.1.1 Image quality and Field Dependence of the PSF

The FOC was designed to image the HST focal plane in an off-axis position, 6.56 arcminutes from the optical axis. At this distance, the focal plane is tilted with respect to the V1 axis by 10°. It is this plane that the FOC cameras image onto their photocathodes. However, the focal surface produced by COSTAR is tilted with respect to the plane that the FOC images. This results in a field-dependent focus variation of approximately 0.7mm over the full field of the F/96 relay. Similarly, the tangential and sagittal focal surfaces are tilted with respect to each other, and this introduces field-dependent astigmatism. Both of these effects increase linearly with distance from the fully-corrected field point.

The field-dependence of the PSF was investigated during SMOV, but the limited observations do not allow detailed characterization of the performance as a function of field position. It is clear from calibration observations that the PSF is visibly different away from the central field point across the largest formats. However, this does not affect the encircled energy within 0.1 arcsec radius by more than a few percent for any field position within the 512X512 aperture.

6.2 DYNAMIC RANGE

If two or more photon events overlap during a given frame, the VPU detection logic will only count one detected photon. This 'undercounting', or non-linearity, sets a hard limit on the maximum allowable photon rate for the FOC. This limit depends on the frame scan time, which is proportional to the area in pixels of the selected format. Users can improve the linearity performance by choosing a smaller imaging format (but at the cost of field of view).

The linearity performance also depends on the image structure. If the illumination is nearly uniform, then the non-linearity depends on the frame scan time and the photon event size (typi-

cally 3 × 3 pixels). However, if the illumination comes from a perfect point source, then the photon event size does not matter, since there are no neighboring photon events, only those that arrive in the illuminated pixel. For FOC images, no source is truly pointlike, but the linearity characteristics of astronomical point sources and flat fields are sufficiently different that they are discussed separately. The situation for more complex image structure (*i.e.* just resolved or linear) will of course be intermediate between these two limiting cases.

6.2.1 Uniform Illumination

Here 'uniform illumination' refers to the case where the intensity varies by less than 20% over scales of 20 pixels. The frame scan time is given by

$$T_f = \frac{z(S \times L)}{8.8 \times 10^6} \sec$$

where $z = 1$ for normal and $z = 2$ for zoomed pixels. For the most widely-used format (512 × 512, normal pixels), this comes to 30 milliseconds. If, during a frame, more than half of the format area is occupied by photon events, a further event will overlap one or more existing events and will not be counted as a detected photon. This would predict a maximum count rate for the 512 × 512 format of 0.05 counts/pixel in 30 milliseconds, or about 1.7 counts/sec/pixel. In practice the saturation level is reached at a lower level, because most of the overlapping events are much larger than a single photon event and are classified as ion events and rejected.

Table 10: Calculated Flat-Field Linearity Parameters

Camera	Format (FxL)	Linearity Parameter a	N_{MAX} (cs^{-1})
F/96	512z×1024	0.11	0.04
	512×1024	0.37	0.08
	512×512	0.73	0.15
	256×256	2.93	0.60
	128×128	11.7	2.40
F/48	512z×1024	0.065	0.03
	512×1024	0.26	0.05
	512×512	0.52	0.10
	256×256	2.09	0.40
	128×128	8.37	1.60
F/48 SPEC	256z×1024	0.13	0.03
	256×1024	0.52	0.10

The flatfield nonlinearity was measured on-orbit during OV and SV using observations of the

internal LED calibration lamps. It was found that the intensity of the light from these lamps is directly proportional to the commanded intensity level. The linearity curve was measured for several different formats to verify the format dependence of the saturation, and the dependence on zoom mode was also investigated. A plot of the measured linearity relation for the 512×512 formats of the pre-COSTAR F/96 and pre-COSTAR F/48 detectors is shown in Figures 28*a* and 28*b*, respectively. Superposed is a curve that describes the behavior of the linearity relation for intensity values up to approximately 80% of the saturation value, originally suggested by Jenkins (*M.N.R.A.S.*, 226, 341 (1987)):

$$r = a(1 - e^{(-\rho/a)})$$

where r is the measured count rate, ρ is the 'true' count rate and a is a fitting parameter that is identified as the asymptotic measured count rate.

When the FOC is configured for zoomed pixels, the linearity performance is slightly different from what would be expected from scaling the results for normal pixels by the ratio of frame scan times. This is because the event sizes and the VPU detector logic are different for zoomed pixels. However, once the linearity performance of one format is calibrated for each camera in zoom mode, the performance at other formats in zoom mode can be derived by scaling by the ratio of format areas, as is the case for normal pixels. The validity of the scaling assumption for both normal and zoomed pixels was checked and found to be true.

Values of a for the most commonly-used formats are given in Table 10. The values refer to dezoomed data in the case of formats that were originally zoomed. In practice, the value of a depends somewhat on position in the image, since it is effectively a measure of the photon event size, and this varies over the format due to slight focus quality variations. To ensure that non-linearity does not compromise the science data, users are advised to ensure that the count rate is kept below N_{MAX}, which is the count rate that would give 10% nonlinearity, as given in the third column of Table 10. Correct and quantifiable operation of the FOC at count rates exceeding N_{MAX} cannot be guaranteed.

6.2.2 Non-Uniform Illumination

When the illumination comes from a star, the FOC is able to count at a much higher rate before saturation occurs. This is because photon events centered on pixels close to the central pixel of a star are much less probable than in the flatfield case.

During OV and SV-it became clear that for the FOC pre-COSTAR F/96 camera when used in the 512×512 format, the maximum obtainable count rate in the core of a star was approximately 3 counts/second/pixel. Variations on this level occur because of jitter, focus, etc. At count levels higher than this, the core of the star turns into a dark 'hole', and a bright crescent appears to one side of the core. Comparison of PSF's taken with and without neutral density filters indicate that there is no noticeable deviation from linear behavior for core count rates up to 1 count/sec in the brightest pixel. This produces the simple guideline for observers: **keep the count rate in the central pixel below 1 count/sec**, and then any photometry method chosen will give results that are not biased by non-linearity effects. If the central count rate is above 1 count/sec, one will need to use other methods to determine the brightness of the star (such as measuring the intensity in the bright halo).

An example of the non-linearity relation for point sources is shown in Figure 29. The data
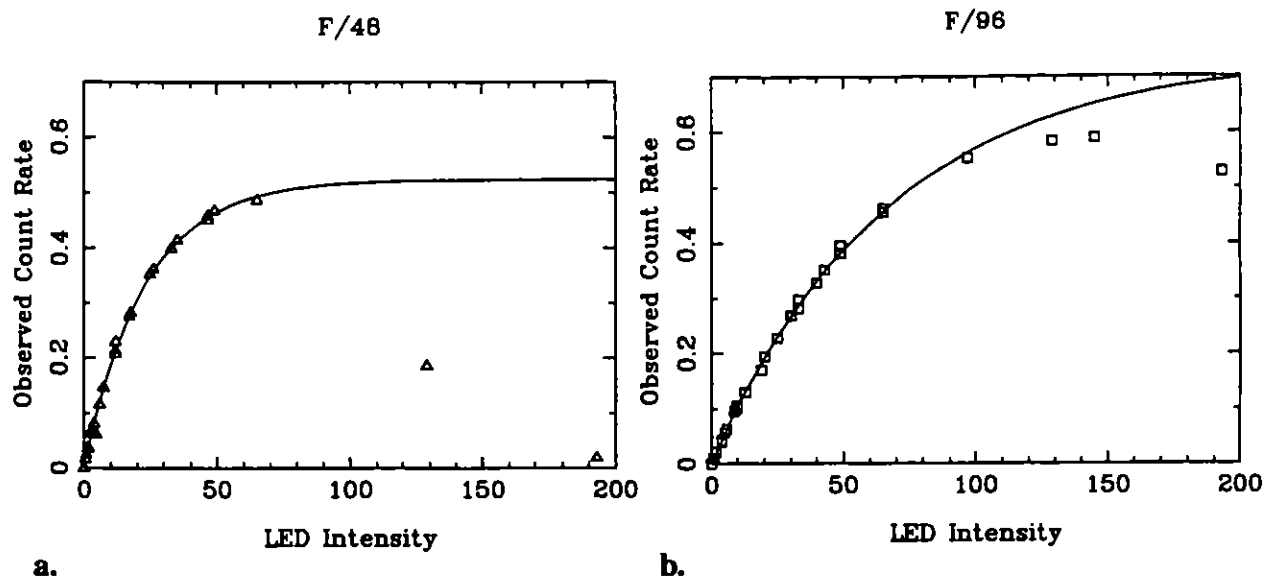
Figure 28. Flat-field linearity plots for the detectors in the pre-COSTAR F/48 and pre-COSTAR F/96 relays, **a** and **b** respectively, based on 512 × 512 pixel flat-field images of the internal LEDs at different intensities. The solid line in each plot is the best-fit solution for the linearity function given in the text.
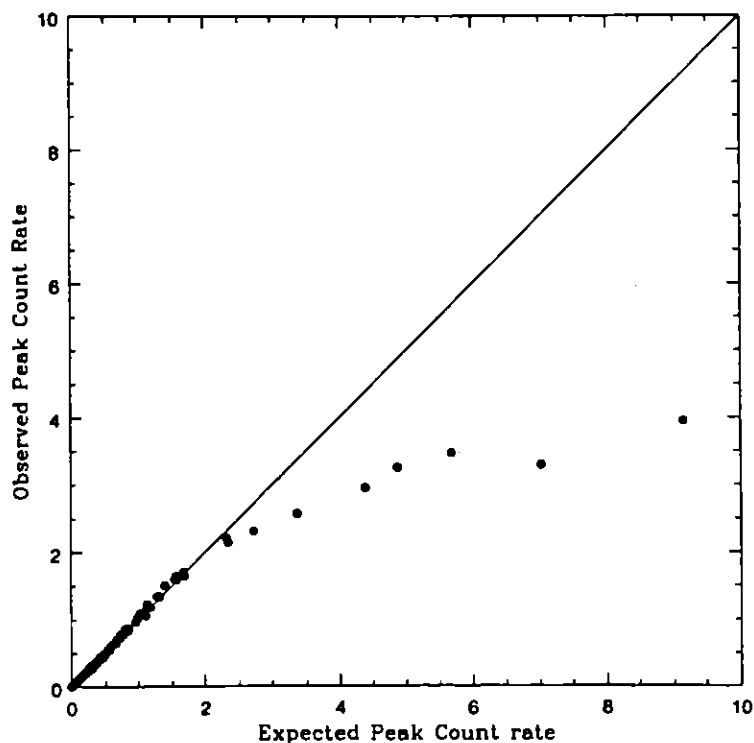
Figure 29. Linearity relation for point sources within a 5-pixel radius aperture, based on 512 × 512 pixel images taken with the post-COSTAR F/96 relay through the F430W filter.

used to construct this figure was drawn from FOC post-COSTAR F/96 512 × 512 images of the center of the globular cluster ω Cen taken through the F430W filter and combinations of ND filters ranging from F1ND to F6ND+F1ND. Observed count rates for each stellar image, measured inside a 5-pixel radius aperture, are expressed in terms of the corresponding peak count rate, assuming a normal F430W point-spread function. The expected peak count rates for each stellar image were determined by measuring the stellar flux through the most opaque ND filter combination in which the star is well-exposed, then extrapolating to more transparent filters based on the ND filter calibrations in Section 4.4.1. Above peak count rates of 2 counts/pixel/sec, the observed peak count rate falls noticeably below expectations, indicating the onset of non-linearity.

To put some hard numbers around these figures, note that a 20th magnitude AOV star will give a total count rate with the F342W filter of 10.9 counts/sec. Referring to Table 9, one can see that for the F/96 relay, the central pixel contains ~8.7% of the total light, therefore the expected count rate for this star is 0.95 counts/sec in the central pixel, which is at the FOC linearity limit. To observe stars brighter than 20th magnitude, it is necessary to either use a smaller format, neutral density filters or a narrower filter (*e.g.* F346M).

Attempts to deal with non-linearity corrections for pre-COSTAR FOC data are presented in FOC Instrument Science Reports FOC-073 and FOC-074, which are available from STScI or can be browsed from the FOC WWW pages.

6.3 ABSOLUTE QUANTUM EFFICIENCY

Spectrophotometric standard stars were observed during SMOV and Cycle 4 Calibration using a variety of filters to allow measurement of both the PSF characteristics and the detector quantum efficiency. These measurements were made after the COSTAR mirror tilts and DOB focus were set to optimize the imaging performance at 4860 Å wavelength for the F/96 camera. **Since the characterization of the F/48 camera is still in progress,** this section refers to the F/96 camera only.

The encircled energy and detector quantum efficiency are somewhat coupled since the PSF does not have a well-defined edge; instead the flux drops steadily with distance from the star center until it gets lost in the background noise. The flux in the wings is due to scattering by dust and small imperfections in the OTA+COSTAR+FOC optical train, and is more pronounced at shorter wavelengths. When constructing an encircled energy curve, which is the curve of the fraction of light enclosed within a circular aperture of a given radius as a function of radius, one naturally has to define how one measures the total flux. In the past, this was done by choosing an aperture size that was large enough to include the spherically aberrated PSF, or about 3.5 arcseconds radius. This aperture size could comfortably fit inside the workhorse 512X512 imaging format before COSTAR was installed.

Table 11: Overall (OTA+FOC+COSTAR) Absolute Quantum Efficiency Q(λ) in 10^{-3} counts photon^{-1}

| λ(Å)	Q(F/48)	Q(F/96)	Q(SPI)	Q(SPII)	Q(SPIII)	Q(SPIV)
1150	1.45	1.00				0.20
1160	4.04	1.39				0.32
1170	6.52	2.30				0.40
1180	9.28	3.39				0.47
1190	11.47	4.62				0.61
1200	13.14	5.88			0.46	0.70
1250	19.95	9.11			0.63	0.95
1300	22.74	10.93			0.70	1.08
1400	22.68	12.37			0.88	1.26
1500	22.30	13.47			1.05	
1600	20.13	12.92			1.15	
1700	18.72	12.32			1.34	
1800	17.84	11.72		2.04	1.55	
1900	20.26	13.12		2.69		
2000	26.41	16.86		3.32		
2200	40.80	26.20		4.60		
2400	51.59	35.44		5.33		
2600	53.59	43.06		5.55		
2800	55.43	51.36		5.47		
3000	55.87	60.66				
3400	56.62	67.65	10.48			
3800	51.70	67.73	10.64			
4000	47.28	61.51	10.58			
4500	35.45	38.66	10.24			
5000	21.27	22.06	8.45			
5500	8.97	10.88	4.84			
6000	3.95	4.90				
6500	0.38	0.46				
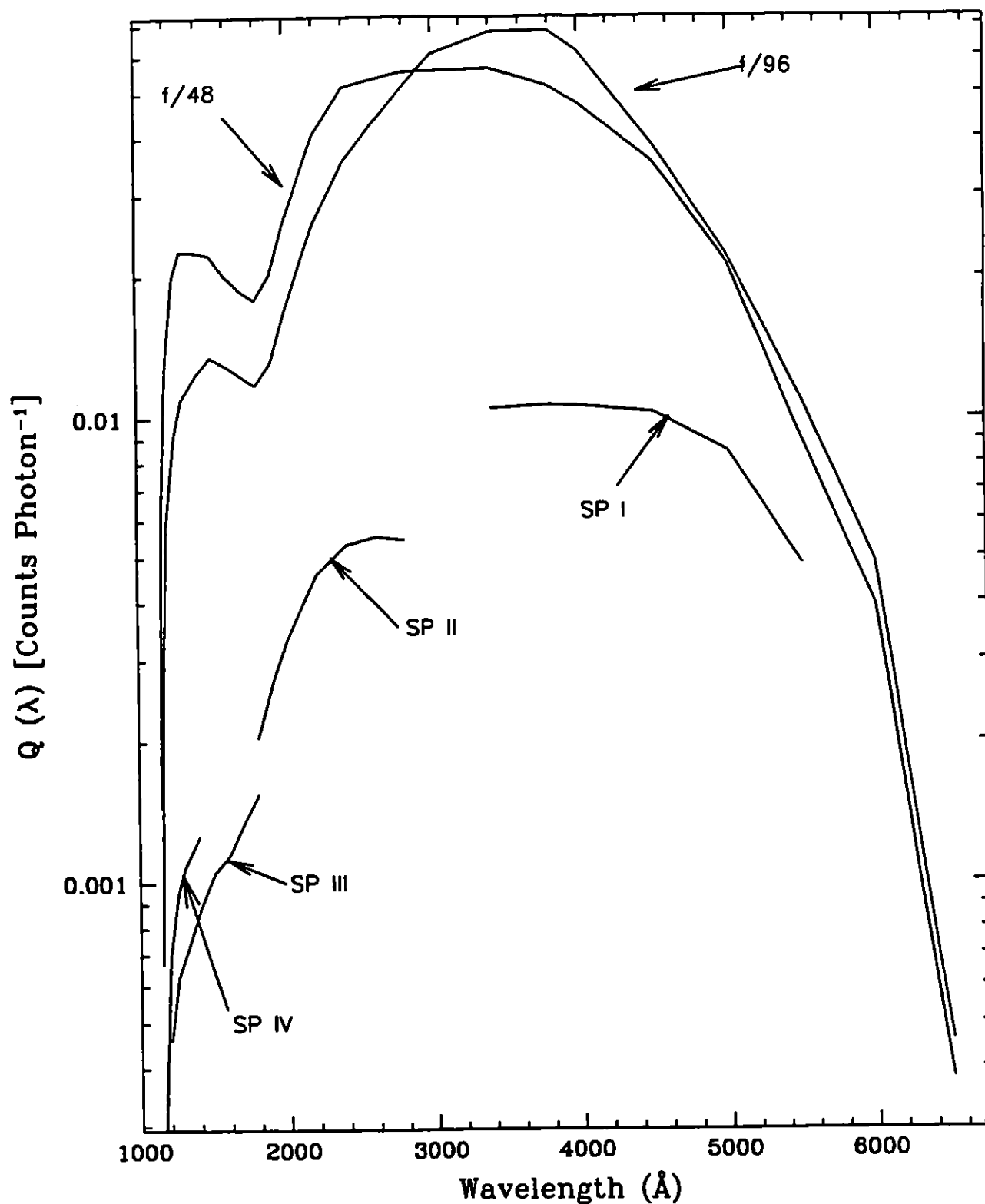
Figure 30. Baseline overall (OTA + COSTAR + FOC) absolute quantum efficiency in counts photon^{-1} as a function of wavelength for the three imaging modes and the four long slit spectrograph orders, including the obscuration of the OTA.

With COSTAR, the magnified plate scale means that such a large aperture size cannot be used for DQE measurements, particularly since most of the measurements of spectrophotometric standards were made using the 256X256 imaging format to improve the linearity performance. For this reason, it was decided to **define** the encircled energy to be 1.0 at a radius of 1.0 arcsecond (70 pixels) and to **define** the background as that value which minimizes the scatter of the points in the encircled energy curve with 0.9" < r < 1.1". In practice, this is equivalent to setting the background to the value measured at approximately 1.0" radius, and it does give encircled energy curves that are qualitatively in agreement with what such a curve would look like: the encircled energy asymptotically approaches a constant value at the last measured points. Users should be aware that there *is* some flux outside 1 arcsecond radius, especially in the ultraviolet, but this flux is not considered "useful" and its contribution to the total DQE is not included.

A thorough discussion is given in FOC Instrument Science Report FOC-085.

The fluxes of the spectrophotometric standards within 1" were compared with SYNPHOT predictions. The spectrophotometric standards had been recalibrated using the best model of the white dwarf star G191B2B to redetermine the IUE sensitivity calibration (a correction of several percent in the 1200-2000 Å wavelength range). It was found that the observed/expected flux values depended on wavelength linearly for the reasons outlined in the previous paragraph, so the DQE curve was transformed by this linear function to derive the new DQE curve.

The overall (OTA + COSTAR + FOC) central absolute quantum efficiency $Q(\lambda)$ in counts photon^{-1} with no filters in the beam is plotted and tabulated as a function of wavelength in Figure 30 and Table 11 for the four FOC imaging and spectrographic configurations. The data represent the product of in-orbit measurements for the F/96 relay+OTA absolute quantum efficiency, and ground-based reflectance calibrations of the COSTAR mirrors for the F/48. The predicted loss of light from two reflections of MgF_2 coated aluminum COSTAR mirrors amounts to a 20% loss in the visible and a 35% loss in the ultraviolet. The loss due to the COSTAR mirrors is more than compensated by the improvement in image quality, since the encircled energy performance is improved from 18% within a 0.1" radius to $\cong$ 80% within the same area, based on theoretical PSFs. This data also includes the obscuration of the OTA, unlike the curves in previous versions of the Handbook. As a result, these data can be directly compared with the throughput tables produced by SYNPHOT.

The spectrograph efficiency is shown for the four orders of the grating (I, II, III and IV) with no order sorting filters in the beam. These measurements were made before launch; no on-orbit calibration of the spectrograph sensitivity has been performed yet, although the observations that have been made show that the ground-based calibrations are consistent at the 50% level.

For the F/96 relay, uncertainties in the DQE curve are approximately ±10% (1σ), while for F/48 errors in the 2000-6500Å range for the imaging modes should not exceed ± 20% and for wavelengths below 2000Å they are expected to be of the order ± 50%. This latter uncertainty should be applied to all the spectrograph data especially in the orders III and IV.

Comparing the FOC UV sensitivity to the STIS MAMA sensitivity, we find that while in the range 1150Å - 2000 Å the FOC UV response is lower than the FUV-MAMA, in the range between 2000Å and 3500Å the sensitivity of the FOC is comparable to the NUV-MAMA. See Figure 31 for a comparison plot of the FOC and NUV-MAMA UV response, for a number of corresponding filters.
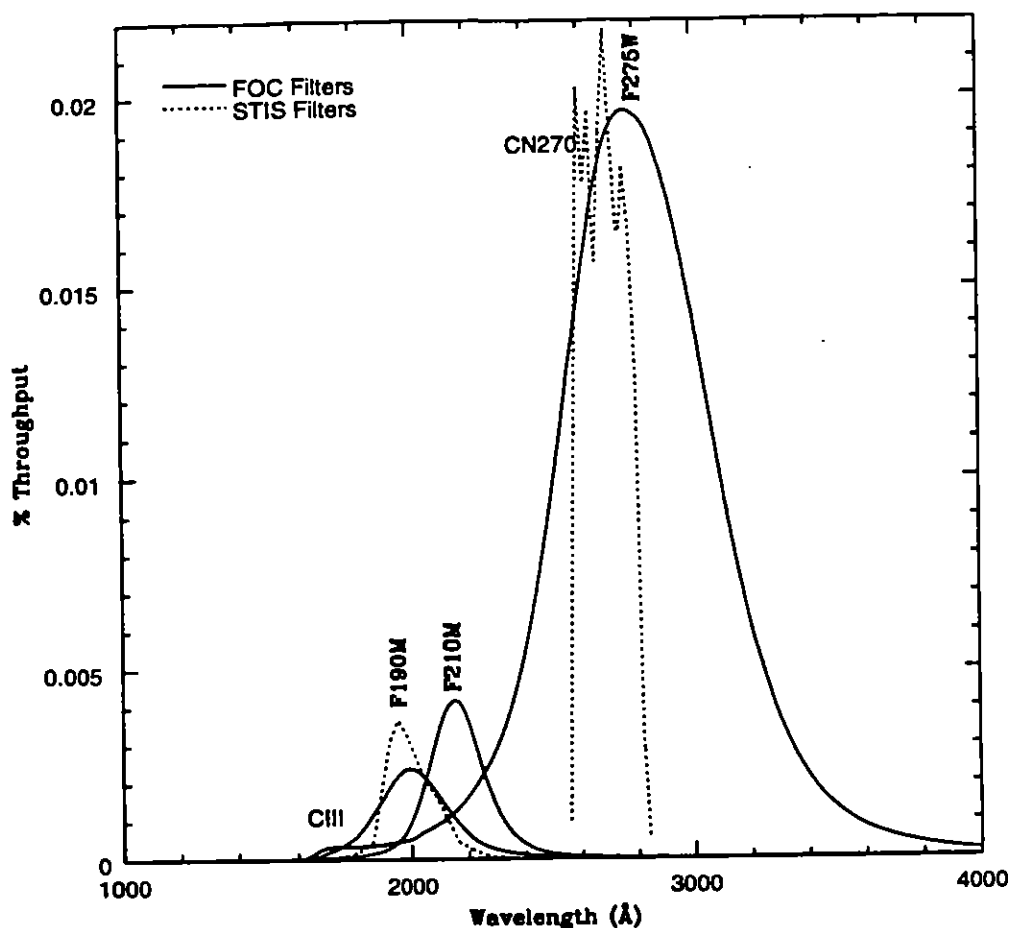
Figure 31. Comparison of FOC + NUV filters to STIS + NUV MAMA + filters.

6.3.1 Format-dependent Effects

It has been found that the DQE is a function of detector format (see Instrument Science Report FOC-075). The cause of this is not known. The relative sensitivities for each format are given in Table 12, where the 512X512 format is set to 1.0 by definition. The DQE values given in Table 11 and Figure 30 refer to the 512X512 format. Typical uncertainties in these numbers are approximately 5%.

Table 12: Format-Dependent Sensitivity Ratios.

Camera	Format (F×L)	Relative Sensitivity
F/96	512z×1024	1.25
	512z×512	1.45
	512×512	≡1.0
	256×256	1.20
	128×128	1.23
F/48	512z×1024	1.44
	256z×1024	1.28
	512×1024	1.02
	512×512	≡1.0
	256×256	0.85

6.4 DETECTOR BACKGROUND

The detector background arises primarily from thermal electrons at the first photocathode and high energy particles. In the 600-km altitude, 28° inclination orbit of HST, substantial fluxes of magnetospheric electrons and protons are encountered in the South Atlantic Anomaly (SAA). The more energetic of these particles are capable of generating intense flashes of Čerenkov radiation in the MgF_2 faceplate of the FOC intensifiers. Since this noise source originates as photons at the very front end of the detector, the Video Processing Unit of the FOC is not able to distinguish between real celestial photons striking the cathode and Čerenkov generated photons.

The threshold energy for Čerenkov radiation in MgF_2 is E>220-keV for electrons and E>400-MeV for protons. Shielding of 4 mm aluminum or more was built into the design of the FOC in order to prevent electrons of energies E < 3-5-MeV from reaching the detectors from any direction.

The effects of the SAA on the FOC were extensively mapped during the commissioning phase. The FOC turned out to be considerably less sensitive to SAA electrons than had been feared. This is presumably due to the additional shielding to electrons provided by the rest of the HST spacecraft. The response of the FOC to SAA protons on the other hand is in good qualitative agreement with the expectations-although the sensitivity of the two FOC detectors differs somewhat.

The highest background rates (0.2-counts $pixel^{-1}$ s^{-1} in the F/48 during nominal operations and 0.02 counts $pixel^{-1}$ s^{-1} in the F/96) are encountered over South America within the peak of the SAA proton density distribution. Since these rates are not high enough to cause damage to the FOC detectors, the FOC is kept fully operational during SAA passages. However, such high background rates do exclude useful scientific observations. A ground-track contour delineating the observed region of high background has been installed within the HST ground system in order that FOC observations not be scheduled within it. Users of the FOC need therefore not concern themselves with avoiding the SAA under normal circumstances (i.e., periods not having unusually high solar activity). The typical detector background rates experienced well outside the SAA are 7

$\times$ 10^{-4} counts pixel^{-1} s^{-1} in the detector for the F/96 relay and 10^{-2} counts pixel^{-1} s^{-1} in the detector for the F/48 relay (see also Section 6.13 for current F/48 performance). Upward fluctuations of a factor $\approx$3 from these minimum values are, however, seen throughout the HST orbit. The minimum in-orbit background rates are, respectively, factors of $\approx$5 and $\approx$3 higher than the background rates measured during ground testing implying that the bulk of detector background counts are particle induced.

6.5 STRAY LIGHT

Normally, the FOC background is dominated by the detector, by zodiacal light in the visible and by geocoronal Lyman alpha and diffuse galactic light in the far UV (see Chapter 7 for detailed calculations of these components). When a bright object such as the Sun, Moon or the bright Earth limb is nearby, however, it may be dominated by stray light reaching the OTA focal plane due to scattering from the baffle system, the OTA tube and dust on the mirror. The observed brightness of stray radiation at the OTA focal plane due to the proximity of the Moon or bright Earth limb in the daytime part of the orbit in V magnitudes arcsec^{-2} as a function of the angle between the Moon or the limb and the OTA axis is shown in Figure 32. These in-orbit calibrations of the baffle attenuation were performed by P. Bely for angles above 30°, while the attenuation for angles less than 30° were derived by D. Elkin. The spectral shape of the stray radiation in the case of the Earth has been assumed to be, for most practical purposes, that of the Earth's daylight radiance given in Figure 33. This data used an *ad hoc* earth albedo published by R. R. Meier (*Space Sci. Reviews*, 58, 1, 1991).

The average zodiacal light background of 120 S10 corresponding to $V \cong 23$ magnitudes arc-sec^{-2} is reached at angles greater than 80° to the limb, approximately. For viewing configurations in which the angle is less than this value, stray light will dominate in most situations. One of the most interesting of these is that encountered when observing in the continuous viewing zones (CVZ) which, in principle, allows for long uninterrupted integrations of very faint sources. Due to the altitude of the spacecraft and the depression of the horizon, the off-axis angle to the Earth limb in the CVZ will be in the range 20° - 44°, approximately. From Figure 32, the expected stray light illumination in this configuration in the visible will be between 20th and 23rd magnitudes arcsec^{-2}. This means that observations in the visible will be limited mainly by this source of background. Below 3400Å, however, this effect will be negligible, as shown in Figure 33, providing an opportunity to use the CVZ for the detection of faint sources with the minimum level of background light.

It is of more than passing interest for observers to pay some attention to the maximum allowable background they can tolerate for their specific observation. The most heavily affected observations are those of faint extended sources, where the background can have comparable count rates. For example, a spiral galaxy with B=20.5 magnitudes arcsec^{-2} could be observed with the F430W filter and achieve a S/N of 10 over a 0.1"x0.1" region in 57 minutes under average observing conditions. Generally this would require a CVZ observation since most orbit viewing periods are only about 50 minutes long (on average). However, in the CVZ, the stray light can be as bright as V=21 magnitudes arcsecond^{-2}, which would require a 83 minute exposure to obtain the same S/N. This situation can be remedied by specifying the Special Requirement 'SHADOW' to force the observations to be taken only during Earth shadow. For the CVZ observations, this would constrain the observations to be scheduled for orientations of low stray light insuring the best possible S/N. Another special requirement that can be used to limit the amount of bacground light is the
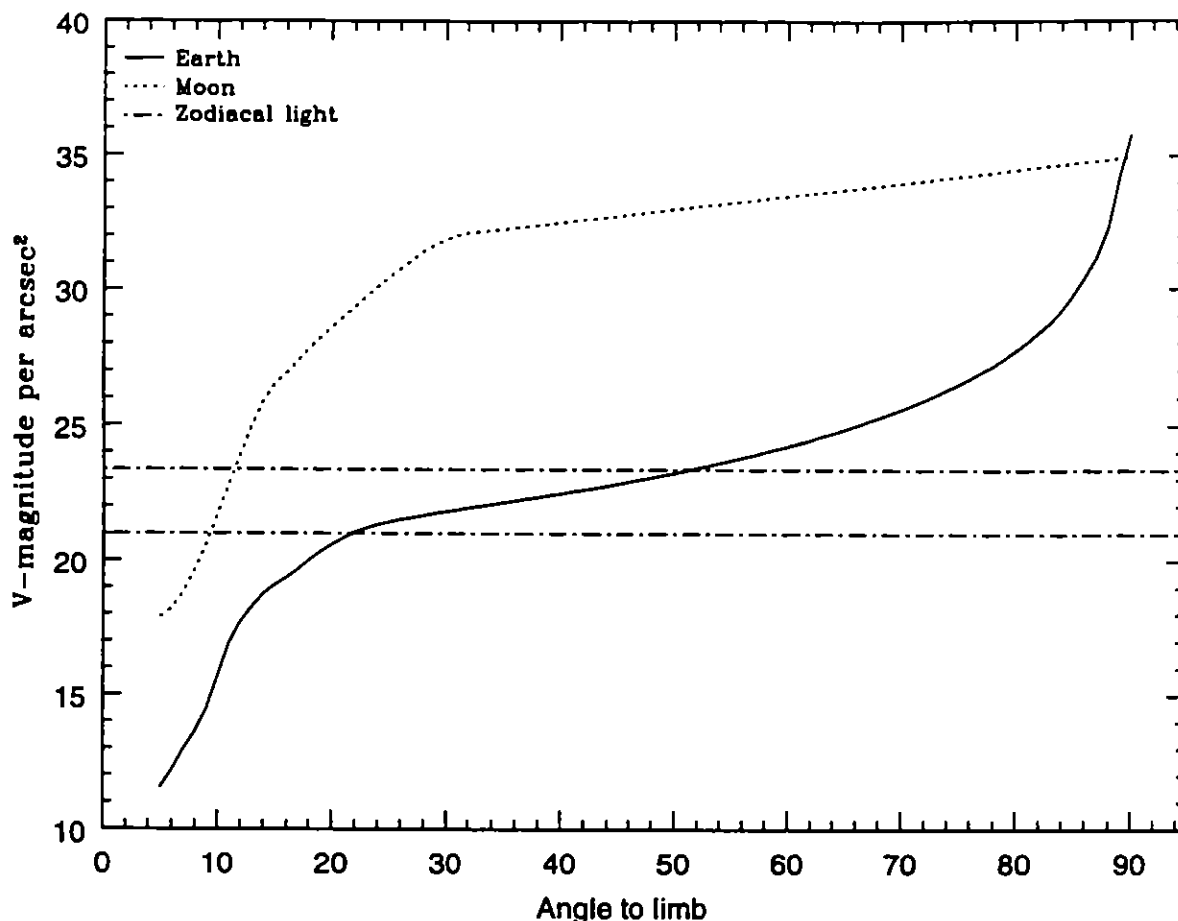
Figure 32. Stray light illumination in V magnitudes arcseconds^{-2} at the OTA focal plane due to the Moon and daylit Earth as a function of off-axis angle determined from in-orbit observations. Limits on zodiacal light contribution are also given.

'LOW SKY' requirement, which forces the observation to be taken only when the background can stay within 30% of the minimum obtainable levels. The 'LOW SKY' requirement can not be used with CVZ observations, unlike the 'SHADOW' requirement. These requirements should be considered for all observations requiring low background levels, especially background from stray light, and included in the Phase II proposal if deemed necessary. These considerations can dramatically improve the detection of faint targets.

6.6 DETECTOR OVERLOAD AND BRIGHTNESS LIMITS

The FOC detectors described in Section 4.6 may be damaged by illumination levels exceeding 10^7 photons s^{-1} pix^{-1} at the photocathode due to point sources and by an average illumination from a diffuse source over the whole photocathode exceeding 10^4 photons s^{-1} pix^{-1}. Because of this danger, the 36 kV HV power supply on the 3 stage image intensifier is set to trip off when the point source illumination exceeds the value given above or if the average illumination from a diffuse source exceeds 200 photons s^{-1} pix^{-1}. Thus, for safety reasons, no point source delivering more than 10^6 photons s^{-1} pix^{-1} at the photocathode or a diffuse source delivering more than an average rate of 100 photons s^{-1} pix^{-1} over the whole photocathode will be allowed to be imaged by the FOC. These values correspond to an 9th magnitude blue star or a diffuse source of surface
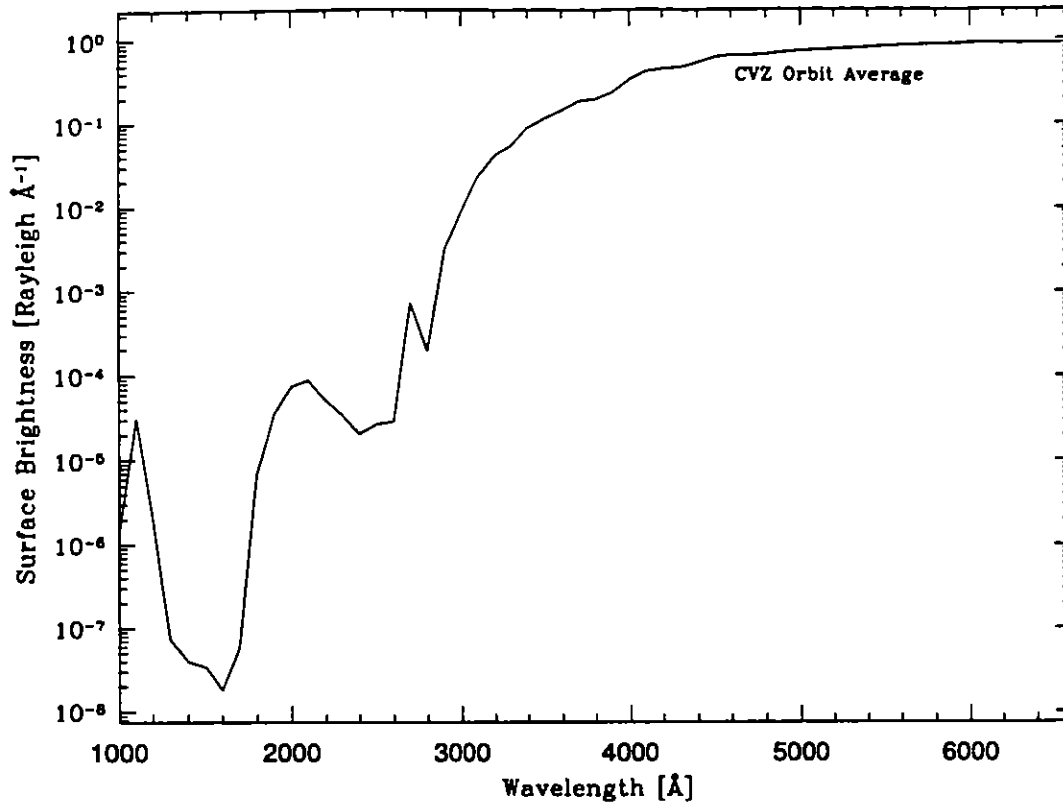
Figure 33. The Earth daylight radiance for an average orbit of CVZ observing in Rayleighs Å⁻¹
          as a function of wavelength. This corresponds to a background of about 22 V magnitudes arcsec² and assumes the sun is providing most of the stray light.

brightness 10 magnitudes arcsec⁻² viewed through the F430W filter with the F/96 relay. Targets brighter than this limit can still be observed by the FOC, provided that 1) sufficient filters are selected, so that a linear countrate is observed by the FOC, 2) the filter configuration is checked prior to the observation [*Special Requirement CHECK-FILTER = YES*].

Currently, we cannot estimate the long term effects on the camera of exposures to high count rates (> 100 cts/sec/pix). We therefore require that, for ALL FOC observations, the filter configurations be fine tuned so that the observed countrate is maintained within the linear regime, even in cases where the targets are fainter than the above-mentioned safety limit. In very special cases, the Instrument Scientist can waive this requirement, upon presentation of a compelling scientific justification.

6.7 OVERHEAD TIMES AND MULTIPLE EXPOSURES

Assuming that the standard science data dump operations at the 32 kHz rate apply, it will take a constant 3.9 minutes plus a variable component to transition from the absolute time tag to stop an exposure to the absolute time tag to start the next one. The variable component depends on the mode change required and can be up to another 3.5 minutes for the worst case with the F/96 relay (4 filter-wheels) to 1.9 minutes for the worst case with the F/48 relay (2 filter wheels). Thus, it could take up to a total of 7.4 and 5.8 minutes of time between successive exposures with an average of approximately, 6 and 5 minutes for the F/96 and the F/48 relays, respectively. If no changes

to FOC mechanisms are required, the time interval between exposures can be reduced to 23 seconds total. This is the fastest rate at which the FOC presently can be run provided the telescope can be slewed to a new position on the detector quickly enough to permit it.

All the overhead times reported here are to be considered approximated, and should not be used for an accurate calculation of the required time (See the Proposal Instructions for a detailed and accurate description of all the relevant overheads).

6.8 GUIDING MODES WITH THE FOC

The FOC will default to fine lock (estimated RMS jitter 0.005 arcseconds out of day/night transitions) for all configurations. Users may not specify coarse track for their observations since it has been determined that guiding in this mode has a detrimental effect on the FGSs. Similarly, gyro hold may not be used because the large pointing and stability uncertainties are not conducive to optimization of the science.

Occasionally, it will be found that two guide stars are not available for an observation. In that case, STScI will notify the PI and offer the possibility of single guide star observing. For relatively short exposure times (<2000s), the impact on performance is very small. The observation will not be executed in this mode unless the PI gives approval.

Sometimes the FGSs fail to achieve fine lock for an observation. In this case, the Take Data Flag comes down, the shutter is not opened, and the users are notified of what happened.

6.9 UNIFORMITY OF RESPONSE (FLAT FIELDING)

The extended format ($512z \times 1024$) geometrically corrected flat fields for both of the new relays are shown in Figures A1-A2. The F/48 image shows the approximate location of the new default 512×512 format, which is no longer at the center, but close to the upper right quadrant. The flat fields were obtained from overlapped observations of the inner region of the Orion Nebula and are at 3727 and 1360Å respectively. The flat fields show a number of various types of features, some more subtle than others. The more evident features are the occulting fingers for the F/96 relay, the slit finger for the F/48 relay (used as a fiducial reference to the spectrograph slit) and the reseau marks. Because of the geometric correction, the edges of the original raw images can be seen as curved edges in these images, mainly on the left and right sides.

Because of the large amount of time necessary to obtain external flat fields for the FOC, these two UV flat fields (one for F/96 and one for F/48) are currently the only UV flat fields for the FOC. We obtained another UV flat field at about 2200Å, which has been analyzed, although its quality assessment has not been completed yet.

In all images, regardless of format, a number of pixels at the beginning of the scan line (*i.e.*, starting at S=1) are corrupted by defects in the beginning of the scanning sawtooth waveform. The number of pixels corrupted depends on the detector and format. Generally it is about 5% of the scan line for the F/96 relay and relatively independent of format, whereas for the F/48 relay it gets progressively worse with smaller formats (for the 128×128 format it is as much as 25% of the scan line). The faint horizontal stripes seen at small L values are due to a ripple instability of the coil drivers at the beginning of a frame.

The narrow line running from the bottom left corner to the upper right corner is due to the read beam not being completely blanked when it is forced to fly back to S=0, L=0 at the end of the frame. This feature is more noticeable with the smaller formats. The narrow horizontal features at

the right edge, especially at L=256, 512, 768, are due to noise glitches on the scan coil driver caused by changes in the most significant bits of the line counter. For both relays, the center 512 × 512 is seen outlined in larger formats. This effect is due to a burn-in of that heavily used format in the camera target so that a charge discontinuity at the edges of the format has appeared. The edges of a square baffle located just in front of the detectors limit the extended field of the F/96 relay at the upper and lower left corners, the extended image field of the F/48 relay on the upper left corner. The broad vertical bands (bright and dark) seen near the beginning of the scan line arise from ripples at the beginning of the scanning sawtooth waveform. The bands occur as a result of the varying pixel size which is a consequence of the varying scan rate at the beginning of the scan. If they were only an effect of geometric distortion, a proper geometric correction would remove this effect; however, the new geometric correction files for F/96 do take scan line variations into account, and do not seem to remove the effect entirely. It will be possible to remove residual effects with format dependent flat fields, but at the moment they are not applied by the normal pipeline calibration (the normal pipeline calibration of the images always uses the appropriate section of a full format flat field to flatten images obtained in all formats).

The remaining features fall into two categories, large scale and small scale features. The large scale variations are due either to vignetting (significant only for the F/48 relay) or detector response. The expected vignetting for the full the F/48 full field format is shown in Figure 34a as a contour plot. Contours are shown as percentage transmission. The expected vignetting has not been included in the flat field for the F/48 relay shown in Figure A1 so that features closer to the edge can be better seen. Figure 34b shows the vignetting function along the long slit.
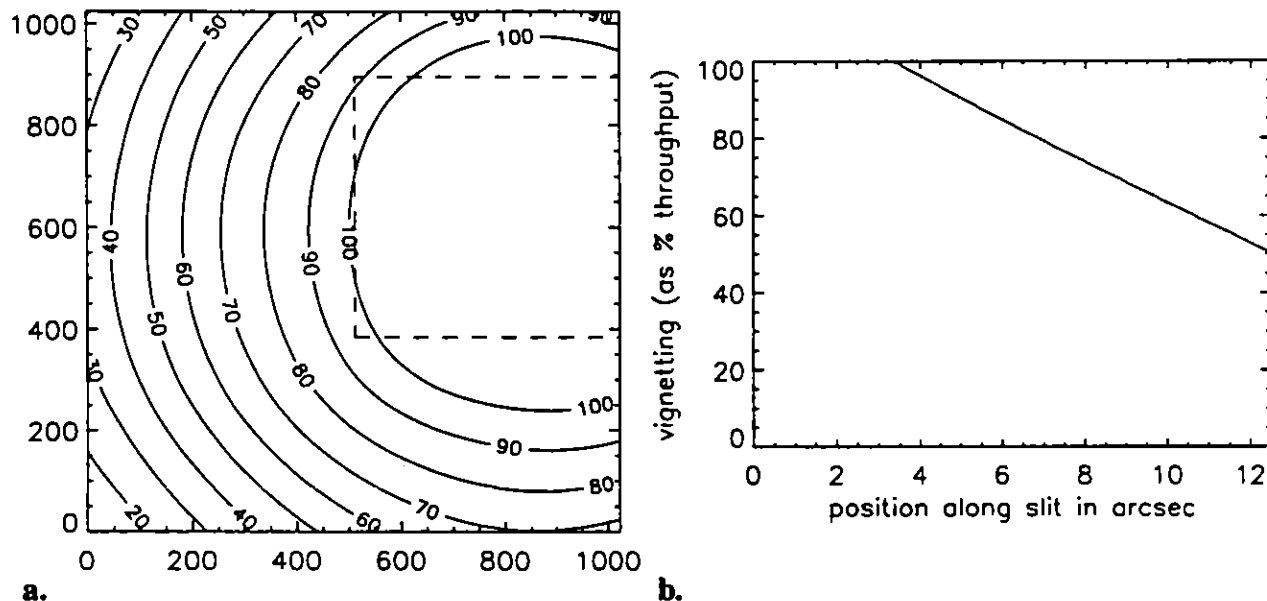

Figure 34. a. Contour plot of the vignetting function for the F/48 relay across the entire photo-cathode, with the location of the primary 512 × 512 imaging format shown (dotted line). b. Plot of the vignetting function along the spectrographic slit.

Contour plots of smoothed flat fields, including the effects of vignetting for the F/48 relay, are shown in Figure 35. A gaussian with a FWHM of 9 pixels was used to smooth the image and the result was normalized to 100 at the center. Figure 36a and 36b show a plot of row 300 of a UV flat field for the F/48 relay and the F/96 relay respectively to give a better idea of the size of the flat field variations.
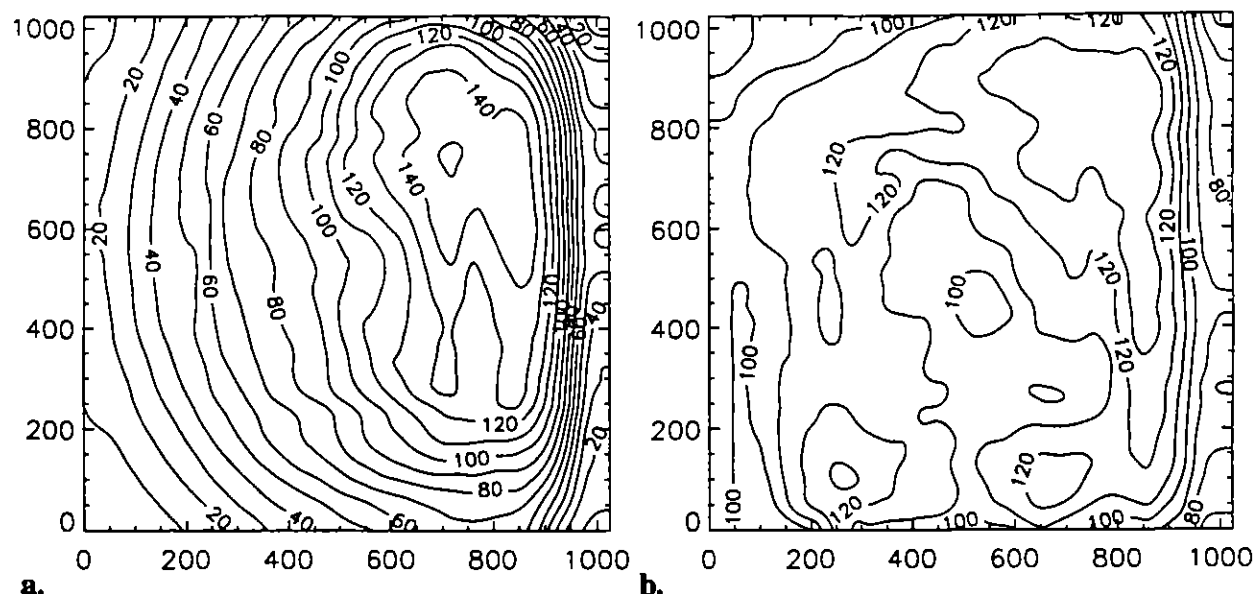
Figure 35. **a.** Contour plot of the smoothed flat field for the F/48 relay, including the effects of vignetting. **b.** Contour plot of the smoothed flat field for the F/96 relay.
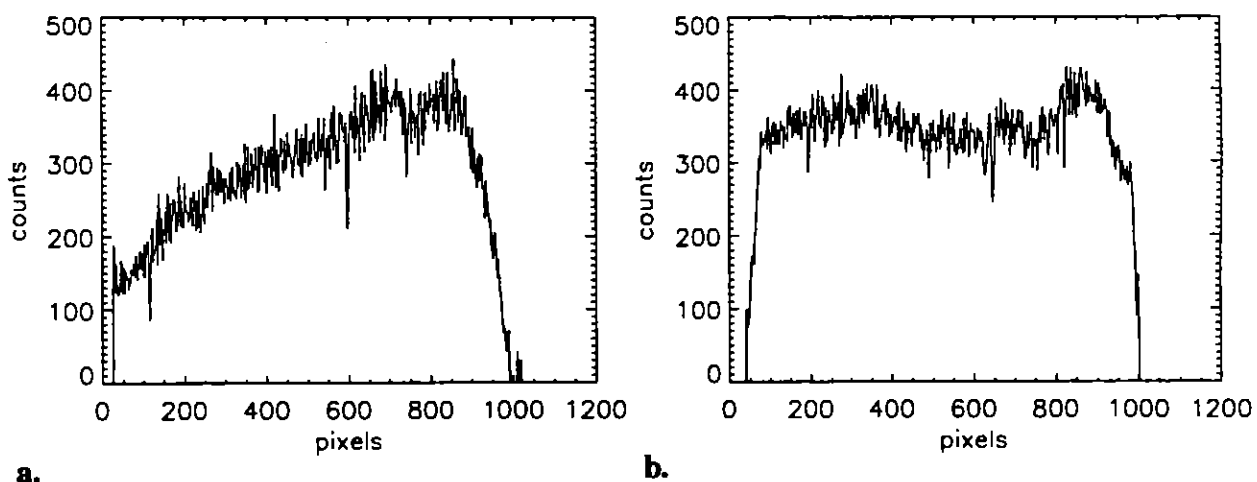

Figure 36. Plots across row 300 of the UV flat field for the F/48 relay (a) and the F/96 relay (b). The effect of vignetting has not been included in plot (a).

All previous indications are that the relative variations in large scale response as a function of wavelength between 1300 and 6000Å are weak; generally speaking, the large scale response does not change more than 10% at all pixels except at the edges and corner of the full format. Figure 37a and 37b show contour plots of the ratio of the Orion Nebula derived flat fields to those obtained from the onboard LEDs for the F/48 and the F/96 relays respectively.

Beyond 6000Å, the flat fields begin to change significantly, generally with poorer relative sensitivity towards the corners. Although the changes in the large scale response with wavelength are relatively minor, the changes in the fine scale features is more pronounced. Scratches and other small scale defects deepen in the far UV; for the F/96, some scratches exhibit as much as a 30% decline in sensitivity in the far UV. Another source of fine scale nonuniformity is the presence of
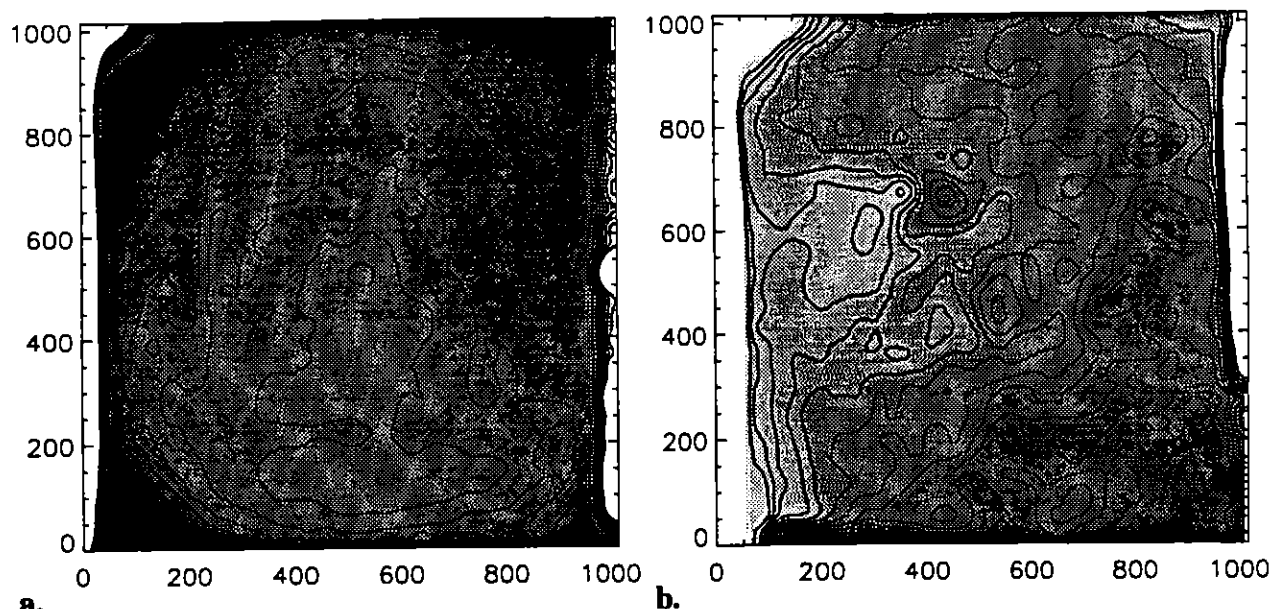
Figure 37. Contour plot of the ratio between external UV flat field and internal LED flat field for the F/48 relay (a) and the F/96 relay (b) based on pre-COSTAR data. The expected effects of vignetting on the ratio for the F/48 relay are not included. The center of each plot has been normalized to 1 with the contours at intervals of 2.5%.

patterns--unfortunately not fixed. Although not always easily seen in low count extended areas or flat fields, there are two different patterns always present. The more noticeable one is an approximately sinusoidal pattern with the peaks and troughs oriented at an approximately 45 degree position angle and a period of 3.35 pixels for the F/96 relay. It is believed to originate from a moiré effect between a TV tube grid and the diode array on the target. The RMS amplitude of this pattern is approximately 5% for the F/96 relay and 2.5% for the F/48 relay (the peak deviations from a flat response due to this pattern are at least twice these values). This pattern becomes intensified when count rates are in the nonlinear regime and thus is much more easily seen. In fact, it is a quick way of recognizing serious nonlinearity in an image. The pattern noise disappears at very low count rates.

A second pattern arises from some form of interference with an FOC digital timing waveform that has a 4 pixel period. It shows up as vertically striped patterns on the flat fields. Although very coherent in nature with regard to orientation and frequency, the details of the modulation do not appear to remain constant from image to image. The RMS amplitude of this pattern is approximately 2.5% for both relays.

There also appears to be an intrinsic granularity in the fine scale response, i.e., effectively random pixel-to-pixel variations in response which has not yet been well characterized.

Some comments on flat field calibration are in order, especially with regard to the routine pipeline calibration. Small drifts in distortion of the order of a pixel result in misregistration of fine scale features such as scratches between the flat field and the science image. Flat fielding the data in this case actually worsens the effects of the fine scale features by correcting the wrong pixels. For this reason and because FOC flat fields are of relatively low signal to noise (typically 300-500 counts per pixel), the flat fields used in RSDP are heavily smoothed to eliminate most of the fine scale features. As a consequence, they are not corrected for in the calibrated outputs of RSDP.

Unsmoothed flat fields are available from the FOC WWW pages or the STScI ftp directories (see Chapter 9 for more details), and by using them, it is often possible to improve the flat fielding by the appropriate registration of the flat field to the science image. But this requires scientific judgment and must be applied on a case-by-case basis.

One final effect should be mentioned. Although it is not a flat field issue, it appears to many at first glance to be one, and so it will be explained here. Many observers see a fringe or fingerprint type of pattern in the background of their calibrated images where the fringes are of relatively low spatial frequency—usually of periods of 20 or more pixels. It is a result of the geometric correction applied to the data. It does not appear in the raw data. What is being seen is not alternating areas of darker and brighter background, but rather, alternating areas of higher and lower variance in the poissonian noise of the background. This effect arises from the resampling algorithm used in the geometric correction--essentially what one is seeing is the effect of the pixels in the output, geometrically corrected image drifting in and out of phase with the corresponding pixels in the input, distorted image. Those pixels mapping directly to the center of a pixel in the input image result in little or no effective smoothing, while those which map to a point in between pixels in the input image will be an average of the input pixels and thus have smaller variance in the noise. A small amount of further smoothing to the geometrically corrected image will virtually eliminate the effect. The pattern is identical in all images as long as they use the same geometric correction file.

The achievable relative photometric accuracy depends on many factors, of course, and no simple rule of thumb will apply to all analyses. In many cases the accuracy depends on the amount of work an observer is willing to do to calibrate his data. For RSDP calibrated files, one should not expect the large scale accuracy to be better than 3-5% over the central region of the format, and should expect errors as large as 10% closer to the edges (much higher very close to the edges). Fine scale features can introduce large pixel-to-pixel errors (*i.e.*, scratches and reseau marks). Scratches and blemishes can be dealt with by careful flat fielding. It is sometimes possible to remove the pattern noise with special techniques. Most important is to avoid placing targets on or near areas with serious photometric problems if possible. That is, keep targets of interest way from the edges of the format, burn-in regions, A/D glitches and known blemishes if more accurate photometry is desired.

6.10 VISIBLE LEAKS

Although the FOC narrow and medium band filters are as good as the technology of 15-20 years ago could provide, they do exhibit a residual transmission of $\cong 10^{-3}$ - 10^{-4} between 5000 and 6000Å where the detectors are still relatively sensitive. Consequently, indiscriminate use of these filters to isolate faint UV features from a bright visible background can lead to serious errors. The magnitude of the error is, of course, very sensitive to the precise shape of the spectrum of the source to be observed throughout the sensitive range of the FOC. Thus, it is not always sufficient to know only the expected flux of the source in the range $\lambda_0 \pm \Delta\lambda/2$ in order to estimate the expected count rate.

A striking example of a possible observing scenario that can be expected when imaging a bright visible source in the UV is shown in Figure 38. In the example shown in this figure, the source spectrum is assumed to increase sharply with increasing wavelength in the manner expected from an M supergiant star. If this source is fed into the F/96 relay with the F231M filter on FW#3 in the beam, the resulting monochromatic count rate as a function of wavelength
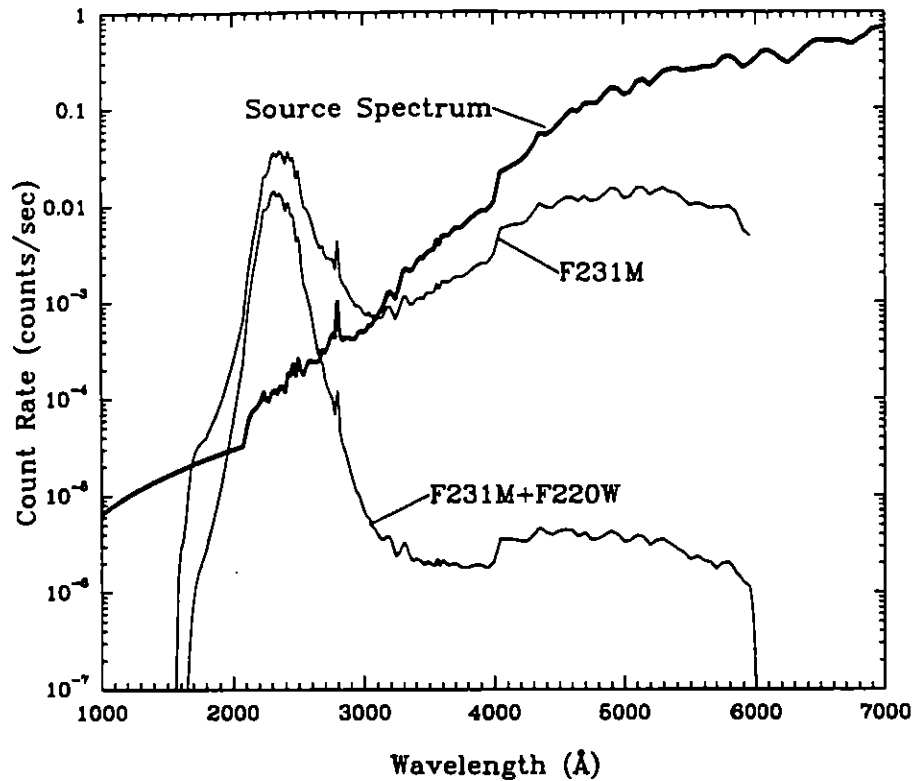
Figure 38. The expected monochromatic count rate as a function of wavelength for the F/96 relay and the F231M filter or the F231M+F220W filters in the beam for an extended source whose spectrum varies as the curve marked SOURCE SPECTRUM. The source flux units are photons $cm^{-2}sec^{-1}\AA^{-1}$.

through the entire OTA+COSTAR+FOC system is shown by the curve marked F231M. The actual observed count rate in this configuration, of course, corresponds to the integral of this curve.

If the F231M filter alone is used in this endeavour, the contribution of the flux within the band $2330 \pm 115\AA$ is only $\cong 18\%$ of the total of 39 counts sec^{-1}. The counts originating from the region $\lambda > 2580\AA$ represent, in contrast, 71% of the total. In this admittedly extreme case, the thus derived UV brightness would be highly suspect, to say the least. Solutions to this problem are not easy to find but, at least for the F/96 relay, one simple device would be to introduce a second cleverly selected filter into the beam in addition to the original one. This selection should be geared towards maximizing the suppression of the visible leak while minimizing absorption in the UV bandpass of interest.

In the case worked out in Figure 38, for example, the F220W filter on FW#2 is ideal as shown by the curve marked F231M+F220W. Now, the in-band fraction of counts amounts to 69% while the visible leak is only 5% or less of the total. The exposure time required to reach a S/N=10 in this case increases by a factor of six mainly because of the effective suppression of the visible counts.

Unfortunately, the F/48 relay with its much smaller filter complement has far less flexibility in this regard than the F/96 relay. In this case, another possible solution to the problem is to use the objective prisms to physically separate the UV from the visible. This technique works best for point or, at least, compact sources where spatial and spectral overlap is minimized. But even for extended sources, appropriate positioning of the target with respect to the dispersion axis of the

prism can work quite well. At that point, the only remaining problem is to insure that the overload limit of the detector (described in Section 6.6) is not violated for the visible part of the image.

6.11 GEOMETRIC DISTORTION AND STABILITY

Because of the nature of the detectors, and the off-axis location of the instrument, the raw FOC data suffers from geometric distortion, *i.e.*, the spatial relations between objects on the sky are not preserved in the raw images produced by the FOC cameras. This geometric distortion can be viewed as originating from two distinct sources. The first of these, optical distortion, is external to the detectors and derives from the off-axis nature of the instrument apertures. The second, and much more significant source of distortion is the detector itself.

Geometric distortion is a fact of life when dealing with detectors containing image intensifiers, primarily because intensifiers rely on an electric field for accelerating, and a magnetic field for focusing the photoelectrons. Any variation in the uniformity of either results in image distortion within the intensifier. Photon positions are then further distorted in the process of "reading-out" the TV tube's target, firstly because the read-out beam is performing an angular sweep across a plane target, and secondly because of non-uniformities in the scanning rate of the beam. For this reason, each video format has individual distortion characteristics, and so unfortunately, the distortion measured for one format cannot be used to correct the distortion of an exposure taken in another format.

In past cycles, the distortion correction model had been based on the measured location of the reseau marks—fiducial reference points etched onto the first of the bi-alkali photocathodes in the intensifier tube. (Since these reseau marks only transmit about 10% of the incident light, for all practical purposes they cannot be flat fielded out.) These reseau marks form an orthogonal grid of 17 rows and 17 columns with a separation of 1.5 mm (60 pixels), each reseau being 75 microns square (3 X 3 pixels). The detector distortion was determined by illuminating the photocathode with an internal light source, (*i.e.*, an internal flat field). The observed positions of the reseau marks, when compared to the expected positions, provide a map of the detector distortion across the field. The optical component of the distortion is determined independently from ray-tracing models of the HST and FOC optics, and is applied to the reference reseau grid to give the 'expected' positions.

Unfortunately, the detector distortion for the FOC clearly has variations on spatial scales smaller than the spacing of these reseau marks (particularly near the scan line beginning), and as a result, models based only on the reseau marks do not adequately represent the true distortion. A new method of determining distortion was developed which is based on overlapping observations of crowded starfields to determined the net distortion (the optical distortion is naturally included in this method of determining the distortion). These observations were then used to determine a two-dimensional spline distortion model which in turn was used to generate the new geometric correction files. The improvement in quality is most apparent for smaller formats where the small number of visible reseaux prevented the determination of a good model. The new geometric correction files have been used in the calibration pipeline for F/96 data since 19 March 1995 (F/48 geometric correction files are still based on reseau marks). As an aside, only those who desire sub pixel accuracy in position measurements or those who have used the 256X256 format should even consider reprocessing data taken prior to this date with the new geometric correction files. For most, the improvements will not have a significant effect on their positions or photometry.

Although the geometric distortion arises from several sources, the correction of images is car-

ried out in a single step using a flux-conserving algorithm which maps values from the raw, distorted image into a geometrically corrected image. Figures 39 and 40 show as an example the magnitude of the distortion field as determined for the pre-COSTAR F/48 and pre-COSTAR F/96 cameras using their $512z \times 1024$ formats, from in-flight calibrations (the differences arising from the change in the new distortion and the optical distortion from the use of COSTAR amount to only a few pixels at most; these figures are intended to show the global distortion effects).

The squares show where a regular grid of points on the sky (using a 60 pixel spacing) should have appeared if there were no distortion; the ends of the line segments show where the grid points actually appear in the distorted image. (The lines have been multiplied by a factor of 2 to make them more easily visible, *e.g.*, a line length of 50 pixels represents a distortion displacement of 25 pixels). The pixel coordinates shown refer to normal, square pixels, rather than the rectangular, zoomed pixel mode the images were obtained in.

In order to carry out geometric correction of FOC data, *i.e.*, to recover an image in which the spatial relationships between objects are restored, a necessary requirement is that the geometric distortion field, shown in Figures 39 and 40, must be stable. By this we mean that there must be no significant change in the observed reseau positions with time.
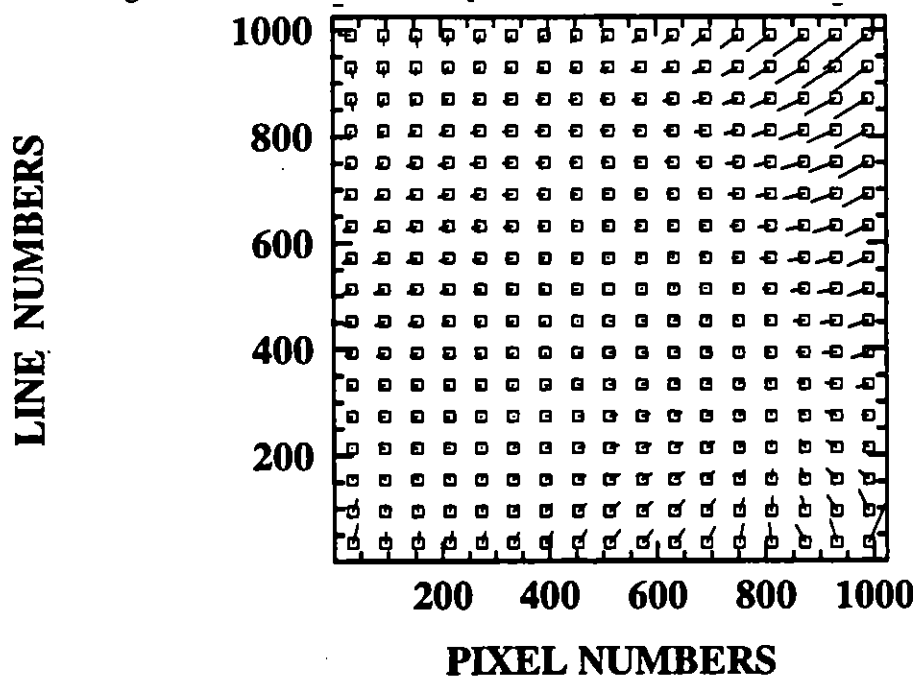
Figure 39. The $512z \times 1024$ format distortion field for the F/48 relay.

Short term variation of the geometric distortion pattern occurs during the period immediately following FOC high voltage switch-on. During this time the observed reseau positions show an RMS deviation from the stable positions of approximately 1-2 pixels. This period however, extends for only about 40 minutes, by which time the reseau position have stabilized to within 0.5 pixels, which is considered adequate for imaging purposes. In order to avoid this period of instability, the scheduling software automatically inserts a delay interval immediately following high voltage switch-on which prevents exposures being taken during this time. Long term variations in the geometric distortion were expected to occur as a result of desorption and out-gassing in the OTA and instruments, however given the time since launch, the desorption curve is now consider-
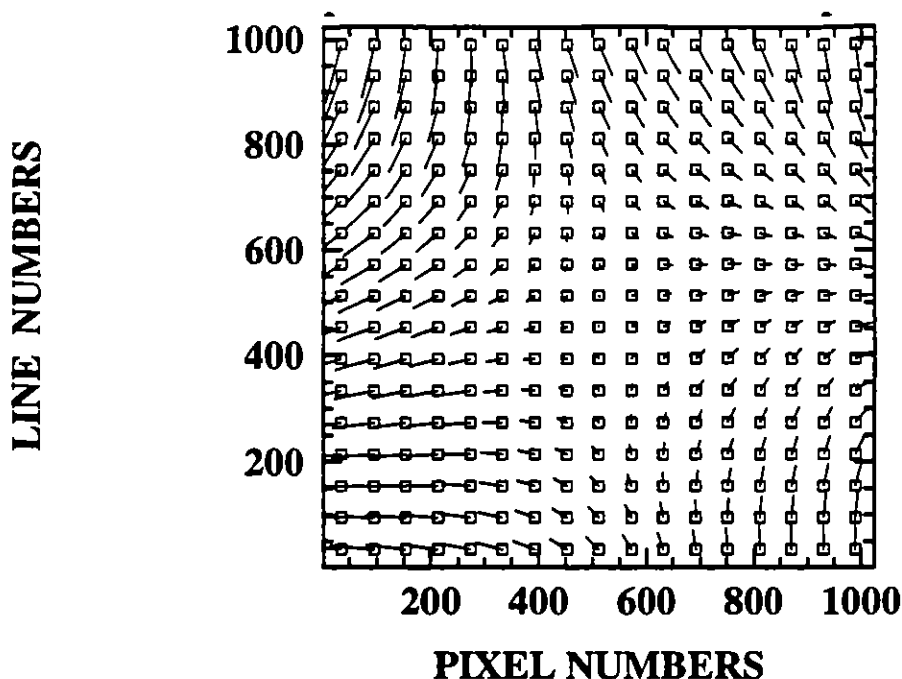
Figure 40. The 512z × 1024 format distortion field for the F/96 relay.

ably flatter and out-gassing should be very near stable. Consequently, effects on distortion are much smaller and are taking longer to materialize. Based on our experience;

a. The F/96 relay continues to be very stable, the geometric variation in the F/96 relay has shown only about 1-2 pixels of movement since launch, (which theoretically should be the worst time).

b. Although most of the variation in distortion resulting from the high voltage turn-on has happened during the warm-up period where data is not normally taken, there is still some residual variation over the next 2 hours. Those PIs needing the ultimate in geometric stability should specify such on their proposal.

c. There are as much as 0.5% changes in effective plate scale between different high voltage turn-ons.

d. The situation with the F/48 relay is somewhat less certain since monitoring of the pre-COSTAR F/48 relay has shown it to be considerably less stable, with several large, unexplained changes in the geometric configuration. No systematic information exists for post-COSTAR data, due to the high voltage problems. All F/48 data must be considered to be poorly characterized with respect to geometric distortion.

6.12 PLATE SCALE

The plate scale (i.e., the pixel size in arcseconds) had been determined for both of the FOC relays prior to the deployment of COSTAR. This was done by taking a series of images of a pair of astrometric stars, moving the telescope between exposures by a predetermined angular offset. The measured distances (in pixels) between the astrometric stars, combined with the known separation (in arc seconds) then give us the plate scale. The effects of COSTAR on the focal ratio of the image was then applied to these values to obtain preliminary plate scales.

Due to problems observing with the F/48 relay since the deployment of COSTAR, the preliminary plate scale of 0.02825 arcsec pixel^{-1} remains the only value available, with an error of $\pm$0.0002 arcsec pixel^{-1} based solely on the pre-COSTAR calibrations. Observations of a field of stars already observed prior to COSTAR deployment were used to determine the new plate scale for the F/96 relay. The derived plate scale for the F/96 relay is 0.01435 arcsec pixel^{-1} ($\pm$0.0002). This value has been verified using astrometric observations.

Calibration programs have shown that these plate scales will provide separations between close pairs of stars to within 0.4 pixels (or about 0.0057 arcsec for the F/96), while the separations between widely spaced stars are good to within 0.25%. This is due to a combination of effects including centroiding accuracy . However, the main error comes from the stabilization of the FOC image after it is turned on for an observation run. Early calibrations (discussed in Instrument Science Report FOC-045) showed that the plate scale and geometric distortion varies for several hours after initial high-voltage turn on. The plate scale, for example, only changes by about 0.25% in the first few hours then remains relatively stable afterwards. This variation can be important to an observer requiring the same astrometry for all their images, in which case, comments should be made in the Phase II proposal stating that the visit shouldn't start immediately after HV turn-on.

6.13 CURRENT F/48 PERFORMANCE

The first failure of the F/48 camera to turn on occurred in September 1992. The high voltage tripped during its ramping up, at the beginning of an observation sequence. The F/48 camera was switched on again successfully in October 1992, and a number of darks and flat fields were taken which confirmed background values more than ten times higher than nominal. The next switch on attempt (January 1993) failed, but the F/48 was again successfully switched on December 22, 1993, before the deployment of the COSTAR corrective optics. The camera remained on for the duration of the observation. While the acquisition image showed a background level consistently high with the previous dark count images, a preliminary analysis of the following frames showed that the background increased dramatically with time, eventually reaching saturation levels approximately two hours after HV switch-on. As a consequence, the F/48 was not made available to GOs during Cycle 4 and 5, while extensive tests were carried out to establish its performance and operational reliability.

After a long period of inactivity, the F/48 was switched on again in November 1994, for the first time after the COSTAR deployment. Images and spectra of an extended target were successfully obtained, and showed a completely different behavior from the earlier tests.

A direct comparison of all nine spectra taken during the November test was made to determine the characteristics of the background as a function of time after switch-on. The high background was still localized in the central area of the image (flare), and in the upper arc across the top of the images. The locations of these features can be seen in Figure 41, where all the images are displayed with the same intensity contrast to allow direct visual comparison. But, it was clear from a cursory comparison that instead of increasing in intensity over time, the flare actually tended to subside over time since switch-on.

This finding was confirmed in the course of three additional successful turn-ons, on March 5 on March 30, and on April 18, 1995. In all cases the background decreased significantly as a function of time, to reach a value lower than 10^{-2} cts/sec/pix after approximately 250 minutes after switch-on. The F/48 camera was switched on again in December 1995, to execute successfully the first scientific program. The background behaved as expected, continuing the diminishing trend
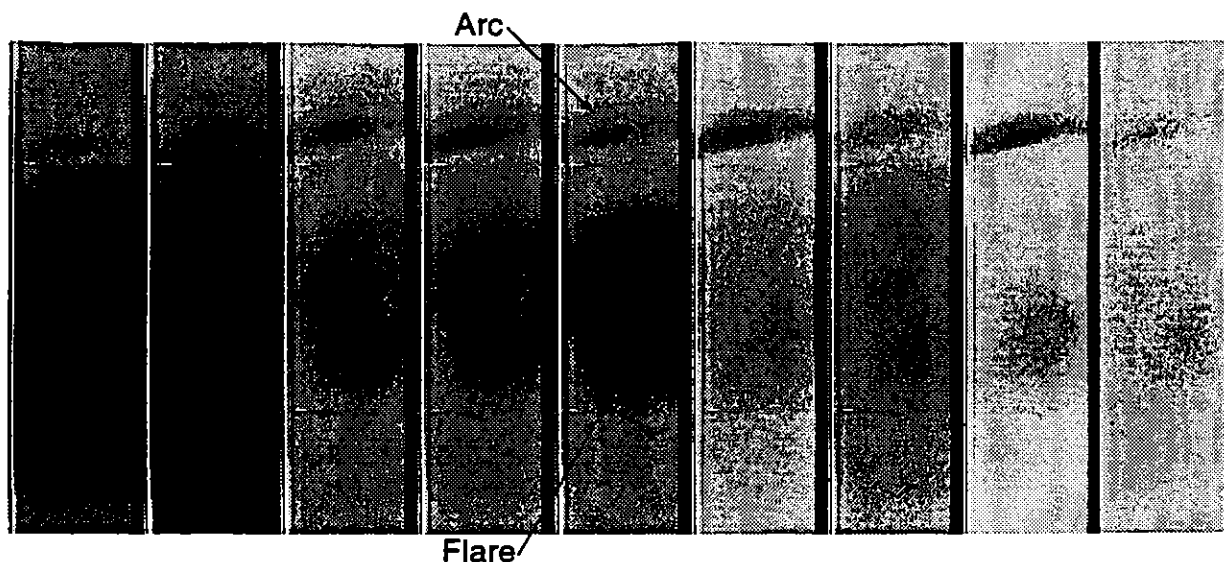
Figure 41. Mosaic of F/48 Images taken ordered by time after switch-on during the November 1994 test. Earliest image is on the left. All are displayed with respect to the same count rate scale, to show how the flare actually tended to subside over time since switch-on. The regions of the flare and arc are marked in the center image.

already noticed in the previous run. In Figure 42, the background is measured in three sample regions (flare, arc, background) in the images taken during the December 1995 observations, and is plotted as a function of time. This program had a duration of approximately 1200 minutes. The measurements taken after 1000 minutes show that the intensity of the flare and arc continued to decrease with time after turn-on, converging to nominal values. The camera is demonstrated to be operational and quite stable, within the background limits mentioned.

Due to these positive results, a decision was taken in Cycle 6 to make the F/48 camera available to the users, limited to LONG SLIT SPECTROSCOPY ONLY. This offer is continued in Cycle 7. At the moment of writing, the long slit facility is unique on board the HST, although after the refurbishment mission planned for 1997, STIS will be able to replicate, more efficiently, all the features of the F/48 long slit spectroscopy (see STIS Handbook for additional details).

6.14 OBJECTIVE PRISM SPECTROPHOTOMETRY

Analysis of objective prism images to produce a flux- and wavelength-calibrated spectrum not only requires knowledge of the dispersion curve (given in Table 5), but also proper extraction of the spectrum from the image. The calibrations carried out to determine the dispersion curves given in Table 5 were based on objective prism observations of a emission-line star and a spectrophotometric standard source. Reduction of the spectra relies on preserving the Y-position of features and, for the calibrations, used the two-dimensional spectra software in IRAF to extract 7-pixel wide image sections along the core of the observed spectra.

In order to insure that the extracted spectra can be flux-calibrated, the percent of the total observed flux contained in the extraction must be known. This is equivalent to knowing the encircled energy fraction for photometry of a point-source, only in this case it is an energy fraction of
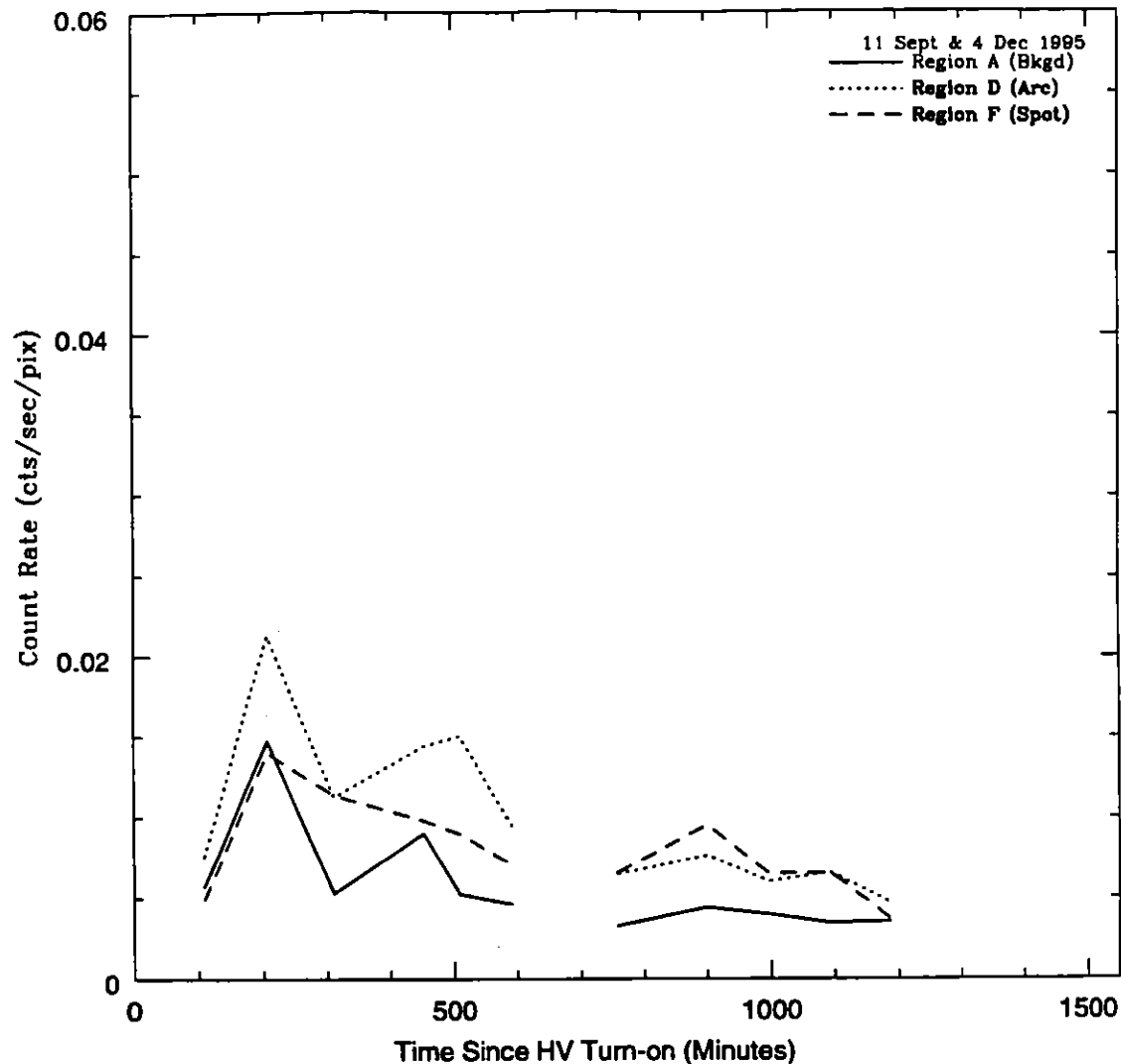
Figure 42. F/48 camera background measured in three areas (A: arc - solid line; B: flare - dotted line; C: background -dashed line) during the latest test, and plotted as a function of time after camera switch-on. The relay showed this same basic behavior during each observation run.

the extraction that is needed. This energy fraction was determined from background subtracted, single source images by dividing spectra of varying extraction widths by the spectra of a 140 pixel wide extraction. This provides some consistency with the DQE determinations for the FOC since the energy fraction of a point source has been defined to be 1.00 for an aperture with a radius of 70 pixels (see FOC-085 for more details). The energy fraction for a spectrum of a given extraction width was determined for each prism, with the results given in Table 13.

Table 13: Energy fractions for spectra as a function of the extraction width.

Extraction Width (pixels)	NUVOP	Error (3σ)	FUVOP	Error (3σ)
5	0.554	0.074	0.480	0.080
7	0.627	0.069	0.557	0.079
9	0.680	0.065	0.616	0.073
11	0.720	0.059	0.660	0.058

The energy fractions given in Table 13 are mean values based on measurements of the Sand-3 and HZ4 calibration observations. The 3σ errors reflect the variations in the energy fraction induced primarily by the effects of breathing and linearity in the spectrum and represent the range of variations that can be expected in well-exposed science observations.

The position of the undispersed target can also have a severe effect on the flux-calibration of the extracted spectrum, an effect that increases toward the longer wavelengths due to the non-linear dispersion of the prisms. The dispersion curves provide the relation between a feature's position in the image to a wavelength, however, the wavelength range covered in a pixel determines how the observed counts are distributed across the wavelength range spanned by each pixel. Both relations, the dispersion curve and the $d\lambda/dx$ relation (wavelength covered by each pixel), are shown in Figure 43. As a result, care must be taken to accurately determine the position of the target in the objective prism image.

Taking both of these effects into account, the calibration of the prisms has been improved considerably over that provided in previous cycles. The final dispersion curves, shown in Table 6, had rms errors in the fit of 0.86 pixels for the FUVOP dispersion curve and 3.43 pixels for the NUVOP dispersion curve. These errors translate to 4Å at 1600Å and 60Å at 3500Å for the NUVOP and 1.3Å at 1150Å and 22Å at 2000Å for the FUVOP. The *synphot* package was also used to calculate the apparent magnitudes for different passbands (including the U and B bands) using both the calibrated spectra and the spectrum from the calibration spectra library. These calculations indicate that the photometry of the NUVOP was within ~0.1 magnitudes from 1600Å - 4000Å and ~0.4 magnitudes from 4000-6000Å, while the FUVOP spectrum was within ~0.1 magnitudes of the catalog spectrum between 1240Å to 3000Å. A comparison of the reduced spectrophotometric standard's spectrum with the catalog spectrum in Figures 2 and 3 shows the close agreement for both the NUVOP and the FUVOP respectively. The disparity in the flux from 1600-1800Å may be due to reduced transmission in the NUV prism relative to the expected throughput. This should be taken into account when performing spectrophotometry in that wavelength range with the NUV prism.

Figure 43. **(a)** Dispersion curve and **(b)** $d\lambda/dx$ relation for the NUV objective prisms, and **(c)** dispersion curve and **(d)** $d\lambda/dx$ relation for FUV objective prisms.
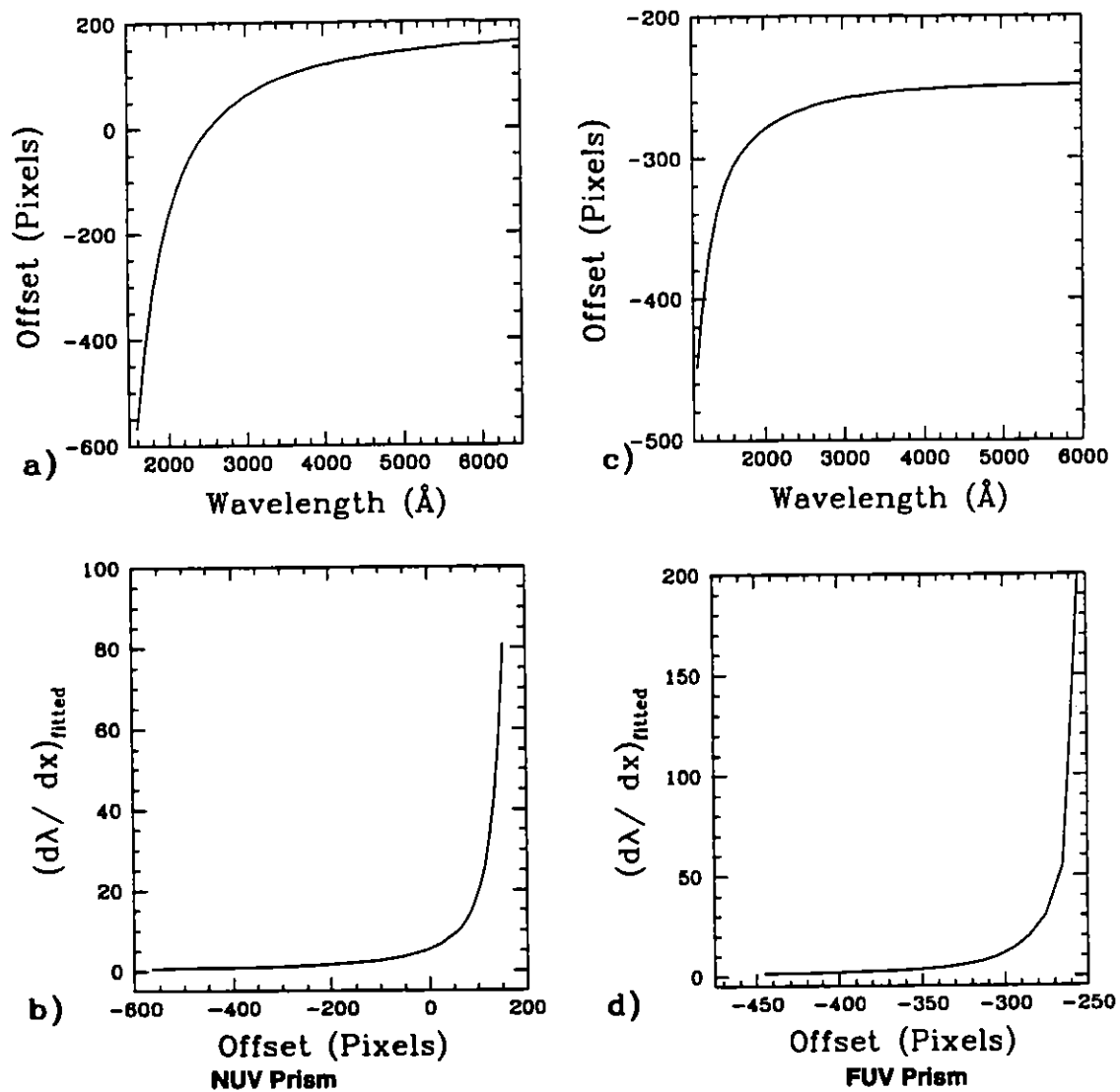
Figure 44. Photometric calibration of the NUVOP. This plot compares the NUVOP spectrum of the spectrophotometric standard HZ4 (**solid**) with the comparison spectrum from the calibration library(**dotted**).
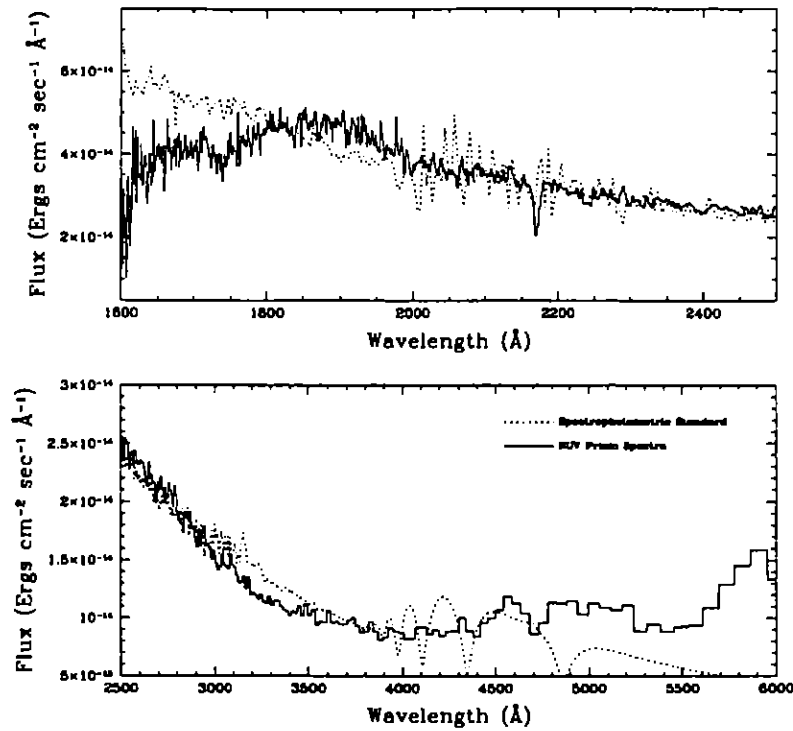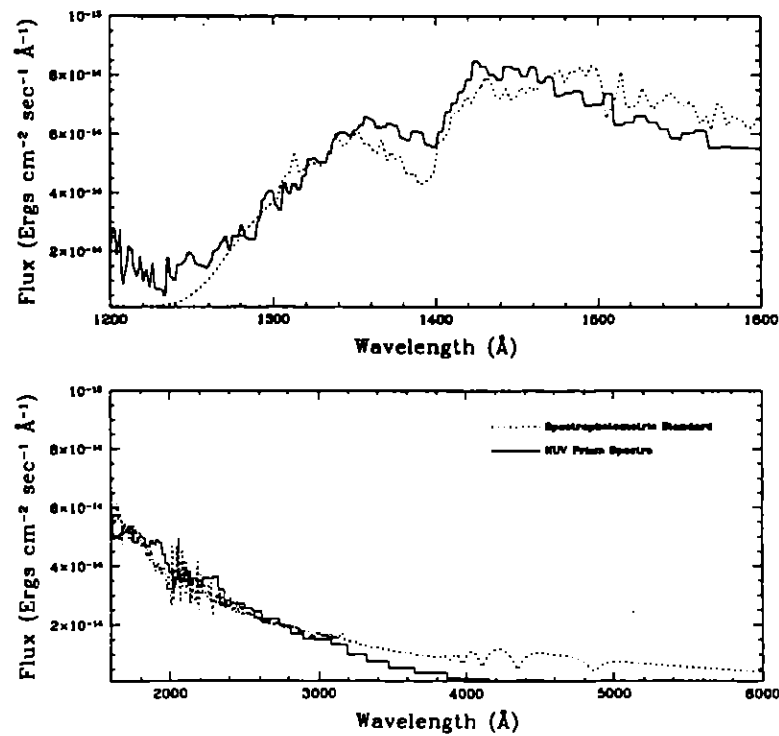

Figure 45. Calibration of Far-UV Objective Prism (FUVOP) spectrum of the spectrophotometric standard HZ4.

7.0 OBSERVER'S GUIDE (PRESCRIPTION FOR ESTIMATING EXPOSURE TIMES)

The first step consists of specifying the required signal to noise ratio *S/N* or the relative accuracy $\delta N/N = (S/N)^{-1}$ of the measurement. Then, the exposure time required to attain that accuracy is given, in general, for Poisson statistics, by:

$$t = (S/N)^2 (R_S + 2R_B) R_S^{-2} \tag{1}$$

where R_S is the source rate and R_B the background rate in an appropriate resolution element in counts sec^{-1}. The problem then simply reduces to properly estimating R_S and R_B.

For a point source in the FOC field of view and for a count rate per pixel much less than N_{MAX} calculated from Table 10, the source rate is given by:

$$R_S = A \int_0^\infty \varepsilon(\lambda) F(\lambda) Q(\lambda) T(\lambda) d\lambda \tag{2}$$

where:
 A = area of the HST primary = 45238.9 cm^2
 $\varepsilon(\lambda)$ = fraction of energy intercepted by the appropriate resolution element
 $F(\lambda)$ = source flux at ST in photons cm^{-2}sec^{-1}Å^{-1}
 $Q(\lambda)$ = FOC+OTA response function for $T(\lambda)$ =1 in counts photon $^{-1}$
 $T(\lambda)$ = transmission of filters or efficiency of dispersing elements

The ratio of obscured area to total area of the primary mirror, equal to 0.138, has been integrated into the values of $Q(\lambda)$ for consistency with SYNPHOT. The terms in eq. (2) can be assumed to be appropriate averages over the pixel to pixel variations in the instrument response function. $Q(\lambda)$ and $T(\lambda)$ are plotted in Figures 30 and 11 through 15.

The background rate, on the other hand, can be expressed, in general, as:

$$R_B = nz \left[B_P + A\Omega^P \int_0^\infty I^B(\lambda) Q(\lambda) T(\lambda) d\lambda \right] \tag{3}$$

where:
 n = number of pixels in appropriate resolution element
 z = 1 for normal pixels, =2 for zoomed pixels
 B_p = inherent detector background count rate per normal pixel (generally 7×10^{-4})
 $I^B(\lambda)$ = specific intensity of diffuse background at ST in photons cm^{-2}sec^{-1}sr^{-1}Å^{-1}
 Ω^P = solid angle subtended by a normal FOC f/48 pixel in steradians = 1.936×10^{-14}

Equations (2) and (3) can be evaluated numerically or by approximating them by assuming that the spectral passband is sufficiently narrow. This permits the following simplifications:

$$R_S \cong 45239 \varepsilon(\lambda_0) F(\lambda_0) Q(\lambda_0) T(\lambda_0) \Delta\lambda \tag{4}$$

$$A\Omega^P = \frac{45238.9(1.936 \times 10^{-14})}{K} = \frac{8.76 \times 10^{-10}}{K}$$

$$R_B \cong nz \left[B_p + \frac{8.76 \times 10^{-10}}{K} I^B(\lambda) Q(\lambda_0) T(\lambda_0) \Delta\lambda \right] \tag{5}$$

where all the relevant functions are evaluated at wavelength λ_0 of peak response and $\Delta\lambda$ is the FWHM bandpass of the instrument in Angstroms. The latter two parameters are listed in Table 3.

K takes on the numerical values 1 and 4 for the F/48 and the F/96 relays, respectively, to account for the different areas the pixels in each relay have on the sky.

For an extended source, the size of the resolution element nz is determined by the user according to his application. For a point source, the encircled energy tabulated in Table 9 should be used to determine $\varepsilon(\lambda)$ and nz for each specific case. The precise area to be used depends in general on the S/N ratio. If it is very high, one can afford to increase the size of the resolution element nz to collect more photons, if it is low, nz should be kept as small as possible. For any particular situation, there is an optimum nz at which the S/N is maximum for a given exposure time t or at which t is minimum for a given S/N ratio. A few quick calculations should be enough to locate this condition once the background has been properly defined as indicated in the next paragraphs.

At least two sources of diffuse background have to be considered in estimating $I^B(\lambda_0)$ in eq. (5). The first is residual airglow above the ST altitude of 500-600 km. For the FOC bandpass of 1200—6000Å only two features need to be considered: the HI, Lyman α line at 1216Å and the OI, 1304Å triplet. The latter feature need only be considered for daytime observations. Their contribution to R_B can be evaluated via the graphs shown in Figure 46. In this graph, the second term in the brackets in eq. (5) is evaluated for the three FOC relays for the condition $T(\lambda_0) = 1$ as a function of spacecraft position in the orbit and for a zenith oriented line of sight. Solar zenith angle 0° corresponds to local noon, 180° local midnight. Lyman α intensities can be expected to increase approximately a factor of 40% if the line of sight drops to the horizon. R_B can be determined by multiplying the data on Figure 46 by the appropriate $T(1216Å)$ or $T(1304Å)$ and nz and adding to B_p.

Table 14: Zodiacal Light Intensities in S10 Units[a]

| $\lambda - \lambda_0^{\beta}$	0°	10°	20°	30°	40°	50°	60°	70°	80°	90°
180	180	152	127	105	89	76	65	59	58	63
170	161	147	123	104	89	76	65	59	58	63
160	147	134	113	98	86	75	64	59	59	63
150	140	129	107	91	80	71	62	58	59	63
140	139	129	105	87	75	67	61	58	60	63
130	141	132	105	86	74	65	60	59	60	63
120	147	138	108	88	75	66	60	59	61	63
110	158	148	113	91	78	68	62	61	62	63
100	175	160	120	96	82	72	64	62	62	63
90	202	176	130	103	87	76	67	64	63	63
80	239	197	144	113	94	82	71	67	64	63
70	296	228	162	124	103	88	76	69	65	63
60	395	275	190	143	116	96	81	72	66	63
50	572	355	238	173	135	108	88	76	67	63
40	SA	545	325	220	160	123	94	80	68	63
30	SA	SA	SA	SA	194	140	102	84	70	63
20	SA	SA	SA	SA	226	157	110	88	73	63
10	SA	SA	SA	SA	SA	167	116	90	74	63
0	SA	SA	SA	SA	SA	170	117	90	74	63
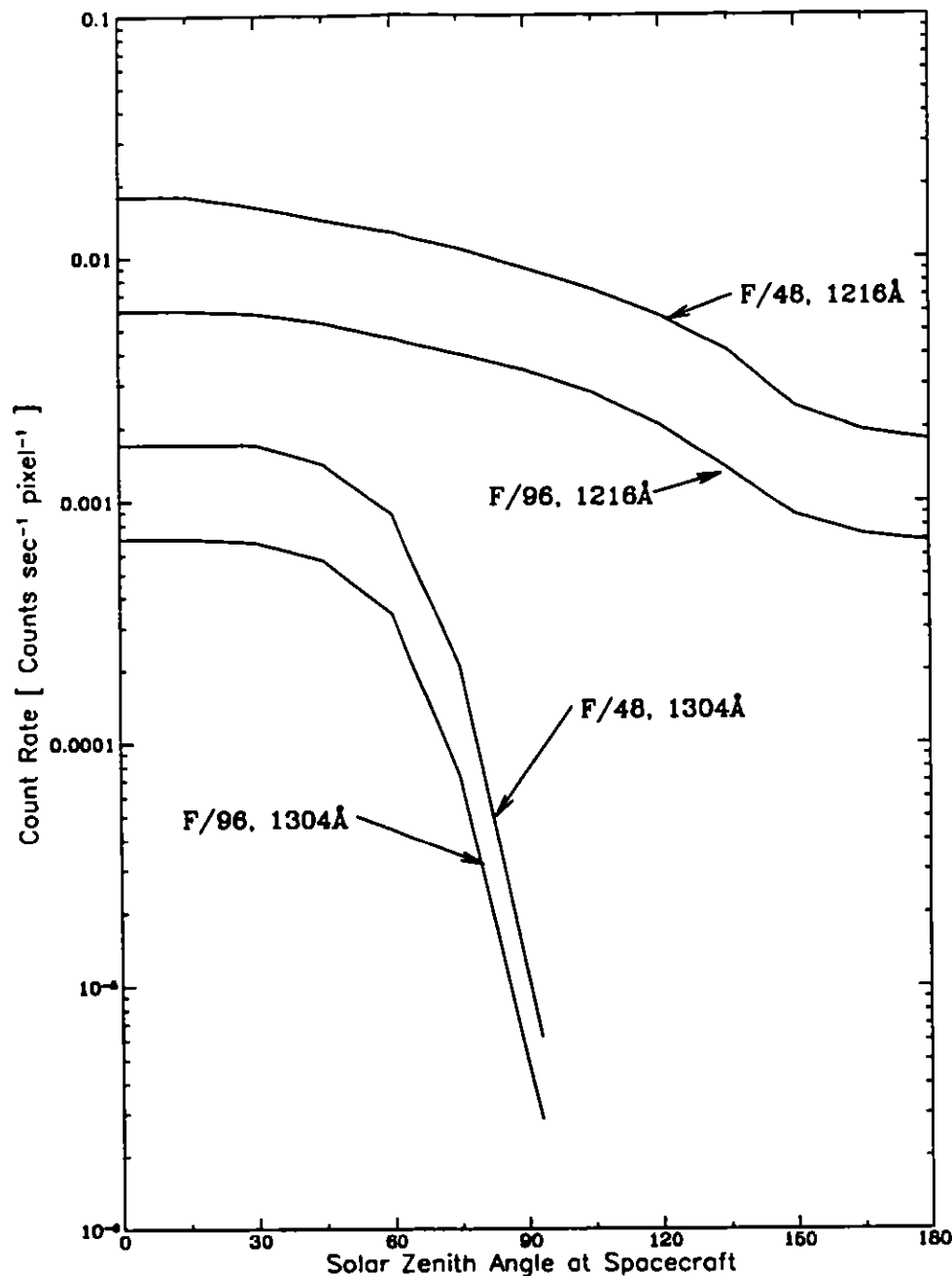
Figure 46. Residual 1216 and 1304Å airglow contribution to the FOC background counting rate with no filters in place in counts sec^{-1} per normal pixel as a function of the solar zenith angle at the spacecraft at 500km altitude. The line of sight is assumed to be oriented towards the zenith.

a. SA- These values are in the region of Sun Avoidance and no observations can be made here.

The second source of background is zodiacal light, which can be an important contributor to R_B in the 3000—6000Å range. This contribution as a function of wavelength is plotted in Figure 47. A standard-solar spectrum was assumed in these calculations. This corresponds to a line of sight direction of ecliptic latitude $\beta=40°$ and helioecliptic longitude $\lambda-\lambda_\Theta=85°$. Thus, R_B for the

zodiacal light can be computed by multiplying the results shown in Figure 47 by the appropriate $nz\ T(\lambda_0)\Delta\lambda$ and by the factor S where S can be computed for any target position by means of the data tabulated by Levasseur-Regourd and Dumont (*Astr. Ap.*, 84, 277, 1980) and reprinted here for convenience as Table 14.
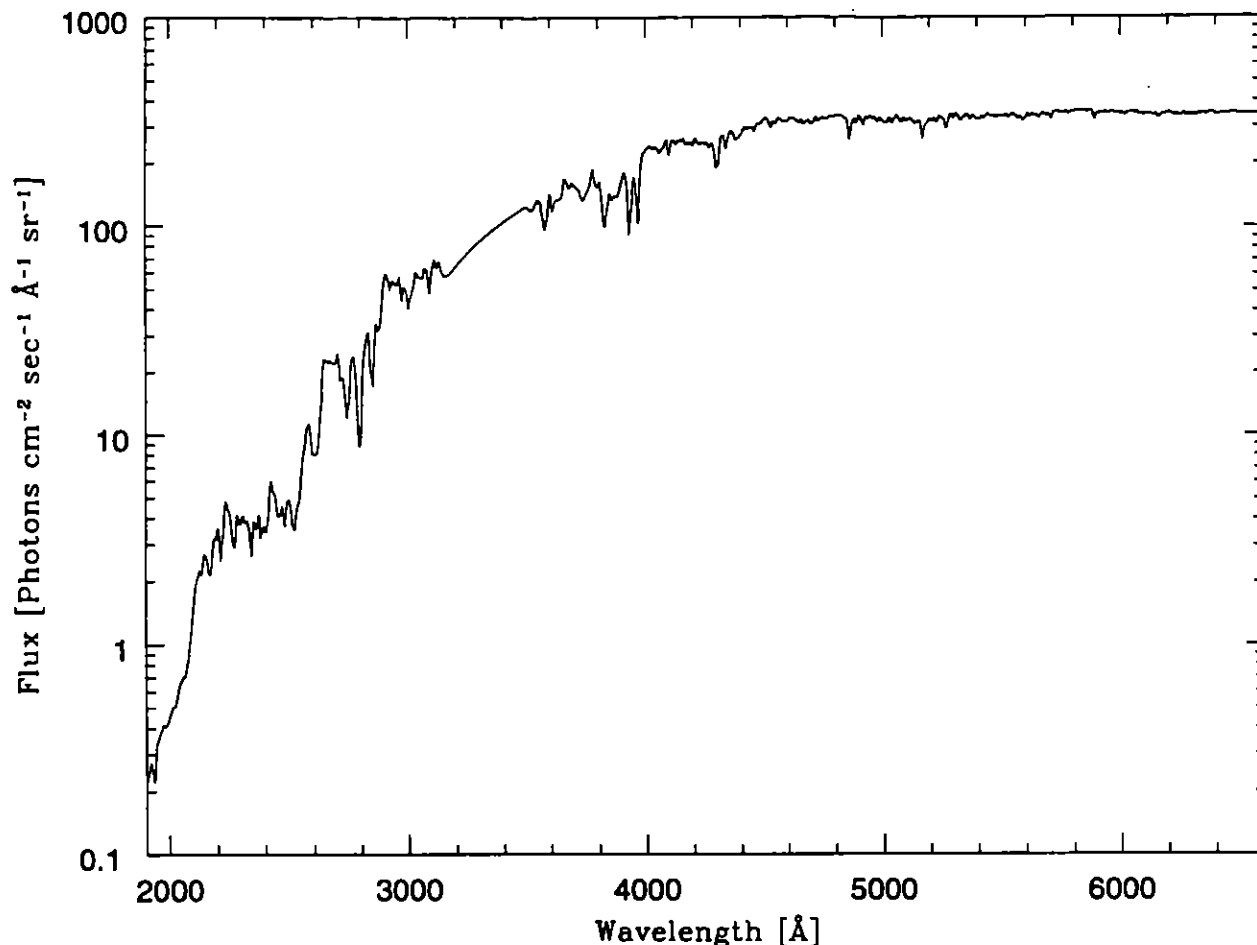
Figure 47. Zodiacal light contribution to the FOC background with no filters in units of photons $sec^{-1}\ \mathring{A}^{-1}\ sr^{-1}$ for use in Eq. 5. The zodiacal light intensity has been normalized to be 1 S10 units at 5300$\mathring{A}$.

7.1 POINT SOURCES

How all this works in practice is best illustrated by some examples.

7.1.1 Imaging

Say that you are interested in observing an unreddened A0V star of $m_\mu=24$ with an accuracy of 10% using the F342W filter, and the F/96 relay with normal sized (unzoomed) pixels for which $z=1$. From Table 3 for the F346M filter, you find that $\lambda_0=3480\mathring{A}$, $\Delta\lambda=434\mathring{A}$, $QT(\lambda_0)=0.039$. The stellar flux $F(\lambda_0) = 8.0 \times 10^2 \times 10^{-0.4 \times 24} = 2.0 \times 10^{-7}$ photons $cm^{-2}sec^{-1}\mathring{A}^{-1}$. Inserting these values into eq. (4), you get $R_S=0.15 \times \varepsilon(\lambda_0)$ counts sec^{-1}. This is the total count rate from that star spread out over a certain number of pixels corresponding to the $\varepsilon(\lambda_0)$ chosen from Table 9. If the

star is reddened by a given total extinction A_V you should use a standard or average reddening curve (see Savage and Mathis, *Ann. Rev. Astr. Ap.*, 17, 73, 1979 for an example) to deduce the appropriate A_λ/V. Then, R_S can be multiplied by $10^{-0.4 A_{\lambda_o}}$ to take this effect into account in the simplest possible way. The possible inaccuracies introduced by this method are probably not worse than the uncertainties on the validity of the reddening curve itself and/or the prediction of the continuous flux to be observed.

Next, calculate R_b from eq. (5) using the data in Figures 46 and 47. Far ultraviolet airglow is not going to be a factor in the B bandpass. The zodiacal light background per pixel can be esti-mated by means of the data graphed in Figure 47 and Table 14. Suppose the star is viewed at $\beta=20°$ and $\lambda-\lambda_\odot = 130°$ for which $S=105$ S10 units, and from Figure 47, we find $I_B(3480Å)$ of ~120 for an intensity of 1 S10. Then, the zodiacal light contribution is

$$(8.76 \times 10^{-10}/4) \times 120 \times 105 \times 0.039 \times 434 = 4.67 \times 10^{-5}\ \text{counts sec}^{-1}\ \text{per normal pixel}$$

so that, assuming $B_p = 7 \times 10^4$ counts sec^{-1} per normal pixel, eq. (5) can be written as:

$$R_B/n \cong 7 \times 10^{-4} + 4.67 \times 10^{-5} = 7.5 \times 10^{-4}\ \text{counts s}^{-1}\ \text{pix}^{-1}$$

Then, the required exposure time can be easily computed from eq. (1) and the data in Table 9 for $\varepsilon(\lambda_o)$. Using the data in the column marked F346M, one obtains:

n	ε(3400Å)	$R_S(cs^{-1})$	$R_B(cs^{-1})$	t(sec)
1	0.087	0.013	0.000075	8584
9	0.409	0.061	0.0068	2005
21	0.528	0.079	0.0158	1772
37	0.601	0.090	0.0279	1800
69	0.722	0.108	0.0520	1817
97	0.773	0.116	0.0731	1948

Thus, integrating under the PSF out to a radius of 0.037 arcseconds at $n = 21$ provides enough flux for the required S/N to be achieved in a minimum exposure time of 1772 seconds. If the back-ground rate for some reason had been 5 times higher, the minimum exposure time would have been 3461 seconds at $n = 9$.

The accuracy of this approximation is, of course, a sensitive function of the shape of the instrument bandpass and is, therefore, expected to be highest for the narrow, well-defined pass-band filters with negligible red and/or blue leaks. It will certainly only give rough order of magni-tude estimates for the wide band pass filters for which a numerical integration of eq. (2) is required for higher confidence predictions. If there are other point sources within a few Airy radii of the primary source, their contribution to the background R_B must be evaluated by means of the appropriate point spread function. It should also be kept in mind that some background sources may vary in intensity during an exposure. This will be the case for the airglow or scattered light emission sources for exposures lasting a good fraction of an ST orbit (see Section 6.5). In this situation, it is advisable to pick the worse case intensity to evaluate the required exposure time.

   — Particular attention has to be paid, in any case, to the expected count rate since it may violate the assumption that $R_S n^{-1} \ll N_{MAX}$ (see Table 10 and Section 6.2.2). If it does for the particular

format chosen as indicated in Table 7, either the format must be changed or a neutral density filter inserted in order to drop the expected rate below the threshold. This, of course, will also result in an increase in the exposure time required to reach the required S/N ratio.

7.1.2 Spectroscopy

Similar computations can be carried out for a point source in the slit of the spectrograph for the F/48 relay except that, of course, the long slit spectrograph efficiencies plotted in Figure 30 have to be used in equations (4) and (5). The bandpass $\Delta\lambda$ is now naturally limited by the projected slit width of 0.06 arcseconds corresponding to 4, 2, 1.3 and 1Å for first, second, third and fourth order, respectively. The transmission of the order sorting filter also has to be taken into account with special attention devoted to possible higher order confusion if the filter has an appreciable near UV and visible leak and the source has appreciable emission in these regions. This confusion can be eliminated completely for point or pseudo point objects with the use of the objective prism FOPCD as the cross disperser. In this case, the transmission and the dispersion of the prism given in Table 6 have to be factored into the calculations.

For the case of the objective prisms, eq. (4) can be rewritten in the form:

$$R_S(\lambda) = 45239\varepsilon(\lambda)F(\lambda)Q(\lambda)T^{op}(\lambda)T(\lambda)\delta\lambda \qquad (6)$$

where T^{op} is the transmission of the prism tabulated in Table 6 and $\delta\lambda$ is the wavelength interval in Å corresponding to the FOC spatial resolution. This interval can be expressed simply as:

$$\delta\lambda = 2r(\lambda)D(\lambda)PS^{-1}$$

where $D(\lambda)$ is the prism dispersion in Å mm^{-1} tabulated in Table 6, $r(\lambda)$ is the radius of the circle enclosing the required energy $\varepsilon(\lambda)$ in arcseconds given in Table 9 and PS is the plate scale of the appropriate relay in arcseconds mm^{-1} given in Chapter 3. Then, the source count rate around λ is:

$$R_S(\lambda) = 9.05\times10^4\varepsilon(\lambda)r(\lambda)D(\lambda)F(\lambda)Q(\lambda)T^{op}(\lambda)T(\lambda)PS^{-1} \qquad (7)$$

Equations (3) and (5) for the noise calculations remain the same except that some simplification can be introduced due to the fact that the overwhelming sources of background in the case $T(\lambda) = 1$ are the system integrated zodiacal light and the geocoronal Lyman α line. Thus, in this case, eq. (5) can be written as:

$$R_B = nz\left[B_p + \frac{2.7\times10^{-5}S}{K} + \frac{c}{b}(7.7\times10^{-4})I^{kR}\right] \qquad (8)$$

where $c=0$ for the NUVOPs and the FUVOP and FOPCD in the F/48 relay, $c=1$ for the FUVOPs on the F/96 relay, $b=1$ for the F/48 relay, and $b=2$ for the F/96 relay. S is the intensity of the zodiacal light in S10 units and I^{kR} is the intensity of the Lyman α airglow in kilorayleighs.

To see how this works, suppose you want to observe a 20th visual magnitude QSO with a V^{-2} spectrum and you want to compute the required exposure time to obtain a S/N=10 at 1700Å with the FUVOP of the F/96 relay. In this case, $F(1700\text{Å})=10^{-5}$ photons cm^{-2}sec^{-1}Å^{-1}. We want to use a 5.5 pixel radius aperture for the photometry of the spectrum at 1700Å, which we find from Table

9 that for $r(1700\text{Å})=0.08$ arcsec we will have an encircled energy of $\varepsilon(1700\text{Å}) = 0.7$. Now, in order to determine how many Angstroms of the spectum will be in the aperture, we find from the data in Table 6 that the dispersion is $D(1700\text{Å})=11.72 / 24 \times 10^{-3} = 488\text{Å mm}^{-1}$. The prism transmission is also given in Table 6 as $T^{op}(1700\text{Å})=0.88$. For the FOC, the detector sensitivity at 1700Å is $Q(1700\text{Å})=0.012$, as found in Table 11. No other filters will be used, so $T(\lambda) = 1$. This means that the source rate from eq. (7) at 1700Å is:

$$R_S = (9 \times 10^4) \times 0.7 \times 0.08 \times 488 \times 10^{-5} \times 0.012 \times 0.88 \times 1 \times (0.526^{-1}) = 0.46 \text{counts sec}^{-1}$$

The count rate is spread over $n=97$ pixels for $z=1$ and $r=0.08$", as given in Table 9. Assuming that $S = 120$ S10 for the zodiacal light, $I^{kR} = 5$ kilorayleighs, $B_p = 7 \times 10^{-4}$ counts sec^{-1} pixel^{-1}, and $K=4$, $c=1$, $b=2$, eq. (8) gives:

$$R_B = 97\left[7\times10^{-4} + \frac{2.7\times10^{-5} \times 120}{4} + \frac{7.7\times10^{-4} \times 5}{2}\right]$$

$$= 97[7\times10^{-4} + 8.1\times10^{-4} + 1.9\times10^{-3}]$$

$$= 0.33 \text{counts sec}^{-1}$$

Finally, the required exposure time is:

$$t = \frac{100(0.46 + 2 \times 0.33)}{0.46^2} = 529 \text{seconds}$$

7.2 EXTENDED SOURCES

The prescription for an extended source deviates only slightly from the formulation discussed so far provided R_S is redefined as:

$$R_S = nzA\Omega^p\int I_S(\lambda)Q(\lambda)T(\lambda)d\lambda$$

$$= nz\frac{8.76\times10^{-10}}{K}\int I_S(\lambda)Q(\lambda)T(\lambda)d\lambda \tag{9}$$

where n is now the chosen number of normal $(z=1)$ or zoomed $(z=2)$ pixels in the required resolution element and $I_S(\lambda)$ is the specific intensity of the extended source in photons cm^{-2}sec^{-1}sr^{-1}Å^{-1}. Equations (3) and (5) for R_B need not be modified. Conversion of other specific intensity units into photons cm^{-2}sec^{-1}sr^{-1} Å^{-1} can be executed via the following relations:

Units	Photons cm^{-2} sec^{-1} sr^{-1} Å^{-1}
U magnitudes per arcseconds squared	$= 3.2 \times 10^{13} \times 10^{-0.4U}$ at 3600Å
B magnitudes per arcseconds squared	$= 6.4 \times 10^{13} \times 10^{-0.4B}$ at 4470Å
V magnitudes per arcseconds squared	$= 4.3 \times 10^{13} \times 10^{-0.4V}$ at 5560Å
1 Rayleigh Å^{-1}	$= 8.1 \times 10^4$
1 erg cm^{-2}sec^{-1}sr^{-1}Å^{-1}	$= 5 \times 10^7 \lambda(\text{Å})$

Units	Photons cm^{-2} sec^{-1} sr^{-1} Å^{-1}
1 Wm^{-2}Hz^{-1}sr^{-1}	$= 1.5 \times 10^{29}[\lambda(\text{Å})]^{-1}$
1 S10	$= 333$

Suppose, for example, you want to observe a Lyman α aurora above the limb of Jupiter of intensity 20 kiloRayleighs with a spatial resolution of 0.28 arcseconds with a $S/N = 10$ with the F/96 relay. You will be using 400 F/96 pixels for this purpose. You should use the F120M filter because it has the highest transmission at Lyman α and the lowest transmission at the longer wavelengths where the disk Rayleigh scattering spectrum may overwhelm any far UV auroral features.

From Figure 13, you find that at λ=1216Å, the F120M filter has T=0.1 and from Table 11 you deduce that Q(1216Å)=0.006. Then, since in this case the Jovian emission line of width $\leq$1Å is much narrower than the instrumental bandpass of 86Å, eq. (9) can be written simply as:

$$R_S \cong \frac{400 \times 8.76 \times 10^{-10}}{4} \times 2 \times 10^4 \times 8.1 \times 10^4 \times 0.006 \times 0.1$$

$$= 0.09 \text{counts sec}^{-1} \text{per resolution element}$$

The background rate R_B will be dominated by the detector background and the geocoronal Lyman α airglow if the observation is carried out at night. From the curve marked the F/96, 1216Å in Figure 46 for a typical observing configuration of 150° local solar zenith angle, you obtain 2.2×10^{-3} counts sec^{-1} pixel^{-1} looking towards the zenith. This implies that, for $B_p = 7 \times 10^{-4}$ counts sec^{-1} pixel^{-1}, you have:

$$R_B = 400[7 \times 10^{-4} + 2.2 \times 10^{-3} \times 0.1]$$

$$= 0.37 \text{counts sec}^{-1} \text{per resolution element}$$

This means that S/N=10 for this Jovian aurora and resolution can be reached in:

$$t = \frac{75(0.09 + 2 \times 0.37)}{0.092^2} = 2562 \text{seconds}$$

Observations at higher spatial resolution would require correspondingly longer exposure times.

If this same aurora is to be observed against a planetary disk background of Lyman α emission of 15 kilorayleighs with the same accuracy, the relevant background rate becomes:

$$R_B = 400\left[7 \times 10^{-4} + 2.2 \times 10^{-4} + \frac{8.76 \times 10^{-10}}{4} 1.5 \times 10^4 \times 8.1 \times 10^4 \times 0.006 \times 0.1\right]$$

$$= 400[7 \times 10^{-4} + 2.2 \times 10^{-4} + 1.7 \times 10^{-4}]$$

$$= 0.44 \text{counts sec}^{-1} \text{per resolution element}$$

so that:

$$t = \frac{25(0.09 + 2 \times 0.44)}{0.092^2} = 2994 \text{seconds}$$

In this case, however, you might be looking onto the visible disk of the planet and the visible leak will dominate the count rate. To estimate the visible leak contribution notice that at $\cong 5000\text{Å}$, the F120M filter has a residual transmission of 10^{-4} and assume the Jovian spectrum to be solar with an intensity of $\cong 2 \times 10^6$ Rayleighs Å^{-1} at 5000Å. Thus, you can approximate the effect by spreading this intensity over $\cong 1500\text{Å}$ where $Q(\lambda) \cong 0.03$. Then, with these assumptions:

$$R_B \cong 0.44 + 400\left[\frac{8.76 \times 10^{-10}}{4} 2 \times 10^6 \times 8.1 \times 10^4 \times 0.026 \times 10^{-4} \times 1500\right]$$

$$= 0.44 + 50 \text{counts sec}^{-1} \text{per resolution element}$$

A solution to this problem would be to insert another filter into the beam to suppress the visible contamination. A good choice would be F140W for which $T(1216\text{Å}) = 0.05$ and $T(5000\text{Å}) = 3 \times 10^{-4}$ and:

$$R_S = 0.09 \times 0.05 = 4.5 \times 10^{-3} \text{counts sec}^{-1} \text{per resolution element}$$

$$R_B = 0.44 \times 0.05 + 400\left[\frac{8.76 \times 10^{-10}}{4} 2 \times 10^6 \times 8.1 \times 10^4 \times 0.026 \times 10^{-4} \times 3 \times 10^{-4} \times 1500\right]$$

$$= 0.02 + 0.015 = 0.035 \text{counts sec}^{-1} \text{per resolution element}$$

$$t = \frac{235(4.5 \times 10^{-3} + 2 \times 0.035)}{(4.5 \times 10^{-3})^2} = 9.2 \times 10^4 \text{seconds} = 26 \text{hours}$$

Obviously, this hypothetical program cannot be accomplished with the FOC. To reduce the exposure time to physically realistic levels one needs to, say, reduce the required accuracy and/or spatial resolution. For example, halving both the accuracy and the resolution yields a more acceptable exposure time of 1.6 hours.

Finally, suppose you wish to image an extended object (a planetary nebula, for example) with the F/96 relay at the highest possible resolution in the zoomed configuration for the biggest possible field of view. Suppose the object exhibits a line spectrum with a surface brightness at H_β of 5 $\times 10^{-13}$ ergs $\text{cm}^{-2}\text{sec}^{-1}$ arcsec^{-2} and you wish to use the F486N interference filter to isolate the line to an accuracy of 10%. From the data shown in Figures 12 and 30 you find that at 4861Å, $T = 0.6$, and $Q = 0.026$. From the conversion relations, you note that $I_s(4861) = 5 \times 10^{-13} \times 4.25 \times 10^{10} \times 5 \times 10^7 \times 4861 = 5.16 \times 10^9$ photons cm^{-2} sec^{-1} sr^{-1}. Thus, eq. (9) becomes for $n=1$, $z=2$:

$$R_S = \frac{2 \times 8.76 \times 10^{-10}}{4} \times 5.16 \times 10^9 \times 0.6 \times 0.026 = 0.03 \text{counts sec}^{-1} \text{per zoomed pixel}$$

From the data shown in Figure 47 and a zodiacal light brightness of 90 S10 and $B_p = 7 \times 10^{-4}$ counts s^{-1} per normal pixel, eq. (5) becomes:

$$R_B = 2[7 \times 10^{-4} + 3 \times 10^{-7} \times 0.63 \times 34] = 1.4 \times 10^{-3} \text{counts sec}^{-1} \text{per zoomed pixel}$$

because $T(\lambda_o) = 0.63$ and $\Delta\lambda = 34\text{Å}$ for the F486N filter from the data in Table 3. In conse-

quence, finally:

$$t = \frac{100(0.03 + 2 \times 1.4 \times 10^{-3})}{0.03^2} = 3644 \text{ seconds}$$

8.0 FOC EXPOSURE TIME SIMULATORS

The general procedures to compute the required exposure times for any FOC observing configuration and possible emission source outlined in the preceding section are perfectly adequate for most purposes including proposal preparation and feasibility verification. There are cases, however, where it is useful to have the means to evaluate more precisely the integrals in eqs. (2), (3) and (9). This capability is especially important when the emission source spectrum is not well behaved outside the wavelength range of interest (see, for example, the situations described in Sections 6.10 and 7 concerning visible leaks), when the precise spatial distribution of counts in the image is important as in crowded fields and for more precise planning envisaged in Phase II of proposal preparation. At present there are three ways to simulate FOC exposures:FOCSIM, SYN-PHOT in the STSDAS package, and SIMPRISM in the FOCPRISM package.

8.1 FOCSIM

To fully simulate both simple and complex situations, an exposure time simulator for the FOC has been developed by F. Paresce, Y. Frankel and W. Hack of STScI. This program, called FOC-SIM, presently evaluates the exposure times and S/N ratio for all imaging exposures. FOCSIM computes the expected spatial patterns of the FOC images using PSFs and, therefore, evaluates the correct S/N for wide bandpasses and/or closely-spaced pairs of stars to simulate crowded field conditions. Since FOCSIM only works with point sources or sources extended over the field of view, it can not simulate the dispersed image created by the objective prisms. Instead, the task SIMPRISM can be used to simulate these dispersed images (see Section 8.5).

FOCSIM is a menu driven interactive FORTRAN program which runs under IRAF. It accepts user input describing the FOC observing configuration and the physical characteristics of an astronomical source to be observed. The user may select from a number of model spectra, have FOCSIM create its own synthetic spectrum (black-body, power law or flat), or use his own file of wavelengths and fluxes in appropriate units. The sources resident in the program include 77 simulated stellar spectra covering a wide range of MK classes generated by the Kurucz (1979) stellar atmosphere models and a number of UV standard stellar spectra from IUE (*Ap. J. Suppl.*, 40, 1, 1979). In addition, FOCSIM can create its own flat continuum between two wavelengths, line spectrum with up to three emission lines, blackbody source of arbitrary temperature or power law spectrum of arbitrary index. The normalization factors of flux and wavelength can all be specified arbitrarily by the user. Furthermore, the diffuse background can also be calculated precisely by FOCSIM using zodiacal light spectrum for UV air glow and the inherent detector background can be accommodated with user supplied intensities. Unfortunately, FOCSIM currently only simulates the normal 512X512 imaging format. When using different formats, the user must account for format sensitivity increasing the expected count rate according to the values given in Table 11 (see Section 6.3.1).

In support of COSTAR, FOCSIM has been upgraded to allow for automatic selection of the COSTAR imaging modes. The latest DQE tables are available for use with FOCSIM for both of the relays. These can be selected in the FOCSIM setup and can be found in the FOCSIM auxiliary directory. In addition to the new DQE tables, theoretical PSFs have been produced to simulate COSTAR corrected FOC PSFs and observed PSFs taken with the COSTAR-corrected FOC have been added to the FOCSIM libraries. Using the updated DQE tables and PSFs allow FOCSIM to simulate COSTAR corrected observations with accuracies dominated by the errors inherent in the

PSFs, primarily from small changes in focus or position in the COSTAR-corrected field of view. Initial experience in Cycle 4 has indicated that errors of about 10% in the simulated count rates for the 512X512 format should be expected.

The output of FOCSIM includes all relevant information on the input parameters selected, the appropriate instrumental parameters and subsidiary data such as the individual components of background, the monochromatic count rate shown in Figure 36, restrictions such as NMAX, data on the magnitude of the red and blue leaks, and, of course, the resultant exposure times. The user can also request that FOCSIM output the transmission curves for the filters and the source spectra as IRAF SDAS tables, which can subsequently be plotted using IRAF procedures.

FOCSIM will be made available at the STScI to interested users of the FOC who have local accounts. Unfortunately, FOCSIM is not available for general distribution along with STSDAS for a couple of reasons: first, it uses additional libraries which are prohibitively large, and secondly, it does not conform to IRAF's standards for software programming. A beginner's manual is available upon request from STScI, either as a POSTSCRIPT file or a printed version. It describes the basic steps necessary for running FOCSIM by walking through a sample session. The manual also provides a list of the catalogs of spectra that are available for use with FOCSIM and samples of the output which FOCSIM produces. Additional on-line help has recently been added which can be accessed through the standard IRAF help facilities.

8.2 WWW Form for FOCSIM

An interface to FOCSIM has been developed for WWW as part of the FOC team's Instrument Pages (see Chapter 9). This form allows the user to simulate a single point-source in the standard 512X512 FOC F/96 (pre- and post-COSTAR) imaging format with average values for the background sources. The user can choose to calculate an exposure time needed to reach a desired S/N or to calculate the S/N for a given exposure time using either observed or theoretical PSFs. Finally, library spectra or synthetic spectra can be normalized to user specified values, although user supplied spectra can not be used with this form.

The short, easy to use graphical interface afforded by the WWW browsers makes this simulation quick to use with results being returned to the user in a very short time. The full ASCII output of FOCSIM gives all the calculated count rates for the source and background and can be saved by Mosaic to the users local disk for later reference.

Along with the fill-out form for running FOCSIM, the FOCSIM Beginners Manual is also available on WWW. Both the Beginners Manual and the FOCSIM form can be found at URL

```
http://www.stsci.edu/ftp/instrument_news/FOC/Foc_tools/focsim/focsim.html
```

8.3 SYNPHOT

The STSDAS package of routines provided by STScI includes the SYNPHOT simulation package. SYNPHOT uses a standard set of DQE and filter transmission tables ensuring that it utilizes the most up-to-date throughput information in calculating count rates. In addition to the latest throughput tables, SYNPHOT also takes into consideration the different sensitivities of each format (described in Section 6.3.1).

SYNPHOT does not, however, have the capability of providing any spatial information for any source as it does not work with either the PSFs or encircled energy tables. SYNPHOT outputs the total count rate expected from any given source spectrum, then the results from Table 8 can be

used to calculate the peak count rate for a point source. This value should follow the limitations discussed in Section 6.2 to maintain photometric accuracy.

Background sources, such as zodiacal light, are not incorporated in the current version of SYNPHOT. The calculation of the background and subsequent S/N for the image must then be calculated by hand using the methods in Section 7.

8.4 Image Orientation Calculation

The geometry of an object, the use of the f/48 long-slit facility, or the f/96 objective prisms may require that the FOC be oriented a particular way in order to get the desired science. The Proposal Instructions illustrate how to calculate the ORIENT angle requested in a Phase II proposal for use with RPS2, but it involves a number of different angles adding (or subtracting) from each other. A WWW form has been created to simplify this calculation for FOC exposures and to plot out the results for the user. The form can be found at the URL:

http://www.stsci.edu/ftp/instrument_news/FOC/Foc_tools/wwwnorth/wwwnorth.html

Once the format that will be used is selected, the user supplies the angle from North to the format's Y axis and the form calculates the proper ORIENT angle. A postscript plot is also produced showing the format size, and the position angle of north in the image for verification of the desired orientation. If a POS TARG is required, the final target position will also be calculated and plotted relative to the reference position for the format. This tool should make it easier for an observer to determine the desired orientation or to verify an orientation that was used for an observation.

8.5 Objective Prism Image Simulation

FOCSIM handles point sources and normal extended sources well, unfortunately the capability for simulating the dispersed point sources from an objective prism image was not included. Instead, the related IRAF package FOCPRISM was created to simulate and analyze objective prism images based on calibrated dispersion curves for each objective prism. This package uses the same filter transmission curves and DQE curves as STSDAS and FOCSIM, insuring reliable count rate calculations. Since it uses routines related to SYNPHOT, it can also take into account the different formats for the FOC. However, unlike FOCSIM, it does not output count rate calculations or include background sources. Instead, it creates a simulated image for the given exposure time and source spectra.

This simulated image does not suffer from non-linearity effects like the FOC, thus the user should use this to make sure the desired image does not exhibit count rates greater than 1 count/ sec/pixel for an emission line of interest or about 0.5 counts/sec/pixel for continuum regions of interest. These count rates serve as guidelines for maintaining photometric accuracy in the final objective prism image. On-line help is available to answer questions about running the simulator. The associated routine, OBJPRISM, takes an objective prism image, extracts and calibrates the spectra given the exposure time and undispersed position of the star. An observer can not only simulate an objective prism image now but also analyze the image after it has been taken using the same software that was used to calibrate the prisms.

8.6 Limiting Magnitudes

FOCSIM can be used to predict the limiting magnitude of any observing configuration. An

example of this type of calculation is shown in Figures 48 and 49 for scenarios matching the observed average in-flight conditions. Studies of calibration images have been used to determine an average zodiacal light intensity of S10 = 120 units and a detector background for the F/96 relay of $B_p = 7 \times 10^{-4}$. These are the same values that are used when the FOCSIM WWW form is used. Figure 48 shows the predicted exposure time in seconds needed to reach a S/N = 10 for a specified visual magnitude of a B5V star through the F342W (U) filter with the F/96 camera. With average in-flight conditions, we should expect to detect a B5V star of V=28.75 with the U filter at a S/N of 5 in about 10 hours of exposure time with the F/96 relay. The limiting magnitude is V=28.25 if a S/N=5 in a 5 hour exposure is deemed sufficient.

Figure 49 illustrates the results of calculations using extended sources. For this case, the specific intensity of the source is expressed in terms of visual magnitudes per arcseconds squared and the spectrum is assumed to have the shape of a B5V star. The spatial resolution in this case is chosen to be 0.112 arcseconds, which corresponds to binned regions of 8 pixels on a side for the F/96 relay. One should be able to detect a source with an intensity of 23.5 V magnitudes per arcseconds squared at S/N = 10 and 0.112 arcsecond resolution in 10 hours of exposure with the U filter under the average in-flight conditions described earlier.
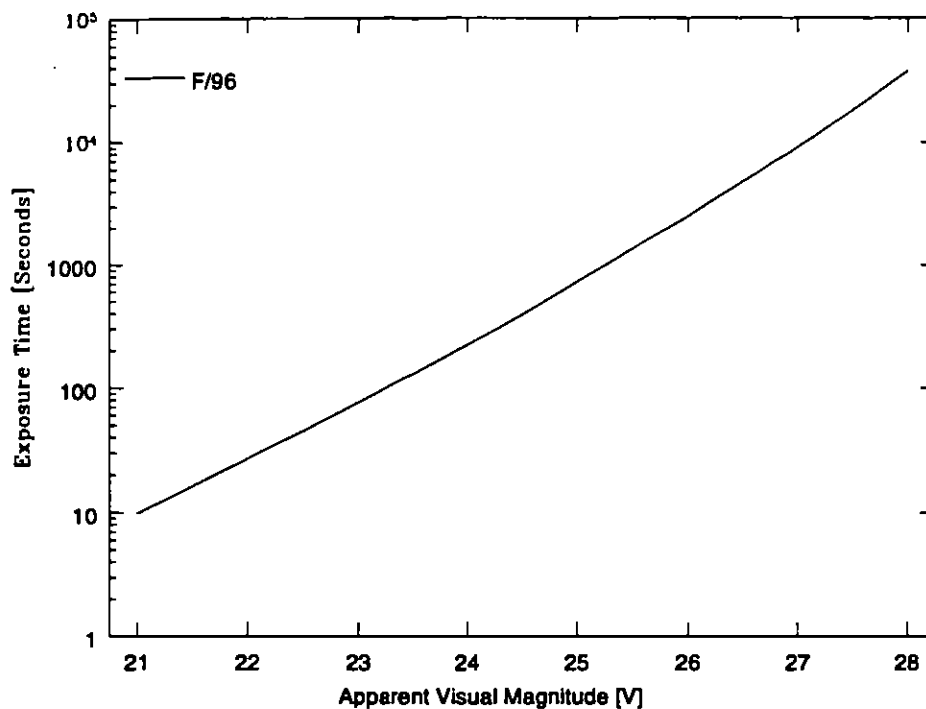
Figure 48. Exposure time required to reach a S/N = 10 on a B5V star with the U filter in an average observing condition with $B_p = 7 \times 10^{-4}$ counts sec^{-1} pixel^{-1} and a zodiacal light intensity of 120 S10.
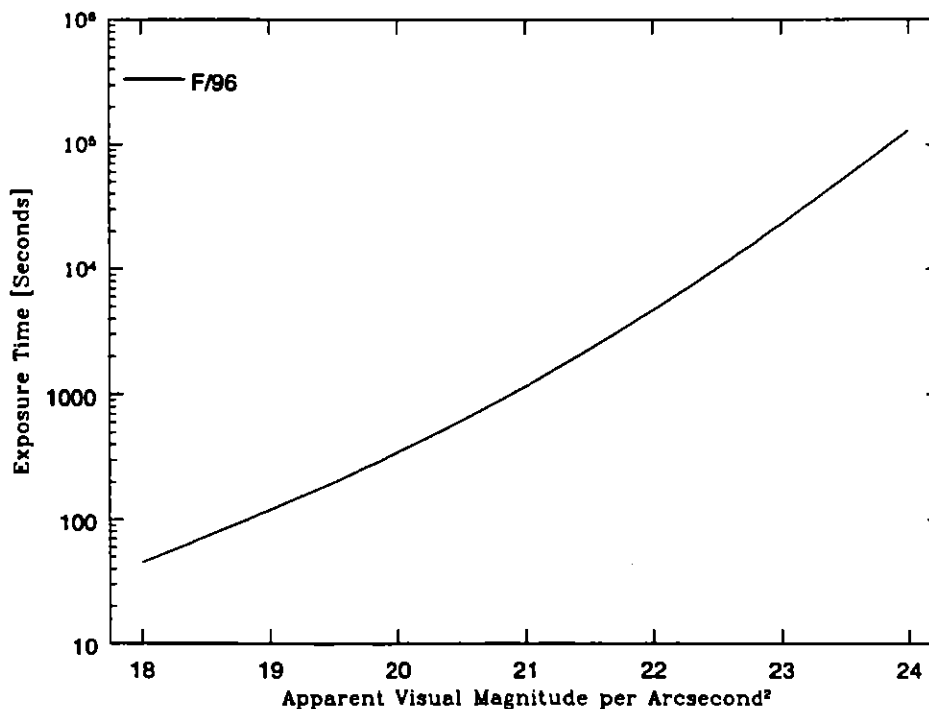
Figure 49. Exposure time required to reach a S/N = 10 on a B5V spectrum extended source with 0.1 arcsecond resolution with the U filter in the observing condition listed in Figure 48.

9.0 FOC WWW PAGES

The FOC team has developed a set of WWW pages to allow greater access to a variety of information regarding the operations, calibrations, and documentation of the FOC. The page can either be accessed from the STScI home page under the Instruments link, or directly using the URL:

http://www.stsci.edu/ftp/instrument_news/FOC/topfoc.html

The introductory page contains links to Advisories, Calibration Products and Tools, Frequently Asked Questions, Manuals and Reports, User Support, the main STScI page, and a directory of the instrument team members.

The Advisories section contains the latest news on the status of the FOC, including changes in calibration information or perhaps even in the operation of the instrument. This should be the first stop for any observer with FOC data in order to see how the data they have, or plan to acquire, might be affected. The date this section was last updated will also be provided.

The Calibration Products and Tools section stands as one of the main repositories of information regarding the calibration and status of the instrument. Descriptions of calibration files and tables used during the standard 'pipeline' calibration of all HST data can be found here. These descriptions provide a history of the calibration files for each instrument and indicate which reference files are most suitable for any given HST data. In addition, calibration information useful for post-'pipeline' reduction of HST data is also listed here. The un-smoothed flat fields for the FOC are examples of the types of additional calibration data that is available.

Many analysis, calibration, and proposal preparation questions are addressed by topic under the Frequently Asked Questions link. A list of subjects can be searched on topics ranging from proposal preparation to data analysis. These lists will be updated throughout the Cycle to quickly address some of the most commonly asked questions about the FOC.

Manuals and reports produced by the FOC team were usually only available as paper copies. Now, though, the FOC Instrument Handbook, a set of Instrument Science Reports (ISR) and other reports are available in PostScript form under the Documentation link. The ISRs document various calibration efforts by the FOC team and can be searched either through a complete list of ISR titles or by topic keyword. At present, only the most recent reports are available in PostScript form, but a convenient e-mail facility is provided to request paper copies from the Institute. In addition to the Handbooks and ISRs, many other reports produced by the FOC team can be found in this section, resulting in an on-line documented history.

We highly recommend that all HST Observers, especially first-time General Observers (GOs), visit the Institute if possible in order to take full advantage of the advice and expertise offered by STScI. Such a visit provides the GO with the latest information concerning HST data reduction and analysis. The User Support section provides details on what can be done at STScI and how to arrange a trip.

In addition to the online documentation available through the pages, questions can be directed to the Institute using the online form accessible from the bottom of nearly every FOC WWW page. This form provides the capability to request paper copies of most FOC documentation (including ISRs and the FOC Handbook), and to direct questions to the STScI Help desk regarding any aspect of FOC operation, from proposal preparation to data analysis. The STScI Help desk can be contacted through email at :

help@stsci.edu

These pages undergo revisions with the inclusion of more information as it becomes available. This knowledge, although quite technical at times, can now be accessed easily in order to help observers get the best possible science out of their HST data. For users who are unable to take advantage of the WWW browsers, this information can also be accessed via ftp or gopher. The ftp directory structure mimcs the structure of the WWW pages and is located at:

ftp.stsci.edu/instrument_news/FOC

Users will see a large number of '.html' files in the directories. These are the documents used by the WWW browsers to direct users to the information stored in the underlying directories. The files referenced by each WWW page has been organized into directories as follows:

- Foc_faq: Contains files with frequently asked questions and their answers

- Foc_handbook: Contains text and PostScript versions of the FOC Instrument Handbook

- Foc_isr: Contains available PostScript versions of FOC ISRs, with an index

- Foc_notices: Contains old advisories issued by the FOC team

- Foc_tips: Contains PostScript copies of FOC TIPS presentations

- Foc_tools: Contains calibration files, with README files as indexes. Also has directories for FOCSIM, PSFS, and flat field images.

10.0 FOC DATA ANALYSIS AND PRODUCTS

10.1 PIPELINE PROCESSING

All data taken by the FOC are automatically processed and calibrated by the Routine Science Data Processing (RSDP), also called the "pipeline". It is possible to repeat, off line, the calibration part of the pipeline processing by using an IRAF/STSDAS task called CALFOC (CALibration of FOC data), used automatically by the pipeline. For every observation, the user will receive two sets of data coming out of the pipeline: the input and output files to CALFOC. The input files to CALFOC are:

1. the raw image,

2. a mask image characterizing the location of known bad pixels, reseaux, and likely data errors determined by on-line processing of transmitted data called the Data Quality File (currently unused),

3. a file containing astronomical information related to the observation called the Standard Header Packet, and

4. a file containing engineering data related to the observation called the Unique Data Log.

The output files from CALFOC are:

1. the geometrically corrected image,

2. the geometrically and photometrically corrected image, and

3. a trailer file (*.trl) containing a log of the pipeline processing.

The data processing flow chart for normal imaging and spectrographic images is shown in Figure 43. CALFOC assumes that the processing parameters are in the image header, either directly from RSDP preprocessing, or inserted by task "cloadrsdpx" or "loadrsdpx". The processing parameters govern which correction steps are to be performed, and which calibration files are to be used. For normal imaging observations, the following steps are performed in order:

* dark count subtraction (not done at this time)
* format dependent photometric correction (using ITF reference file) (not done at this time)
* unzoom the zoomed image
* absolute calibration affecting header parameters only
* geometric distortion correction involving data interpolation and requiring a new mask image
* relative calibration or flat field correction (removing instrumental sensitivity variations) using UNI reference file, which is a reciprocal of a flat field.

For spectrographic (long-slit) observations, the final step is different i.e.:

* spectrographic relative and absolute calibrations with flux and wavelength calibrations affecting both data and headers (currently not performed, awaiting calibration).

In the spectrographic mode, several orders may overlap. The pipeline does not deliver separately calibrated data sets for each order, leaving line identification and order deconvolution to the user. The pipeline delivers the raw image and data sets corresponding to the results of the tasks as indicated in Figure 43. Detailed information on FOC calibration procedures and algorithms can be found in the HST Data Handbook, available from STScI. Some more general information is contained in the Calibration HST Data Set manual. See also the STSDAS Calibration Guide.
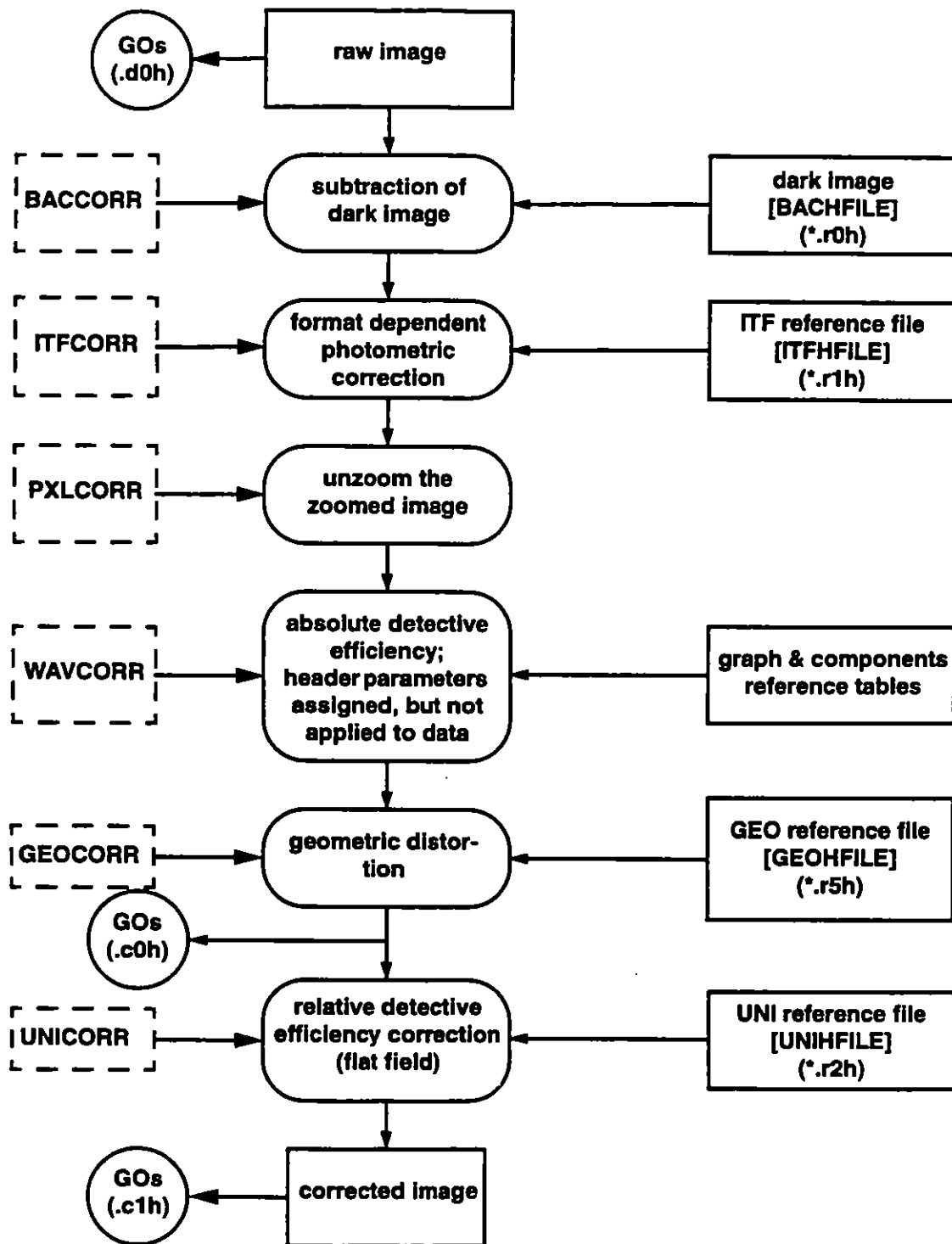
Figure 50. Flow diagram of FOC imaging data through the Routine Science Data Processing System.

10.2 GENERAL PROCEDURES

All delivered images are REAL*4 datatype, to avoid integer rounding. The actual counts in each pixel are preserved as accurately as possible to permit immediate visualization of counting statistics and noise.

10.2.1 Dark-Count Subtraction

The dark-count reference file multiplied by the exposure time is subtracted from the input science file. The dark-count file is a full-frame image (512 X 1024), so if the science file is smaller than full frame then only the appropriate section of the dark-count file is used. Use "imarith" or "darkx" IRAF tasks. Standard processing does not apply the dark-count subtraction to images at this time.

10.2.2 Format-Dependent Photometric Correction (ITF)

These reference files are called ITF (Intensity Transfer Function) files for historical reasons. There is one such file for each format. The format-dependent correction is applied by multiplying the image from the previous step (i.e. the dark-count subtracted image) by the appropriate ITF file. Use "imarith" IRAF task. Standard processing does not apply the photometric correction to images at this time.

10.2.3 Correct For Zoom Mode

If the image was taken in zoom mode, the next step is to split the data values along the first image axis (the sample direction). This means that each rectangular pixel is split into two square pixels. Therefore,the length of the first axis (NAXIS1) is doubled, and the length of the second axis (NAXIS2) is not changed. The overall flux is conserved. Use "dezoomx" IRAF task.

10.2.4 Compute Absolute Sensitivity

This does not affect the data values. The inverse sensitivity, pivot wavelength and RMS bandwidth of the optical mode selected are computed and stored in the header of the output image. The zero-point magnitude and the observation mode are also saved in the output header. Multiplying the data numbers in the image by the value of the header parameter PHOTFLAM and dividing by the exposure time converts the image counts to flux density F in units of ergs per square centimeter per second per angstrom. Use "evalband" IRAF task.

10.2.5 Geometric Correction

A raw FOC image is distorted by a few percent for two reasons, the optics and the detector. Both distortions are comparable in magnitude. The optical distortion was computed by ray tracing, and the detector distortion is measured by taking flat-field images and observing the positions stars in a crowded field relative to the uniformly spaced reseau marks that are etched on the photocathode. A geometric correction reference file includes both optical and detector distortion. It gives the location in the input (distorted) image of each corner of every pixel of the output (cor-

rected) image. The geometric correction is performed for each output pixel by adding up the counts in the corresponding region in the input image. This procedure rigorously preserves flux. Use "newgeom" IRAF task.

10.2.6 Relative Calibration or Flat Field Correction (images only)

This correction is called the uniform detective efficiency (UNI) correction, and removes the nonuniform detective efficiency of the detector. It is applied by multiplying the image by the UNI reference file (format independent), which is the reciprocal of a flat field. The UNI files are full-frame in size, which is 1024 × 1024 because the image is dezoomed. As with the dark-count correction, if the science image is smaller than full-frame then only a subset of the UNI file is used. Since the sensitivity of the detector depends on wavelength, six different UNI files are provided for different wavelengths. For the F/48 configuration, lambda = 3345 and 4800 Angstroms are provided; for the F/96 configuration, lambda = 1360, 4800, 5600, and 6600 Angstroms are provided. The file to select is determined by comparing wavelengths of the UNI files with the pivot wavelength of the optical mode. Use "imarith" IRAF task.

10.2.7 Spectrographic Detective Efficiency Correction (f/48 spectra only)

The SDE correction is only applied to spectrographic images. It includes both the flat-field correction and a conversion from counts to flux density. It is applied after geometric correction because the absolute sensitivity depends on wavelength, and a major function of the geometric correction for spectrographic images is to align the spectrum with the axes and set the dispersion. The correction is applied by multiplying by a spectrographic detective efficiency reference file. The use of an order-selecting filter can change the location of a given wavelength on the photocathode, so there are several reference files; the appropriate one is selected based on the filters used. These files are full-frame (1024 × 1024), so only a subset will be used if the science image is smaller than this. Use "imarith" IRAF task. Standard processing does not apply the SDE correction to images at this time.

11.0 FOC CALIBRATION: STATUS AND ACCURACIES

11.1 CURRENT CALIBRATION STATUS

The performance of the FOC+COSTAR system has been characterized in detail using a combination of ground-based and in-flight tests. After COSTAR deployment, an extensive calibration program was carried out (SMOV) to describe the performance of what could be considered, to all intents and purposes, a new instrument. At that point, the scientific program was enabled.The Cycle 4 calibration program then completed this initial effort and fully characterized the FOC+COSTAR performance. In Cycle 6, we are in a routine situation, and our calibration program is divided into two parts:

1.a set of monitoring tests, whose aim is to maintain the calibration level previously achieved (e.g. pointing accuracy, geometric distortion, flat fields), or to discover possible variations in performance

2.a number of dedicated tests designed to maximize the scientific output of the instrument.

These tests were designed after having carefully reviewed the observing proposals to be executed during the current cycle, and would, for example, provide accurate PSFs and check the detector response at certain wavelengths, or characterize special capabilities not previously calibrated.

In Table 15 we provide a list of the calibration tests which will be performed in Cycle 6, with their objective outlined. The Cycle 5 and Cycle 6 calibration programs both relied on the science goals of the GO programs to determine what needed special calibration effort. For example, a significant number of FOC users in Cycles 5 and 6 are using the polarizers, and therefore an extensive calibration program has been designed, after checking all the individual requirements, to ensure that the best science is achieved with the FOC polarizers. Anyone interested in the details of these calibration programs, or any Phase II program, can view the proposals using WWW at:

http://www.stsci.edu/public/propinfo.html

Table 15: Summary of Cycle 6 Calibration Plan

ID	Proposal Title	Accuracy	Objective
Routine Monitoring Programs			
6893	UV Throughput Monitoring	3%	monitor UV throughput
6894	Aperture Location Monitoring	0.2"	monitor pointing stability
6895	PSF Monitoring	2μ	monitor image quality
	Geometric Distortion Monitoring		monitor stability of geometric distortion
Special Calibration Programs			
6929	Absolute Sensitivity	5%	characterize FOC photometric response
6930	Neutral Density Filter Checks	5%	determine throughputs of ND filters
6931	Exploratory Focus Monitoring Test	1μ	investigate new means to monitor focus
6932	UV Flatfields	5%	improve UV flat-field accuracy
6933	Prism Wrapup	1 pixel	calibrate prism dispersion from 4000-6500Å

11.1.1 The Routine Calibration Programs

The routine calibration programs are designed to monitor those aspects of FOC performance that are believed to be subject to time variation. Typically, observations are made at 3 month intervals to verify that the performance has not changed significantly and to warn users if a significant difference is found.

11.1.2 The Special Calibration Programs

The special calibration programs are designed to offer a more detailed calibration of modes or observation types and represent a class of calibration observations that may be executed once with the results expected to be valid over a long time base. Previous special calibrations, as well as monitoring programs, have resulted in calibration accuracies as discussed in the next section. Should your program require calibration accuracies that are not obviously satisfied by the values listed below, then you should contact an FOC Instrument Scientist for guidance. Individual GO programs requiring special calibrations must directly request these observations as part of their Phase I proposal.

11.2 CALIBRATION ACCURACIES

The accuracies specified in Table 15 are requirements, in that we expect that a single observation, provided that sufficient photons are detected that Poisson noise can be neglected, will be good to the accuracy stated at the 1σ level. In practice, it may be possible to use more careful analysis to determine quantities of interest to higher accuracy.

11.2.1 Absolute Sensitivity

The F/96 Absolute Sensitivity is calibrated between 1200Å and 5500Å to an accuracy of 10% (1σ). This is achieved by taking high S/N images of UV spectrophotometric standards through a number of filters, and by comparing the observations with the simulations. Observers can expect to achieve similar accuracy in the absolute flux measurement of a point source as long as the aperture used for photometry is large enough so that the PSF structure is not affected significantly by orbital variations (typically radius > 0.2 arcsec). Several causes contribute to this uncertainty: some can be removed, others cannot:

- *Errors in the spectrophotometric standards:* the published error estimates for the UV spectrophotometric standards range from 3% at longer wavelengths to 5% at shorter wavelengths.
- *Errors in the assumed filter transmission curves:* The filter transmission curves were carefully measured on the ground, but some subsequent degradation or change in performance might have occurred since launch.
- *Format dependence:* A variation of sensitivity with video format has been noted. In particular, differences have been found in the relative response of the more common F/96 formats with respect to the 512×512 imaging format, see Section 6.3.1. We believe that the correction factors are accurate within 5%.
- *Variability of F/96 DQE:* The UV throughput of the FOC has been regularly monitored as part of an observatory program. There appears to be a 5% degradation in sensitivity since launch, with no evidence for any wavelength dependence.

- **Source spectrum:**. The value of PHOTFLAM provides an exact average $F\lambda$ across the bandpass, irrespective of the source spectrum's shape. Large errors can arise in situations where redleak results in a significant fraction of the light observed, especially if the source has most of its emission outside the desired bandpass. If there is any doubt as to whether there are significant color effects, the observer is advised to use SYNPHOT or FOCSIM to check their absolute fluxes.

- **Pattern Noise:** The small-scale sensitivity variation described in Section 6.9 modulates the measured flux from a star. The effect on the measured flux depends on the aperture size used; for apertures larger than 3 pixels radius the effect is believed to be less than 2% rms.

- **Other flatfield effects:** Large scale and pixel-to-pixel flatfielding errors can occur to affect the accuracy of PSF photometry. Taking multiple dithered observations can reduce the effect of the small-scale contribution.

11.2.2 Geometric Distortion

The plate scale has been determined for the F/96 camera to an accuracy of ~0.3%. The following formats (all centered) are geometrically calibrated and maintained: 512x1024 zoomed, 512x512zoomed, 512x1024, 512x512, 256x256, 128x128. Since March 19, 1995, these formats are calibrated using the new model (described in Section 6.11). The new geometric calibration has an accuracy of better than 0.5 pixel rms. The F/48 plate scale has never been measured after COSTAR deployment. Therefore, the estimated value must be used (see Section 6.12).

- **Long Term Stability: F/96.** The F/96 relay has shown a reasonable level of stability over the period since launch. This relay has experienced a very slow, steady change over this time however this appeared primarily as a simple shift (~3 pixels) and rotation (~0.2 degrees), neither of which significantly affect astrometric measurements.

- **Short Term Stability: F/96.** As fully described in Sections 6.11 and 6.12, most of the variations in distortion in the F/96 camera occur during the warm-up time. However, residual variations (~0.25%) are noticed over the next few hours. We encourage users who require the best possible astrometric conditions for their observations to write a comment in the proposal requiring the observations not to start immediately after HV switch-on. They may also want to talk to their Contact Scientist.

- **Stability: F/48.** In January 1992, the geometric distortion behavior of the F/48 relay, (which had never been quite as stable as the F/96), began suddenly to show large, erratic variations in its distortion characteristics. Due to the long inactivity period, it is not clear whether this effect persists. The data taken in early 1995 seem to indicate overall stability.

Overall this means that, for an average observation, the separation of two stars can be measured to an accuracy of 0.5 pixels(~7 mas) or 0.3%, whichever is larger.

11.2.3 Flat Fields

Smoothed full flat fields have been determined at 1300, 4800, 5600, and 6600Å to an accuracy of ~3%. Pixel-to-pixel errors may be much larger due to blemishes and detector defects, as it can be seen from Figures A1 and A2. Unsmoothed flat fields are available on-line through the FOC Web pages, but we also list here all the major features, so the reader can learn to recognize them in the FOC images:

- **Border Effects:** can be external (F/96 occulting fingers, upper and lower left corners of the F/

96 image, lower right corner for the F/48 image) or internal (bad rows at the top and bottom of the raw images, leftmost columns of the raw images, and a number of columns at the beginning of the scan line). These effects are not correctable.

- **Video and Digitizing Defects:**
  1.fly back of the read beam of the television camera, especially noticeable in small formats.
  2.noise glitches on the scan coil driver caused by changes in the most significant bits of the line counter, show up as horizontal features at lines 256, 512 and 768. This is much more noticeable in the F/48 relay.
  3.Both relays show the center 512 × 512 outlined by a sharp change in sensitivity. The effect is due to burn-in of the heavily used standard camera format.
  These effects are not correctable, with the possible exception of the F/96 fly-back.
- **Reseau Marks, Scratches and Blemishes:** as the pipeline flat field correction is heavily smoothed, none of these effects will be flat fielded out.
- **Large Scale Variations:** it is estimated that the F/96 large scale response is accurate to better than 3% over most the photocathode, at the wavelength it was obtained, excluding edges and corners.
- **Time Variability:** a minor amount of time variability has been observed in the flat field response. It is largest just after HV turn-on, where changes of 1-2% are seen when compared to the response seen after an hour observation. The changes for the F/48 are twice as large.
- **Pattern Noise:** The response of individual pixels varies with a sinusoidal pattern by up to 5% or so due to pattern noise; this is described in more detail in Section 6.9.

These factors limit the achievable accuracy for photometry of both point and extended sources.

11.2.4 Pointing Accuracy

- **F/96.** The center of the F/96 aperture has been determined to within 0.2", and is maintained at this accuracy level through routine monitoring during each Cycle. All the centered formats have the same accuracy.
- **F/48.** The center of the F/48 acquisition format has not been calibrated after COSTAR deployment. The acquisition of an external non-astrometric target has shown that the center appears to be offset of approximately 2" from its real position.
- **F/48 Slit.** The position of the spectrographic slit relative to the image center will be determined. Present calibration plans expect to determine this offset to within 0.1".

The astrometric accuracy for an isolated star in the FOC field is determined by the Guide Star coordinate accuracies, which have an rms uncertainty of approximately 0.5 arcsec.

11.2.5 Objective Prisms

A new set of F/96 near-UV (NUVOP) and far-UV (FUVOP) dispersion curves have been derived based on Cycle 4 calibration observations of an emission line source and a spectrophotometric standard. These dispersion curves provide photometry with errors of approximately 0.1 magnitudes from 1600-4000Å for the NUVOP and 1200-3000Å for the FUVOP. Larger errors of up to 0.2 magnitudes can be expected outside these wavelengths, especially in the red end of the spectrum. Furthermore, the dispersion curves have rms errors in the fit of 3.4 pixels for the NUVOP and 0.87 pixels for the FUVOP. These errors in the fit correspond to errors in the wave-

length determination of 1.8Å at 1600Å and 17Å at 2500Å with the NUVOP and 1.3Å at 1200Å and 16Å at 1800Å with the FUVOP.

11.2.6 Polarization

Accuracies of polarization measurements for point sources are governed by those achievable for relative photometry. Typical 1σ uncertainties are 4-5% in the degree of polarization for point sources. Better precision is achievable for extended sources, where the differences between the PSFs of the polarizers and small-scale flatfield structure are less important; typically ±2% (1σ) or so may be achieved. The angles made by the polarizers to the V2V3 coordinates are believed to be correct to approximately 3°; analysis of the Cycle 4 polarization calibration data by Robinson & Thomson (see the proceedings of the Workshop "Calibrating Hubble Space Telescope: Post Servicing Mission", eds. Koratkar & Leitherer) indicate an offset of −1.4 ± 0.3°. Calibration of the instrumental polarization involves measurements of the flux of unpolarized targets through each of the polarizers; this effect is very difficult to separate from differences in the throughputs of the polarizers. The properties of the reflecting surfaces in the optical train and the angles of incidence of the beams predict an instrumental polarization of less than 1%.

Users should also be aware that some care is needed in analyzing polarization data since the PSF is noticeably different through each of the three polarizers. This makes estimating the relative throughputs difficult for small apertures, and analysis of complex fields at resolutions of <0.1" will require some care in matching the PSF profiles in the observations through the three polarizers. Current calibration plans for Cycle 5 call for the acquisition of PSFs through each of the polarizer filters in combination with the F342W filter. This should aid users in understanding the smaller features provided high enough S/N PSFs can actually be obtained.

11.2.7 F/48 Long-slit Calibrations

The F/48 camera is being used for science in Cycle 5 and Cycle 6. Almost no calibration has been performed with the F/48 relay since the First Servicing Mission. In order to support usage of the F/48 long-slit facility in Cycle 6, we have designed a calibration plan which will devote approximately 10 orbits to the calibration of the F/48 long slit, summarized in Table 16. This program will satisfy the basic requirements of acquiring a target onto the slit, performing the wavelength calibration, correcting for S-distortion and calibrating the absolute flux scale.

- *Target Acquisition:* unless the target is very large (>10"), the default mode of target acquisition is to take an INT ACQ image using the 512x1024 (Z) format, and then use the position of the object of interest in the image to calculate the small angle maneuver that will place the object on the slit. Based on calibration observations of NGC4151 and science observations of M31, we believe we can perform this maneuver with a typical 1σ error of 0.1 arcsec. This means that our 95% confidence error box for the slit location is ± 0.2 arcsec across.

Typically, when acquiring to the slit, the initial acquisition image may place the target of interest anywhere between 0 and 4 arcseconds from the fiducial position. The accuracy of a slew of this distance, especially when calculated from a geometrically distorted raw image, limits the accuracy of the initial acquisition. An absolute calibration of the astrometric position of the

imaging aperture would ensure that the initial pointing error is kept to 2 arcseconds or less, improving the accuracy of the slew to put the target on the fiducial point.

The goal accuracy is therefore that the initial pointing error be no more than 2 arcseconds, and that the offset between the slit and the acquisition fiducial point is known to 0.1" (1σ).

- *Wavelength Calibration*: since the FOC has no internal line spectrum source, it is necessary to rely on external targets for wavelength calibration. The most convenient are planetary nebulae, which display an emission-line spectrum extended over areas larger than the FOC slit. NGC 6543 was used to determine the wavelength calibration during Cycles 0 and 1; it is a high sur- face brightness planetary nebula with bright lines. It makes an ideal target for Cycle 5 obser- vations.

Each format that is used for science needs its own wavelength calibration; the reseau marks do not provide enough resolution to map the distortion with enough detail. We will calibrate the 512x1024(Z) and 512x1024 formats. *The accuracy goal is 0.3 pixel rms, which corresponds to 44 km/sec, everywhere along the slit and for the wavelength range 3750-5010Å.*

- *Absolute Sensitivity & S-distortion:* this is measured by placing a spectrophotometric stan- dard star down the slit. The narrowness of the slit (0.062") makes it necessary to position the star very accurately, otherwise a small centering error will be confused with a sensitivity defi- cit. To ensure that the star is placed centrally in the slit to an accuracy of 1/4 of the slit width, it is necessary to scan the star across the slit in steps of 2/3 of the slit width, or 0.04 arcsec- onds. Since the position of the slit relative to the imaging fiducial is uncertain by ± 0.2" (2σ), it is necessary to use 11 scan positions. Accurate placement of the star will give us the relative position of the slit and acquisition fiducial to 0.05" or so. *The spectrophotometry goal is an accuracy of 20% binned over 20 pixels in first order, $\pm 50\%$ binned over 20 pixels in 2nd and 3rd orders.* This accuracy goal will be valid only where it is measured.
A further goal of the spectrophotometry program is to measure the S-distortion for a star at 2 positions along the slit, separated by 3 arcsec. *The accuracy goal of this is 0.3 pixels.* Also, by peaking up the star's flux at 2 different positions on the slit, it is possible to measure the angle the slit makes with the V2V3 axes. *The goal of this measurement is 0.4 degrees.*

Table 16: Summary of Cycle 5/6 F/48 Calibration Programs

ID	Proposal Title	Accuracy	Objective
6198	FOC F/48 Absolute Spectrophotometry, S-distortion, and Fine Slit Location	0.015" slit location S-distortion to 0.3 pix $\pm$ 20% 1st order sens.	Determine location of the slit to 0.1", measure the S-distortion and absolute sensitivity.
6199	FOC F/48 Longslit Spectrograph Wavelength Calibration	λ to 0.3 pixel rms	Determine wavelength calibration.
6200	FOC F/48 Geometric Correction and Plate Scale	distortion: 0.5% plate scale: 0.5%	characterize F/48 geometric distortion and plate scale
6890	FOC F/48 Aperture Location	0.2"	Determine the aperture location
	FOC F/48 Longslit Radial Velocity Template	~40 km/sec rms	Create a 2-d spectrum as a stellar template for radial velocity determinations

12.0 ACKNOWLEDGMENTS

Figure A1. Extended format (512z × 1024) de-zoomed image taken with the pre-COSTAR F/48 relay under uniform external illumination. This image does not show the effects of vignetting that will be present after the installation of COSTAR. The slit finger is just visible at the right center edge inside the default 512 × 512 imaging format which is outlined with the solid line.
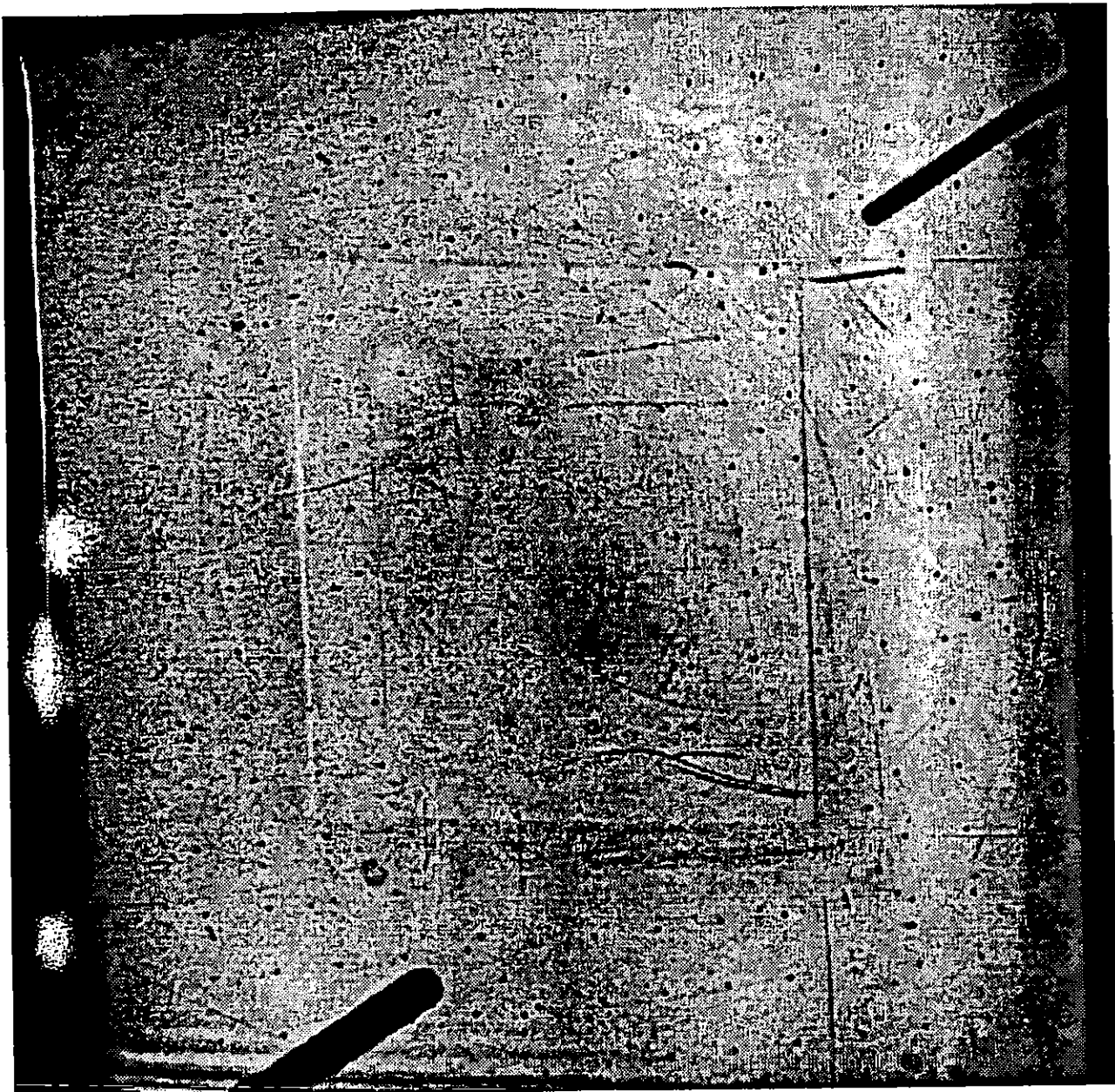
Figure A2. Extended format (512z × 1024) de-zoomed image taken with the pre-COSTAR F/96 relay under uniform external illumination. The occulting fingers and clipping of the frame due to the baffle are clearly visible.
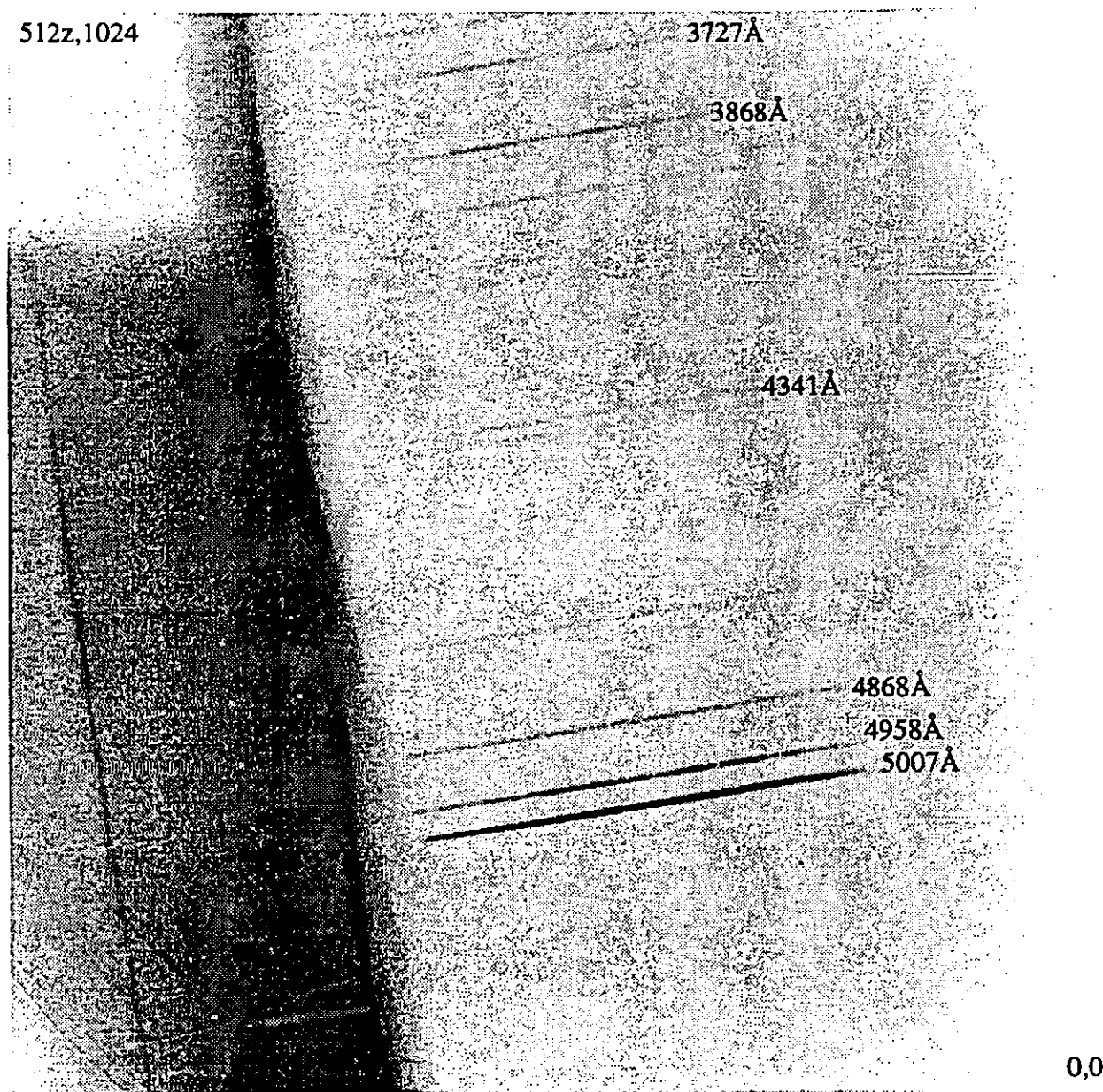
Figure A3. Extended format (512z × 1024) de-zoomed negative image taken with the pre-COS-TAR F/48 relay in spectrograph mode of an extended external object. The area in the upper left corner suffers serious vignetting, limiting the wavelength coverage for slit-less spectroscopy.
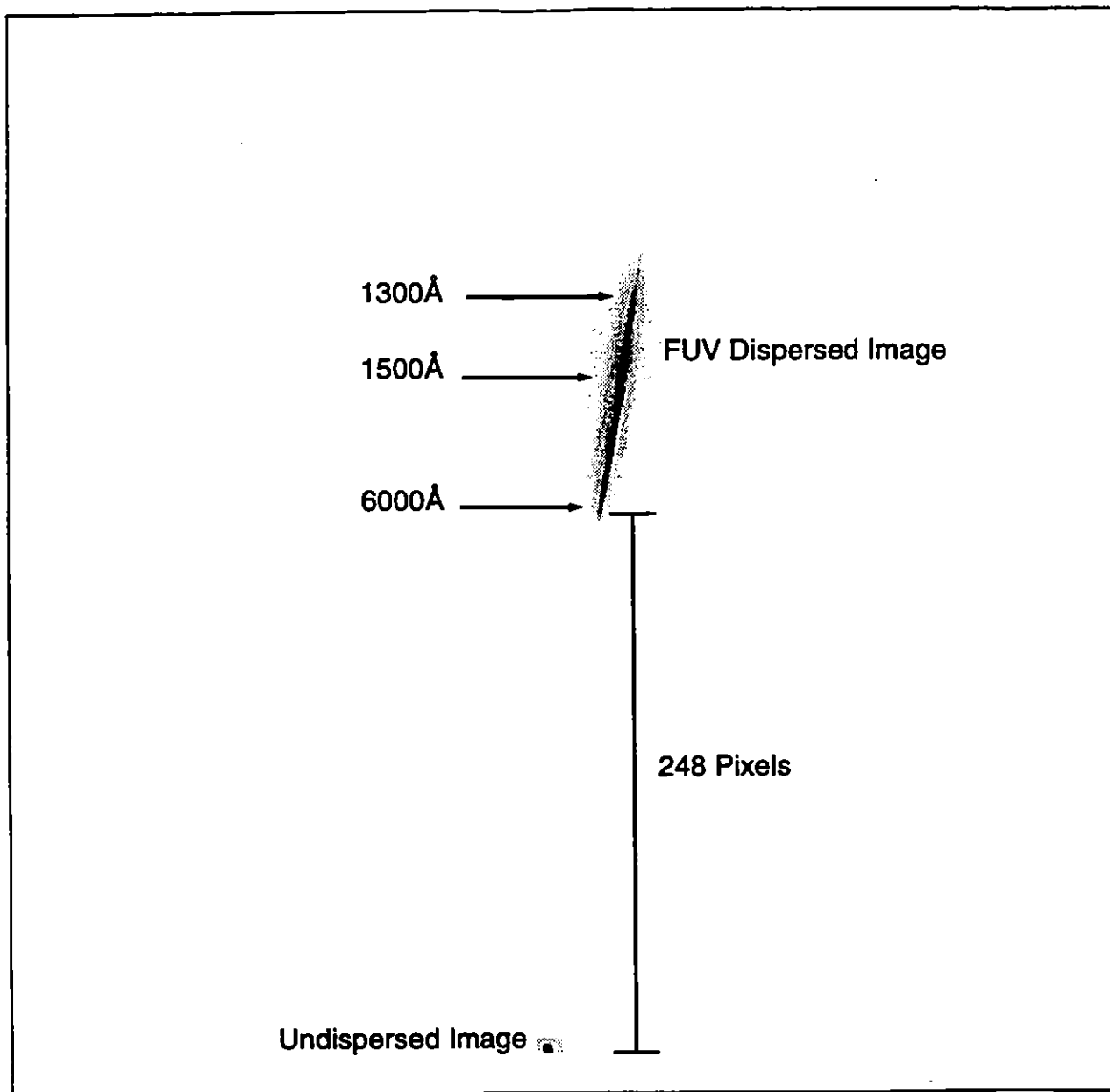
Figure A4. Central 256 × 512 pixels of the full 256 × 1024 pixel negative image taken with the COSTAR-corrected F/96 relay showing a star at the undispersed position overlayed with the image showing its Far-UV prism spectrum.

INDEX

V
Video Processing Unit(see "FOC, Video Processing Unit")
vignetting 9, 22–23

W
WFPC2 1–3, 8
    comparison with FOC 52
WWW 93

Z
zodiacal(see "background, zodiacal light")